Borehole to Surface Electrical Monitoring of a Salt Water Injection Experiment

By

Dimitri Bevc

B.A. (University of California) 1984

THESIS

Submitted in partial satisfaction of the requirements for the degree of

MASTER OF SCIENCE

in

ENGINEERING
MATERIALS SCIENCE AND MINERAL ENGINEERING

in the

GRADUATE DIVISION

of the

UNIVERSITY OF CALIFORNIA at BERKELEY

Approved: D.F. Morrison Sept 12, 1989
Chair Date
Alex Becker Sept 12, 1989
Paul A. Witherspoon Sept. 5, 1989

****

BOREHOLE TO SURFACE ELECTRICAL MONITORING OF A SALT WATER INJECTION EXPERIMENT

Dimitri Bevc

BOREHOLE TO SURFACE ELECTRICAL MONITORING OF A SALT WATER INJECTION EXPERIMENT

by

Dimitri Bevc

ABSTRACT

This thesis describes a field experiment which demonstrates the sensitivity of borehole to surface resistivity measurements in ground water investigations. A quantity of saline water was injected into a fresh water aquifer while the resistivity was monitored using a multi-channel borehole to surface system. Two experiments were conducted using different receiver electrode arrays and salt water slugs of different salinity. The data was interpreted using a three-dimensional resistivity modeling program, and compared to hydrological measurements taken during the injection. In addition to demonstrating the sensitivity of subsurface arrays, the measurement of bulk resistivity identified a ground water flow pattern not detected by hydrological measurements.

Since rock resistivity is a function of pore water resistivity it is not surprising that electrical measurements are sensitive to conductive contaminants. However, as shown here, the measurement array configuration and how the data is presented are essential components in determining how well the data can be interpreted. The observed data was superposed to simulate many array configurations and apparent resistivities were calculated. The best results were obtained by superposing the data to form subsurface dipole electrode sources. Interpretation is further facilitated by examining the result in terms of normalized voltage, rather than apparent resistivity.

ACKNOWLEDGEMENTS

I would like to thank my thesis advisor, Professor H. Frank Morrison, for his support and guidance. I would also like to thank Professor Alex Becker for his assistance in determining the system characteristics and for his advice and suggestions. Thanks also go to Professor Paul A. Witherspoon for reading the thesis. Ted Asch, Seunghee Lee and Mike Wilt did much of the preliminary work in designing and setting up the field experiment. Their work, encouragement, and suggestions were invaluable. Many Engineering Geoscience students and Lawrence Berkeley Laboratory employees donated their time and resources, for which I am grateful.

Special thanks to Mary DeNobriga and my parents Nada and Vladislav Bevc for their moral support and encouragement.

Table of Contents

List of Illustrations

Introduction

Today's fast paced, consumption oriented and energy hungry society is placing a tremendous burden on our planet. Environmental concerns, often overlooked in the past, are becoming increasingly urgent issues. At the forefront is the issue of ground water management and contamination. This has led to a flourish of activity in hydrology, and the assessment of geophysical methods for mapping contaminant plumes and monitoring ground water migration.

Of all the geophysical techniques, the electrical methods have had the most widespread use in ground water investigations because many contaminants decrease the pore water resistivity which in turn reduces the bulk earth resistivity (Saunders and Stanford, 1984; Rodriguez, 1984). Surface resistivity surveys have been used successfully to delineate aquifers, locate fresh, brackish, and saline water-bearing zones (Van Overmeeren, 1989) and to determine the bulk ground water velocity and hydraulic conductivity (White, 1988). Unfortunately surface methods do not work well for low resistivity contaminants and areas of conductive overburden if the zone of interest is too deep. Furthermore, the sensitivity of surface surveys is strongly influenced by the inhomogeneous near surface layer (Asch and Morrison, 1989).

Many authors have used various numerical examples to demonstrate that subsurface features are more easily detected if some or all of the electrodes are placed in the subsurface (Daniels, 1977; Young and Ward, 1985a,b. Beasly and Ward, 1986). Daniels (1983) used a borehole to surface resistivity array to define geoelectric inhomogeneities in a layered volcanic sequence. Le Masne and Poirmeur (1988) used a three-dimensional (3-D) integral equation program to interprete a borehole to surface survey and delineate pyritic conductors

in granite. The same program was also used to interprete a cross-hole survey in a similar environment (Poirmeur and Vasseur, 1988).

This thesis is concerned with similar geometries, but in more conductive terrains with anomalies due to changes in pore fluid resistivity. Wilt et al., (1983) used the 3-D program developed by Dey and Morrison (1979) to model a geothermal reinjection process, and Wilt and Tsang (1985) later used the same program to simulate subsurface contaminant migration. They found that an order of magnitude increase in sensitivity can be achieved when the current source is placed downhole and within the electrolytic contaminant zone. This thesis describes a borehole to surface electrical resistivity field experiment designed to confirm these numerical results by monitoring the injection of a salt water slug into a fresh water aquifer.

In order to predict the field results and subsequently interpret them, a model study was done in conjunction with the field experiment. The 3-D program developed by Dey and Morrison was used to simulate the geological setting of the field experiment and the salt water injection. Two tabular block models were used to simulate a plume of salt water injected into an aquifer at 30 m depth. Models RFS20 and RFS20c are 1 ohm-m blocks 3 m in the z direction, 13 m in the y direction, and 8 m to 10 m in the x direction, respectively. Block model RFS20 is centered on a transmitter electrode at 30 m depth, and model RFS20c is 2 m off-center to the right. This corresponds to the injection of 25,000 gallons into an aquifer of 25 to 30 percent porosity. A second transmitter electrode is located at a depth of 40 m directly below the 30 m electrode making it possible to simulate a dipole transmitter. The dipole-pole potential was calculated for an array of receiver electrodes located along the x direction on the surface.

Curves of potential difference were generated by subtracting the calculated background potential due to the host rock alone from the calculated potential distribution

due to the host rock and the tabular blocks. Asymmetric current channeling in model RFS20c causes the potential in the direction of block displacement to fall off more slowly, so that the difference curve has a positive lobe in that direction (Figure 1.0). These curves represent an anomaly of 25 to 30 percent difference relative to the background potential; this compares to a less than 1 percent difference for surface dipole-dipole results calculated for the same model (dipole separation of up to ten dipole lengths).

Two separate experiments were conducted at the University of California Richmond Field Station (RFS) using different receiver electrode arrays and salt water slugs of different salinity. The first experiment utilized a pole-pole data acquisition configuration with transmitter electrodes on the surface and downhole. The second utilized a pole-dipole arrangement with transmitter electrodes downhole. In both cases, the receiver electrodes were located on lines radiating from the injection well. The data was interpreted using a 3-D resistivity modeling program, and compared to hydrologic measurements taken during the injection. This thesis describes the field experiment, the resistivity monitoring system, and the results.

Chapter One

Experimental Setting

The experiments took place in February 1988 and February 1989 at the University of California Richmond Field Station, an industrial area adjacent to San Francisco Bay and about six miles northwest of the Berkeley Campus. The site was chosen for its accessibility, suitable geological conditions and the availability of a supply of salt water for fluid injection. The well field is located in an open area 400 m north of San Francisco Bay.

Eight wells were drilled to depths ranging from 30 to 40 meters (Figure 1.1) through a section of unconsolidated clay and silt with intermittent lenses of sand and gravel. Analysis of the driller's logs shows that several of the clay horizons can be traced throughout the well field but that many sand and gravel bodies are lenticular connecting three or four of the wells at most (Pouch, 1987). A geologic section at well EXT is presented in Figure 1.2 (After Asch, 1986) as an illustration of the stratigraphy in the field area and the well construction. Pouch (1987) described the rocks as predominantly a deltaic sequence consisting of deposits from San Pablo and Wildcat Canyon Creeks.

Several geophysical methods have been used to characterize the geology of the field site. Among these methods are seismic, electrical resistivity (Wilt et al., 1987), time domain electromagnetics (Wilt and Zollinger, 1986) and a borehole induction log survey (Bevc, 1987). The data from these experiments are adequately interpreted by a four layer model. The surface layer is two meters thick and has a resistivity of 17 ohm-m when dry, and 5 ohm-m when saturated. This is underlain by a thin layer with conductivity thickness product of about 0.5 S and an 11 ohm-m to 13 ohm-m layer extending to a depth of 40 meters and representing the interbedded sequence of deltaic deposits. The whole sequence lies on top of a 50 ohm-m halfspace.

All the wells are cased with PVC plastic. Two of the wells, INJ and EXT, are 15.24 cm (6 inch) in diameter and were designed for fluid injection and withdrawal experiments; these wells have steel sections for current injection. As shown in Figure 1.2 there are metal pipe casing segments at 21.3 m to 22.9 m, at 38.7 m to 40.2 m and a metal screen segment between 30.5 m and 33.5 m. The latter was chosen to allow injection and withdrawal of fluids in the sand and gravel aquifers that are at this depth. The metal electrode segments are connected by individual cables to the current transmitter on the surface. The remaining six holes (OBS1-OBS6) are 10.16 cm (4 inch) diameter wells drilled to depths ranging from 30-35 meters. These wells are open at the bottom and designed for use in water level measurement, downhole water sampling, and subsurface electrical potential measurements.

Piezometric levels were measured in the wells at various dates. These measurements showed that under undisturbed conditions, flow in the vertically confined aquifer was from north to south and the average gradient of the piezometric level was about 0.003. Several pumping tests were carried out in different wells to calculate hydrologic properties of the aquifer. Values of drawdown from observation wells 1, 4, 5, and 6 due to pumping of Well INJ are shown on Figure 1.3 (Javendel, 1987). This figure shows that there is a distinct difference between transmissivity data obtained from Wells 1 and 6. The analysis of this data indicates that the transmissivity of the gravel formation at this location is largest in the west-east direction. Note that these curves represent a point measurement and are aliased in azimuth about the injection well so that they do not sample the bulk ground water flow in all directions.

Salt Water Injection and Extraction Procedure

Salt water for the two injection experiments was obtained from San Francisco Bay and pumped into a 50,000 gallon holding pond 200 meters south of the injection well. Salt and fresh water were pumped into the pond to adjust fluid conductivity. After mixing and settling to remove silt and mud, the water was passed through filters and pumped into the injection well. A total of 25,000 gallons of salt water was injected at an average flow rate of six gallons per minute for 72 hours. The conductivity of the native ground water and the injected salt water were monitored throughout the experiment with a conductance meter. Conductivity probes were located in the injection well just above the screen and at the bottoms of the observation wells.

The conductivity of the native ground water was measured to be 50 to 60 mS/m (20 ohm-m to 17 ohm-m) and the injected salt water was 1.3 S/m and 0.88 S/m (0.76 ohm-m and 1.13 ohm-m) for the first and second experiment, respectively. Since the injection zone is below the water table and the ground water resistivity is known, the resistivity of the intruded formation can be estimated as

$$\rho_{anomalous}=\rho_{formation}\left(\frac{\rho_{salt\ water}}{\rho_{ground\ water}}\right)$$

For a ground water resistivity of 17 ohm-m and a formation resistivity of 11 ohm-m, the intruded zone would have a bulk resistivity of 0.5 ohm-m for the first experiment and 0.75 ohm-m for the second experiment.

Assuming an aquifer thickness of 3 m and a porosity of 20 percent, it is easy to show that a 25,000 gallon (94.5 cubic meter) injection would result in a cylindrical

anomaly of 7 m radius under conditions of isotropic plug flow. No changes in ground water conductivity were measured at the observation wells 15 meters away.

Three days after injection was stopped, extraction was begun from the same well. The salt water was extracted at a rate of 20 gallons per minute for seven days until the outflowing fluid reached the same conductivity as the native ground water. This resulted in a total extraction of 200,000 gallons, eight times the amount injected.

Chapter Two

Multi-Channel Resistivity System

Conventional resistivity surveys are carried out by measuring potential differences on the surface of the earth due to a current electrode pair also located on the surface. The locations of receiver and transmitter electrodes are prescribed by the type of array used, such as Schlumberger, Wenner, or dipole-dipole. The receiver and/or transmitter pairs are moved after each measurement and the measurements are normalized by the current and by the geometry of the array to yield apparent resistivities.

During the first experiment resistivity measurements were made by injecting current at the surface electrodes and at the downhole metal segments of the casing and measuring potentials along north-south and east-west profile lines that intersect at well INJ. A small building at the eastern end of the array was used to house the instrumentation for the experiment. All electrodes were wired into the building and resistivity measurements were made from this one location. For the second experiment, more azimuthal information was obtained by adding receiver electrode lines between the north-south and east-west lines. The receiver electrodes along the north-south and east-west lines were copper sulfate porous pots, while the electrodes along the other lines were iron stakes. These two experiments incorporated two different receiver electrode configurations. The first experiment was conducted with a pole-pole acquisition system and the second a pole-dipole system.

The pole-pole configuration utilized a fixed reference transmitter electrode and a fixed reference receiver electrode. Measurements were made by energizing any one of 40 transmitter electrodes in concert with the reference transmitter electrode to obtain values of potential relative to the reference potential electrode at 76 surface and subsurface locations.

Transmitter and receiver electrodes were evenly spaced along north-south and east-west lines so that many array configurations could be simulated by superposing these pole-pole measurements.

The pole-dipole acquisition system utilized a fixed surface reference transmitter electrode and a set of 130 receiver dipoles. Measurements were made by energizing the borehole current electrodes in concert with the reference transmitter electrode and obtaining values of dipole voltage along eight radial lines on the surface of the earth. These lines radiate from the injection well and consist of up to 17 measurement dipoles.

In most exploration applications, survey accuracy is not of great concern. Gross geological structure is inferred from relative measurements taken over short survey periods (usually one day or less). Although these types of measurements may be precise, they may not be repeatable over longer periods of time or with different sets of equipment. In this experiment accuracy was crucial. System repeatability was maintained by using permanent electrodes and an accurate transmitter-receiver system especially developed for this application.

Instrumentation

The multi-channel resistivity system can be divided into two major elements; the transmitter, and the receiver with its attendant software (Figure 2.1). Precise timing for the system is provided by a crystal clock which generates two synchronized TTL-output square waves. The low frequency square wave (0.05 to 0.2 Hz) controls the transmitter waveform, and the high frequency (10 to 100 Hz) triggers the receiver sampling rate. The actual setting of the low frequency is chosen so as to reduce the effects of telluric noise and electromagnetic inductive coupling. Selection of the high frequency sampling rate is

dependant only on the maximum speed of the scanner and voltmeter and the number of data channels desired.

The transmitter system was originally designed for crustal resistivity monitoring in earthquake prediction studies (Morrison and Fernandez, 1986). It rectifies a three phase 220 or 440 volt input to produce direct current. This input voltage must be isolated in order to prevent ground-loop coupling of the transmitter with the receiver or other instrument grounds. The current polarity is switched by the low frequency signal from the crystal clock to generate an alternating square wave output. The amount of current transmitted is manually controlled by a variac transformer on the input. The current is monitored by a precision resistor serially connected in the output current path. The voltage measured across this resistor is optically isolated in order to prevent coupling between the transmitter and receiver, and is scanned by the voltmeter. The current is scanned before and after each set of potential readings and interpolated so that each reading can be accurately normalized. The transmitter is capable of switching 140 Amps at 600 volts. A current level of 10 to 20 Amps was used for this experiment.

As shown in Figure 2.1 the receiver is subdivided into four components: low pass filters, a Hewlett-Packard 3495A scanner, an HP 3456A digital voltmeter, and an HP 330 computer.

Up to 80 input voltages from the potential electrodes and the serial current resistor voltage from the transmitter are filtered by the four pole Butterworth low-pass filters (Figure 2.2). Each filter chasis contains eight filter circuits with a common ground. These filters are set at 3 Hz to reject 60 Hz noise. For the pole-pole configuration, all the filters share the same isolated 24 volt power supply and the same ground. The power supply ground is at the potential of the reference electrode and the filters are completely isolated from the rest of the system (Figure 2.3). For the pole-dipole configuration each filter

chasis has its own power supply and only two dipole signals pass through each chasis. These two signals share the same ground with the filter power supply. This ground corresponds to the middle electrode of any three consecutive receiver electrodes which constitute two dipoles (Figure 2.4).

The voltmeter measures the filtered signals after they have been sampled sequentially by the scanner. The sampled voltages are stored in the computer for further processing. The average of the ratio of voltage to current and the standard deviation are calculated for every channel and the resulting data is displayed and plotted at the end of every transmitter sequence.

By carefully monitoring the transmitter current, avoiding ground-loops, isolating all the signals, and sampling coherently this system is capable of making measurements to an accuracy of 0.1 percent.

System Transfer Function

Figure 2.5 shows the timing and sampling sequence of the receiver system for the pole-pole configuration. Each current cycle is 10 seconds long and 6 samples are taken every cycle. With a sampling rate of one second, it would be possible to take 10 samples per cycle, but the 1st, 5th, 6th, and 10th are skipped to avoid sampling when the current polarity is changing.

For a sample interval δ, 3 samples in the positive half cycle and 3 samples in the negative half cycle, and a spacing of 3δ between the two groups, the frequency domain transfer function can be written as

$$H(\omega)=\frac{1}{6}[e^{-j\omega t_2}+e^{-j\omega t_3}+e^{-j\omega t_4}-e^{-j\omega t_7}-e^{-j\omega t_8}-e^{-j\omega t_9}]$$

setting $t_2 = 0$ and $t_n = (n-2)\delta$,

$$H(\omega)=\frac{1}{6}[1 + e^{-j\omega\delta} + e^{-j\omega 2\delta} - e^{-j\omega 5\delta} - e^{-j\omega 6\delta} - e^{-j\omega 7\delta}]$$

upon rearranging,

$$H(\omega)=\frac{1}{6}[1 + e^{-j\omega\delta} + e^{-j\omega 2\delta} - [1 + e^{-j\omega\delta} + e^{-j\omega 2\delta}]e^{-j\omega 5\delta}]$$

$$=\frac{1}{6}[1 - e^{-j\omega 5\delta}][1 + e^{-j\omega\delta} + e^{-j\omega 2\delta}]$$

$$=\frac{1}{6}[1 - e^{-j\omega 5\delta}]\frac{[1 - e^{-j\omega 3\delta}]}{[1 - e^{-j\omega\delta}]}$$

Factoring out the exponential terms

$$H(\omega)=\frac{1}{6}[e^{j\omega\frac{5}{2}\delta} - e^{-j\omega\frac{5}{2}\delta}]\, e^{-j\omega\frac{5}{2}\delta}\,\frac{[e^{j\omega\frac{3}{2}\delta} - e^{-j\omega\frac{3}{2}\delta}]e^{-j\omega\frac{3}{2}\delta}}{[e^{j\omega\frac{\delta}{2}} - e^{-j\omega\frac{\delta}{2}}]e^{-j\omega\frac{\delta}{2}}}$$

or

$$H(\omega)=\frac{1}{6}\,\frac{\sin(\omega\frac{3}{2}\delta)}{\sin(\omega\frac{\delta}{2})}\, e^{-j\omega\frac{7}{2}\delta}\, 2j\sin(\omega\frac{5}{2}\delta)$$

rearranging terms,

$$H(\omega)=\frac{1}{6}\,\frac{\sin(\omega\frac{3}{2}\delta)\,\sin(\omega\frac{5}{2}\delta)}{\sin(\omega\frac{\delta}{2})}\,2je^{-j\omega\frac{7}{2}\delta} \qquad (1)$$

If the sampling is done for N cycles and averaged, the transfer function becomes

$$H'(\omega)=H(\omega)\,\frac{1}{30}\sum_{n=0}^{N-1}e^{-j\omega n\delta'}=H(\omega)\,\frac{1}{30}\,\frac{[1-e^{-j\omega N\delta'}]}{[1-e^{-j\omega\delta'}]}$$

for a cycle length of 10 s,

$$H'(\omega)=H(\omega)\,\frac{1}{30}\,\frac{\sin(\omega N\frac{10}{2})}{\sin(\omega\frac{10}{2})}\,\frac{e^{-j\omega N\frac{10}{2}}}{e^{-j\omega\frac{10}{2}}}$$

Inserting expression (1) for $H(\omega)$,

$$H'(\omega)=\frac{1}{180}\,\frac{\sin(\omega\frac{3}{2}\delta)\,\sin(\omega\frac{5}{2}\delta)}{\sin(\omega\frac{\delta}{2})}\,\frac{\sin(\omega N\frac{10}{2})}{\sin(\omega\frac{10}{2})}\,2je^{-j\omega\frac{7}{2}\delta}\,e^{-j\omega\frac{10}{2}(N-1)}$$

If the sampling is stacked for N = 30 cycles, the transfer function of the system is

$$H'(\omega)=\frac{2j}{180}\,\frac{\sin(\frac{3}{2}\omega)\,\sin(\frac{5}{2}\omega)}{\sin(\frac{\omega}{2})}\,\frac{\sin(150\omega)}{\sin(5\omega)}\,e^{-j\omega\frac{297}{2}}$$

using the identity: $\sin(5\omega)=2\sin(\frac{5}{2}\omega)\cos(\frac{5}{2}\omega)$

$$H'(\omega)= \frac{1}{180} \frac{\sin(\frac{3}{2}\omega)}{\sin(\frac{\omega}{2})} \frac{\sin(150\omega)}{\cos(\frac{5}{2}\omega)}$$

where the phase term has been left out.

Finally, setting $\omega=2\pi f$ the transfer function of the system can be written as

$$H'(f) = \frac{\sin(3\pi f)\ \sin(300\pi f)}{180\ \sin(\pi f)\ \cos(5\pi f)}$$

where the current square wave frequency is 0.1 Hz and the sampling frequency is 1 Hz. This is a function with spectral peaks at odd harmonics of the square wave repetition frequency (Figure 2.6).

Figure 2.7 shows the timing and sampling sequence of the pole-dipole receiver system. Each current cycle is 5 seconds long and 12 samples are taken every cycle. Sampling at 4 Hz, it would be possible to take 20 samples per cycle, but the first two and last two samples in each half cycle are skipped to avoid sampling when the current polarity is changing.

For a sample interval δ, 6 samples in the positive half cycle and 6 samples in the negative half cycle, and a spacing of 5δ between the two groups, the frequency domain transfer function is

$$H(\omega)=\frac{1}{12}[\ e^{-j\omega t_3} + e^{-j\omega t_4} + e^{-j\omega t_5} + e^{-j\omega t_6} + e^{-j\omega t_7} + e^{-j\omega t_8}$$

$$- e^{-j\omega t_{13}} - e^{-j\omega t_{14}} - e^{-j\omega t_{15}} - e^{-j\omega t_{16}} - e^{-j\omega t_{17}} - e^{-j\omega t_{18}}$$

Proceeding as for the pole-pole configuration, the transfer function of the system can be written as

$$H'(f) = \frac{\sin(\frac{3}{2}\pi f)\,\sin(150\pi f)}{360\,\sin(\frac{1}{4}\pi f)\,\cos(\frac{5}{2}\pi f)}$$

where the current square wave frequency is 0.2 Hz and the sampling frequency is 4 Hz. A plot of this transfer function is presented as Figure 2.8.

Measurement Noise and System Repeatability

An estimate of measurement noise can be made by multiplying the spectral density function of noise at the field site with the transfer function of the system. This corresponds to a convolution of the telluric noise time series with the filter function of the system. Figure 2.9 is a plot of a typical telluric spectrum at Richmond for a 5 m measurement dipole. At the first harmonic spectral window of the pole-dipole transfer function (0.2 Hz) this spectrum has a value of 300 $\mu V/\sqrt{Hz}$ (the noise bandwidth of the spectrum analyzer is 30 mHz at this range). The half width of the transfer function's first spectral window is 0.008 Hz. Squaring the amplitude of the spectrum and multiplying by the width of the spectral window gives a variance of 0.72 nV^2, or a standard deviation of 27 μV. If the measurements are made with a transmitter current of 15 A, the standard deviation due to telluric noise should be 1.8 $\mu V/A$.

Figure 2.10 is a plot of normalized voltage for the pole-dipole system. This data was taken with a current electrode at 30 m depth and 5 m receiver dipoles along the south-north line. The signal varies from about 2700 $\mu V/A$ to 5000 $\mu V/A$. Comparing this to the

noise estimate in the preceding paragraph (1.8 μV/A) suggests a standard deviation of about 0.07 to 0.04 percent.

The actual standard deviation of the data (Figure 2.11) is in the 0.05 to 0.1 percent range for all but a few isolated data points. This compares reasonably with the average estimated value. Comparing this noise level to the signal of Figure 2.10 we can interpret the bumps in the curve to be due to geology, not noise. Isolated noisy data points (such as receiver dipole 15) were excluded from the data analysis presented in this thesis. This type of noise usually persisted at a given location and is most likely due to a bad receiver wire or electrode, or the proximity of a cultural noise source such as a grounded fence or pipe.

Since this thesis is concerned with temporal measurements it is essential to insure that measurements taken on different days repeat within the calculated standard deviation if no geological or hydrological change has taken place. Figure 2.12 is a plot of percent difference for measurements taken on two consecutive days. Most of these readings are within 0.1 to 0.2 percent of each other, and therefore, within acceptable error tolerance.

It is also interesting to determine what effect rainfall has on repeatability. The largest amount of rain fell before salt water injection began. According to local newspapers, this ten hour period resulted in half an inch of precipitation. Measurements taken before and after the rain show a maximum difference of about 3 percent (Figure 2.13). These changes are due to resaturation of the surface layer and alteration of current flow paths due to standing water around the electrodes. Only light rain fell occasionally during the actual injection experiment. A plot of percent difference taken on two consecutive days with maximum salt water injected (Figure 2.14), shows that the repeatability of the readings is well within 1 percent. For most dipoles it is within 0.5 percent. This is well within tolerance considering that the expected anomaly is 25 to 30 percent. Even an error of 3 percent would allow for detection.

Since the pole-dipole data was superposed to create dipole-dipole data and superposition of noise propagates error, it is interesting to examine the repeatability of the superposed data. Figure 2.15 is a plot of the maximum injection dipole-dipole repeatability for data taken with 30 m and 40 m current electrodes on the same day as the data of Figure 2.14. Most of the dipoles repeat to within 2 percent.

The measurement accuracy of the acquisition system is 0.1 percent. Repeatability is degraded by changes in surface resistivity caused by rain, but remains within 0.5 percent. Even in the worst case, when the data taken during a period of light rain is superposed, the repeatability is better than 2 percent.

Chapter Three

Electrical Resistivity Monitoring

The two different receiver electrode arrays were used for two separate experiments at the same field site. The first experiment generated a complete set of surface and borehole to surface data along two intersecting receiver lines. The second experiment was done as a follow-up to the first.

For the first injection experiment a complete data set was taken before salt water injection, at maximum volume injected and after salt water extraction. This full data set was generated by energizing 40 surface and borehole current electrodes and measuring potential at 76 electrodes for each current source. A partial data set collected with current sources at the 30 and 40 meter levels of the INJ and EXT wells and potentials measured at all 76 electrodes was taken every day during the injection and extraction procedure. The experiment was started during a period of dry weather but heavy rains began on the second day of injection. This period of rain introduced noise into the measuring system in the form of short-circuits at some of the electrodes.

During the second injection experiment, data was taken by energizing the 30 m or 40 m transmitter electrodes in well INJ and measuring 17 dipole potentials along any half of one line at a time. Measurements were taken every day during the injection and extraction procedure.

Although analysis of the first data set suggested that superposing pole-pole data to form dipole-pole data was best, the second set was gathered as pole-dipole and transformed into dipole-dipole. This was done for two reasons: 1) The signal levels and standard deviations of the pole-pole data are such that the subsurface data cannot be superposed into pole-dipole or dipole-dipole without introducing an excessive error and analyzing dipole

voltage may really be the preferred approach since some model studies show it to be more sensitive to changes than pole voltage (Eloranta, 1985). 2) The pole-dipole configuration was chosen for convenience because it was desired to make the acquisition system more portable in order to conduct larger scale surveys. Measuring dipole potentials reduces the dynamic range requirements of the digital voltmeter and minimizes electromagnetic coupling effects. Also, the logistic problem of locating a reference receiver electrode in a noise free and convenient location was eliminated.

Throughout this thesis the measurement results are presented as either apparent resistivity or normalized voltage. The normalized voltage is the observed voltage divided by the injected current. In order to facilitate discussion, the normalized voltage is refered to as potential when the data is gathered with the pole-pole acquisition system and as voltage when gathered with the pole-dipole system.

Surface Resistivity Monitoring

Figure 3.1 is a surface dipole-dipole apparent resistivity pseudosection along the south-north line generated by superposing the pole-pole data. Apparent resistivities range from 10 to 25 ohm-m within the pseudosection and increase with larger n-spacing or greater depth. The profile does not show any large lateral variations in resistivity although there are some indications of near surface inhomogeneities.

Figure 3.2 is a dipole-dipole pseudosection along the same line after salt water was injected into the aquifer. Some of the electrodes were short-circuited by rain, and that data has been omitted from the pseudosection. The percent difference of the two data sets (Figure 3.3) shows that there is no significant change in apparent resistivity for low n-spacing, and that the rain fall did not have a significant effect on the surface layer

resistivity. The isolated points of high percent difference can be attributed to short circuit noise from wet electrode wires and standing water. These variations are of such high spatial frequency that they cannot possibly be attributed to changes in formation resistivity.

The main reason for this insensitivity to the salt injection is that a relatively small volume of rock is affected by the salt water compared to the volume of rock sampled by the measurements.

Borehole to Surface Resistivity Monitoring

Since the zone of interest is at depth, the greatest change in the measurements is observed when the transmitter electrodes are located in the sub-surface. To investigate the sensitivity of various arrays, the measured pole-pole potentials were superposed to create pole-dipole, dipole-dipole, and dipole-pole potentials for apparent resistivity calculation.

The measured borehole to surface pole-pole potential before and after salt water injection is presented as Figures 3.4 and 3.5. The potential is negative for electrode locations beyond electrode number 12 because the reference electrode is located 60 m east and 10 m south of the center of the array. Since all potentials are measured relative to this reference electrode they are positive for locations within about 60 m (around electrode number 12) of the center of the array, and negative for locations more than about 60 m from the center.

The time difference of these curves (Figure 3.6) shows a strong asymmetric anomaly due to the presence of the salt water. Before attempting an interpretation of this data it is interesting to calculate apparent resistivities for various superpositions of the data and try a few temporal and spatial differencing schemes. This data manipulation should reveal the optimal way to present and acquire the data.

Pole-Pole Apparent Resistivity

Since the reference receiver electrode is within the array, the potential is relatively small at locations near 60 m from the array center. This causes difficulty in calculating pole-pole apparent resistivities. The spikes in the apparent resistivity curves (Figures 3.7 and 3.8) are due to two related factors: 1) The geometric factor in the apparent resistivity calculation develops an instability 60 m from the array center and is very sensitive to the exact electrode location. 2) The error in the readings becomes a proportionaly larger percentage of the observed value at these locations.

Noise due to possible near surface lateral heterogeneities can be minimized by differencing the data from some background level. This may be done by computing the percent difference of the data taken with the current electrode at the 30 m level relative to data taken with the current electrode at the 40 meter level. Here, the percent difference is defined as

$$\frac{(\rho_{30} - \rho_{40})}{\rho_{40}} * 100$$

where ρ_{30} is the apparent resistivity due to a current source at 30 meters and ρ_{40} is the apparent resistivity due to a current source at 40 meters (Asch and Morrison, 1989). The curves in figures 3.9 and 3.10 were obtained using this scheme for the baseline and maximum injection data. Although the data is smoother, this scheme did not remove the instability around electrode 12. Taking the time difference of this spatially differenced data does not eliminate the spikes either (Figure 3.11). This figure does show more asymmetry

in the north-south direction than in the east-west (as does figure 3.6), but it is difficult to choose reliable data points near electrode number 12.

The plot of potential difference (Figure 3.6) shows a pronounced asymmetry with less error and distortion than the plot of temporal percent difference (Figure 3.11). The potential difference plot seems to be the best way to present this data. However, the anomaly is only 1 to 2 mV/Amp. This is an anomaly of only about 5 percent. Examining Figures 3.1, 3.2 and 3.6, one could speculate that subtracting the 30 m potential from the 40 m potential to create a dipole transmitter would create a smaller primary field, and a larger difference. Dipole receivers would result in a quantity proportional to the gradient of the potential (electric field). Therefore, it seems that some superposition of the data into dipole transmitter and/or dipole receiver should enhance the anomaly.

Superposition of Borehole to Surface Pole-Pole Data

Figure 3.12 is a plot of the superposed pole-dipole apparent resistivity along the north-south and east-west lines due to pole sources at the 30 and 40 meter levels of well INJ before salt water injection. Although the noise level of the pole-pole measurements is very small (0.1 percent), This superposed data is very noisy. The same effects are evident after maximum salt water injection (Figure 3.13). Since dipole measurements are analogous to measuring electric field, and electric field is discontinuous at resistivity contrasts, the pole-dipole data is expected to be somewhat noisier. However, the differencing scheme of Asch and Morrison (1989) should remove this type of noise if it is really due to geological structure.

The curves in figures 3.14 and 3.15 are the spatial percent differences of the baseline and maximum injection data. The spatial percent difference is defined in the same

way as for the pole-pole case. Although the data is still noisy, it is an improvement over the superposed pole-dipole data. Subtracting the baseline percent difference from the percent difference at maximum injection yields the time differenced data of Figure 3.16. Here we see a pronounced but very noisy low about the center of the array corresponding to the effect of the injected salt water.

Figures 3.17 and 3.18 are plots of dipole-dipole apparent resistivity obtained by superposing data from the 30 m and 40 m level electrodes at well INJ to simulate a transmitter dipole and receiver dipoles. As in the pole-dipole case, this configuration is also noisy. Figure 3.19 is the temporal percent difference of the dipole-dipole apparent resistivity. Temporal percent difference is defined as

$$\frac{(\rho_{After} - \rho_{Baseline})}{\rho_{Baseline}} * 100$$

The dipole-dipole percent difference (Figure 3.18) is noisier than the pole-dipole (figure 3.16) because more superposition of noisy data is required to create the dipole-dipole potentials. Since there is only one subsurface dipole, the dipole-dipole data cannot be differenced relative to a particular depth.

In both cases the superposed data is so noisy that a precise interpretation is not possible. All that can be said is that some change took place. Since percent differencing the data with respect to depth or time did not remove the noise, the noise cannot be solely due to surface heterogeneities. The noise is due to the fact that the data is gathered as pole-pole voltages and then superposed to simulate pole-dipole and dipole-dipole voltage. Each of the pole-pole readings has an associated standard deviation, so that superposition of these readings in combination with the geometric factor increases the standard deviation. This can be demonstrated by investigating a simple numerical example.

For the sake of discussion, assume a model with half-space resistivity 4π ohm-m. The normalized voltage at a point on the surface directly above (at x = 0 m) a transmitter electrode at 40 m depth is given by

$$\frac{V}{I} = \frac{\rho}{2\pi r} = \frac{2}{40} = 0.05 \text{ V/Amp}$$

similarly, at x = 5 m on the surface, the normalized voltage is 0.049613893 V/A. Subtracting these two pole voltages the dipole voltage between a 0 m and 5 m receiver electrode is 0.38617 mV/A. If the pole voltages have a 0.1 percent error (i.e. standard deviation of 0.05 mV/A), this is a 12.9 percent error for the dipole voltage. For a transmitter at 30 m depth, the normalized voltage at x = 0 m is 0.0666 V/A. This can be combined with the voltage due to the 40 m transmitter to get a dipole-pole normalized voltage of 0.01666 V/A. For this configuration, a pole-pole error of 0.1 percent translates into a dipole-pole error of 0.3 percent. From these numerical examples it is evident that the superposition of pole-pole data to create surface dipoles leads to unacceptable error propagation, while superposition of the data to create subsurface dipole transmitters remains within acceptable error tolerances.

In an attempt to eliminate the noise problems due to superposition, the data were superposed to simulate a dipole-pole configuration. Figures 3.20 and 3.21 are plots of potential due to a dipole source before and after salt water injection. Subtracting the baseline potential from the potential at maximum injection gives curves of potential difference (Figure 3.22). The maximum anomaly of about 2 mV/A represents a change of approximately 25 percent over the base line value. A notable feature of this data is the pronounced asymmetry of the curves comparable to the model results presented in the introduction.

Figures 3.23 and 3.24 show the apparent resistivity due to a simulated dipole source with transmitter electrodes at the 30 and 40 meter level of well INJ, and surface receiver poles. These results are seen to be much cleaner than those for superposed pole-dipole or dipole-dipole but there is still some noise in the data. Some data points have been dropped from the apparent resistivity calculation to avoid noise due to inaccuracies in the geometric factor and the location of the reference electrode. Figure 3.25 is a plot of temporal percent difference for the dipole-pole apparent resistivities. This shows a substantial improvement over the pole-dipole and dipole-dipole cases.

As found by Eloranta (1985), analyzing differences in potential rather than apparent resistivity turns out to be best. Although the percent difference plot (Figure 3.25) shows a distinct asymmetric anomaly, the potential difference plot (Figure 3.22) shows a sharper anomaly with more distinct features. The potential difference curves develop distinct positive lobes at distant electrode locations and sharp peak amplitudes near the array center. Also, more data is shown in the potential difference curves because some of the data was dropped from the apparent resistivity and percent difference calculations.

The sensitivity of borehole to surface measurements for source locations outside the anomalous body may be investigated by looking at the data for a dipole source in well EXT. The current electrodes at the surface and 30 m were used because the 40 m electrode at well EXT was short-circuited by rain. The dipole-pole differences are shown in Figure 3.26. This shows a weak but pronounced anomaly consistent with the numerical model studies of Wilt and Tsang (1985) for current sources outside the injection zone. Note that the largest change in potential occurs over the transmitter electrode location (receiver number -12).

Interpretation of Dipole-Pole Potential Data

Analytical and numerical modeling programs were used to qualitatively interpret the results of this experiment. An analytical solution was used to model the layering sequence at RFS and the 3-D finite difference program discussed in the introduction was used to model the effects of the conductive salt water slug. Computer memory limitations constrained the finite difference mesh size to 55 by 16 by 20 nodes on the IBM 3090. This makes it difficult to include the layered stratigraphy and to adequately discretize the area around the current source while allowing the potential to fall off properly at the edges of the mesh. These computer size restrictions do not allow a large enough mesh to simulate spheroidal or cylindrical bodies with this algorithm.

Because of the limited mesh size, the potential gradients are not approximated correctly by the program and the potential does not fall off properly. This results in a noisy looking curve. With these modeling limitations the program can give only a crude qualitative approximation of the field situation for such a small and relatively deep body. A larger mesh size would allow for better discretisation of the anomalous body. The tabular models could then be replaced with much more accurate 3-D representations of the saline intrusion and the complex layering sequence at the site could be better represented.

The layer model used to represent the geology of the field site has a 2 m thick surface layer of 17 ohm-m underlain by a 38 m thick 11 ohm-m layer, all over a 50 ohm-m halfspace. The fit of this layer model to the field data can be demonstrated by calculating an analytical model and varying the middle layer resistivity (Figure 3.27). The model with 11 Ohm-m middle layer fits the field data the best. Figure 3.28 is a schematic diagram of the model halfspace with salt water block RFS20 in place.

Figures 3.29 and 3.30 are plots of calculated potential difference due to a dipole transmitter with electrodes at the 30 m and 40 m levels. The models used to generate these curves are exactly like those presented in the introduction, except that the tabular blocks for the RFS10 series models are only 2 m thick. Models RFS10 and RFS20 are blocks centered on a transmitter electrode at 30 m depth, and models a through c are progressively off-center to the right (Figure 3.31). A resistivity of 1 ohm-m was assigned to all the blocks because the size and geometry are so constrained by the mesh that varying the resistivity by 50 percent does not have as much effect as varying the size and geometry would.

Comparing the RFS10 and RFS20 model series gives an indication of the sensitivity of these types of measurements to the size and relative position of the anomalous body. The RFS20 bodies are comparable in volume to that anticipated for the salt water intruded zone in the aquifer with about 20 percent formation porosity (472.5 cubic meters). The RFS10 series models would correspond to a porosity of about 30 percent. Mesh size restrictions do not allow the variation of resistivity, shape and size of the body to define or constrain these parameters by iterative modeling. Also, the mesh size in the y dimension is so limited that the body cannot be displaced in that direction. Since run time for these models is about 20 minutes on the IBM 3090, successive forward modeling or data inversion is impractical and prohibitively expensive. With these modeling constraints, the best interpretation that can be achieved is to fit the model results to the observed data on a line by line basis as if the body were off-center in only one direction.

The model curves have a positive lobe on the side corresponding to the direction in which the body is offset. The position of the curves minima and its amplitude also changes as the body is moved off-center. Comparing the south-north difference data (Figure 3.25) to the model curves indicates a fit between models RFS10b and RFS20b. This

corresponds to a displacement of the body to the north and a porosity of 20 to 30 percent. The character of the west-east data indicates a displacement to the west consistent with models RFS10a and RFS20a. Therefore, the resistivity data indicates that the plume is displaced to the northwest, and the bulk transmissivity is greatest in this direction. This differs from the conclusion derived from the drawdown test (Figure 1.3), which indicates that the maximum transmissivity is to the east.

Pole-Dipole Electrical Monitoring

The second injection experiment was done to confirm that the bulk formation transmissivity was greatest to the northwest by adding two new lines of receiver electrodes at 45 degrees to the south-north and west-east lines.

Figure 2.10 is a plot of pole-dipole voltage along the south-north line before salt injection. This curve is not as smooth as the potential of Figures 3.23 or 3.24 because it is proportional to electric field, and electric field is discontinuous at resistivity contrasts. However, it is not as noisy as the superposed pole-dipole apparent resistivity curves (Figures 3.12 and 3.13).

Dipole-Dipole Potential Monitoring

Figure 3.32 is a plot of pole-dipole data along the south-north line after maximum salt water injection. On this scale the before and after curves (Figures 2.10 and 3.32) are difficult to tell apart. The maximum anomaly is only about 0.24 mV/A, or 5 percent. As in the pole-pole case, the anomaly can be enhanced by superposing the pole-dipole data from the 30 m and 40 m transmitter electrodes to create dipole-dipole voltage. This decreases the

effective amplitude of the observed voltages. A plot of superposed dipole-dipole voltage for all the lines is presented as Figures 3.33 and 3.34. Figure 3.35 is the difference between the maximum injection data (Figure 3.34) and the baseline data (Figure 3.33). This data shows a maximum anomaly of about 40 percent.

The dipole-dipole voltage for model series RFS21 (Figure 3.36) can be used to interpret the curves of Figure 3.35. The results in Figure 3.36 are for a series of blocks displaced to the left (Figure 3.37). The models are otherwise identical to the RFS20 series.

There are several salient features to these model curves. The amplitude of the anomaly increases on the side corresponding to the direction of block displacement and the zero crossing shifts away from the direction of displacement. Also, the curves for the displaced blocks intersect the curve for the centered block. This intersection occurs at lower receiver number for greater block displacement.

Analyzing the data of Figure 3.35 in light of these model results confirms the conclusion that the direction of maximum transmissivity is northwest. The amplitude of the northwest-southeast curve is maximum to the left, which is the northwest side of the line. The zero crossing is displaced to the southeast, indicating displacement to the northwest. For the other three lines, maximum displacements occur to the (in order of magnitude) west, north, and northeast. Since the northwest-southeast data shows the greatest amplitude, this must correspond to the direction of maximum bulk ground water flow.

Conclusion

This thesis demonstrates that the borehole to surface electrical resistivity monitoring system is capable of gathering data accurately enough to map subsurface ground water flow. The injected plume of salt water moved asymmetrically into the northwest quadrant from the injection hole. The pressure during drawdown tests indicated major transmissivity to the east although no test wells are available to measure transmissivity to the northwest. The resistivity results suggest strong channel flow paths that could not be determined by a limited number of observation wells, but which are clear in the resistivity results.

The choice of how to present electrical data was seen to be dependant on how the data was gathered. In this case, looking at time differences of potential, instead of apparent resistivity yields cleaner results that allow for easier interpretation.

The chief limitation to this method lies in the lack of adequate interpretive tools. The development of a new program with greatly expanded mesh size and much quicker run time would enable more detailed and accurate interpretation of field data. If the plume boundary could be accurately modeled, the porosity and transmissivity of the aquifer could be determined. This method would then move from the realm of reconnaissance and detection, to precise engineering application.

References

Asch, T. and Morrison, H. F., 1989, Mapping and monitoring electrical resistivity with surface and subsurface electrode arrays. Geophysics, v. 54, pp. 235-244.

Asch, T. 1986, Personal comunication.

Beasley, C. W., and Ward, S. H., 1986, Three-dimensional mise-a-la-masse modeling applied to mapping fracture zones. Geophysics, v. 51, pp. 98-113.

Bevc, D. 1987, Borehole electromagnetic survey of the Engineering Geoscience well field at the Richmond field station: data presentation. Engineering Geoscience Report, University of California, Berkeley CA 94720

Daniels, J. J., 1977, Three-dimensional resistivity and induced polarization modeling using buried electrodes. Geophysics, v. 42, pp. 1006-1019.

Daniels, J. J., 1977, Hole-to-surface resistivity measurements. Geophysics, v. 48, pp. 87-97.

Dey, A. and Morrison, H. F., 1980, Resistivity modeling for arbitrarily shaped three-dimensional structures. Geophysics, v. 44, p. 753-780.

Eloranta, E.H., 1985, A comparison between mise-a-la-masse anomalies obtained by pole-pole and pole-dipole electrode configurations. Geoexploration, v. 23, p. 471-481.

Javandel, I. 1988, Personal comunication. Earth Sciences Division, Lawrence Berkeley Laboratory, University of California, Berkeley, CA 94720.

Le Masne, D., and Poirmeur, C., 1988, Three-dimensional model results for an electrical hole-to-surface method: Application to the interpretation of a field survey. Geophysics, v. 53, pp. 85-103.

Morrison, H. F. and Fernandez, R., 1986, Temporal variations in electrical resistivity of the earth's crust. Jour. Geophys. Res., v. 91, no. B11, pp. 11618-11628.

Poirmeur, C., and Vasseur, G., 1988, Three-dimensional modeling of a hole-to-hole electrical method: Application to the interpretation of a field survey. Geophysics, v. 53, pp. 402-414.

Pouch, G. W., 1987, Hydrogeologic site assessment of the Engineering Geoscience well field at the Richmond field station, Contra Costa County, California. MS Report, Engineering Geoscience, University of California, Berkeley CA 94720.

Rodriguez, E. B., 1984, Ground water contamination studies in Ontario. Proceedings from surface and borehole geophysical methods in ground water investigation, February 6-9, San Antonio, TX.

Saunders, W. R. and Stanford, J. A., 1984, Integration of individual geophysical techniques as a means to characterize an abandoned hazardous waste site. Proceedings

from surface and borehole geophysical methods in ground water investigation, February 6-9, San Antonio, TX.

Van Overmeeren, R. A. 1989, Aquifer boundaries explored by geolectrical measurements in the coastal plain of Yemen: A case of equivalence. Geophysics, v. 54, pp. 38-48.

Wilt, M. J. and Tsang, C. F., 1985, Monitoring of subsurface contaminants with borehole/surface resistivity measurements. Proceedings from surface and borehole geophysical methods in ground water investigation, February 12-14, Fort Worth, TX.

Wilt, M. J., Pruess, K., Bodvarsson, G. S. and Goldstein N. E., 1983, Geothermal injection monitoring with dc resistivity methods. Procedings of the Geothermal Resoources Council annual meeting, October 24-27, Portland, OR.

Wilt, M. J. and Zollinger, R., 1986, personal comunicatiion.

White, P. A., 1988, Measurement of ground water parameters using salt water injection and surface resistivity. Ground water, v. 26, pp. 179-186.

Yang, F. W., and Ward, S. H., 1985a, Single-borehole and cross-borehole resistivity anomalies of thin ellipsoids and spheroids. Geophysics, v. 50, pp. 637-655.

Yang, F. W., and Ward, S. H., 1985b, On sensitivity of surface-to-borehole resistivity measurements to the attitude and the depth to center of a three-dimensional spheroid. Geophysics, v. 51, pp. 1978-1991.

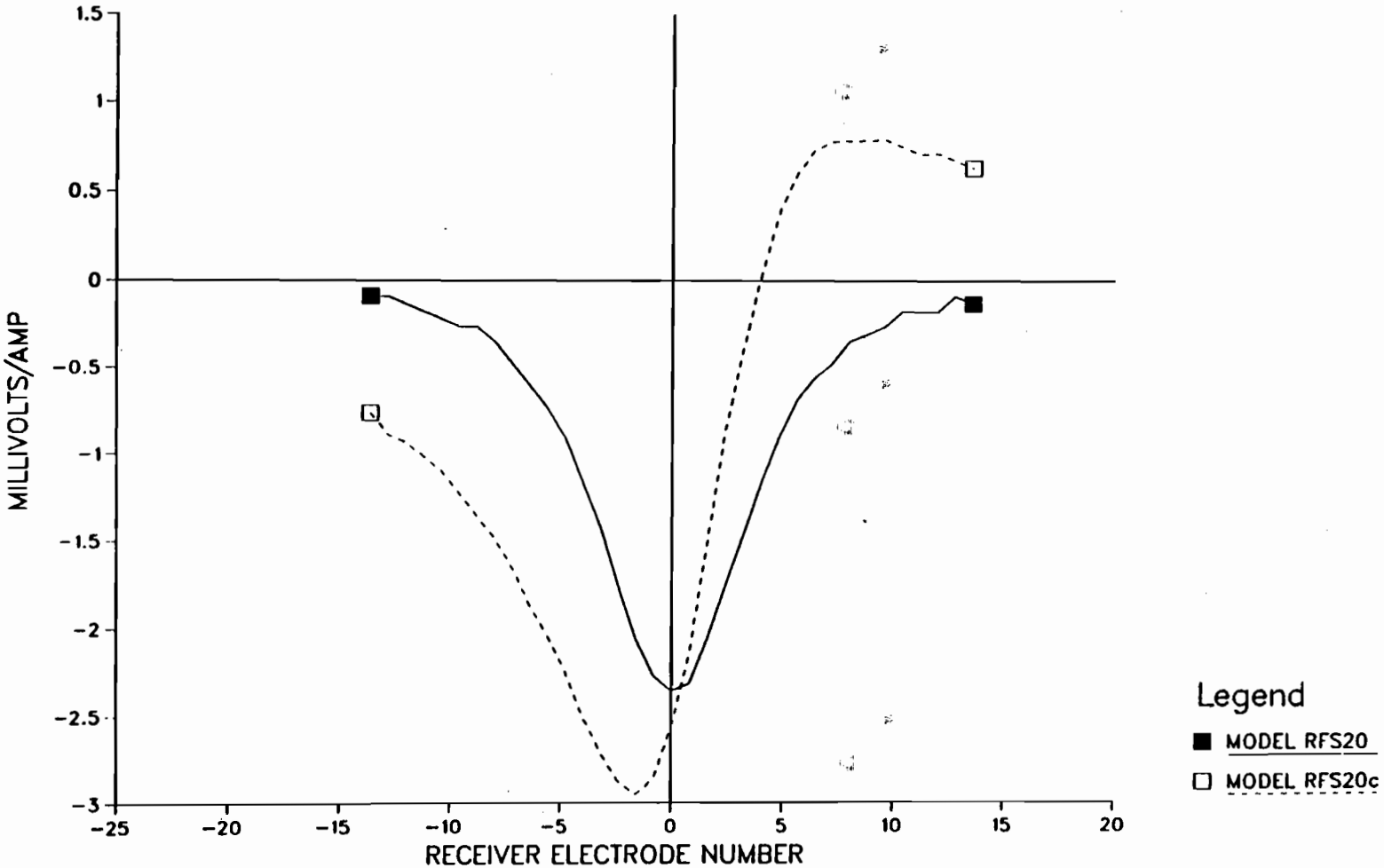

Figure 1.0. Three-dimensional finite difference model results for the borehole to surface configuration. These curves of potential difference were generated by subtracting the calculated potential for the halfspace without the salt water from the potential calculated with the salt water in place.

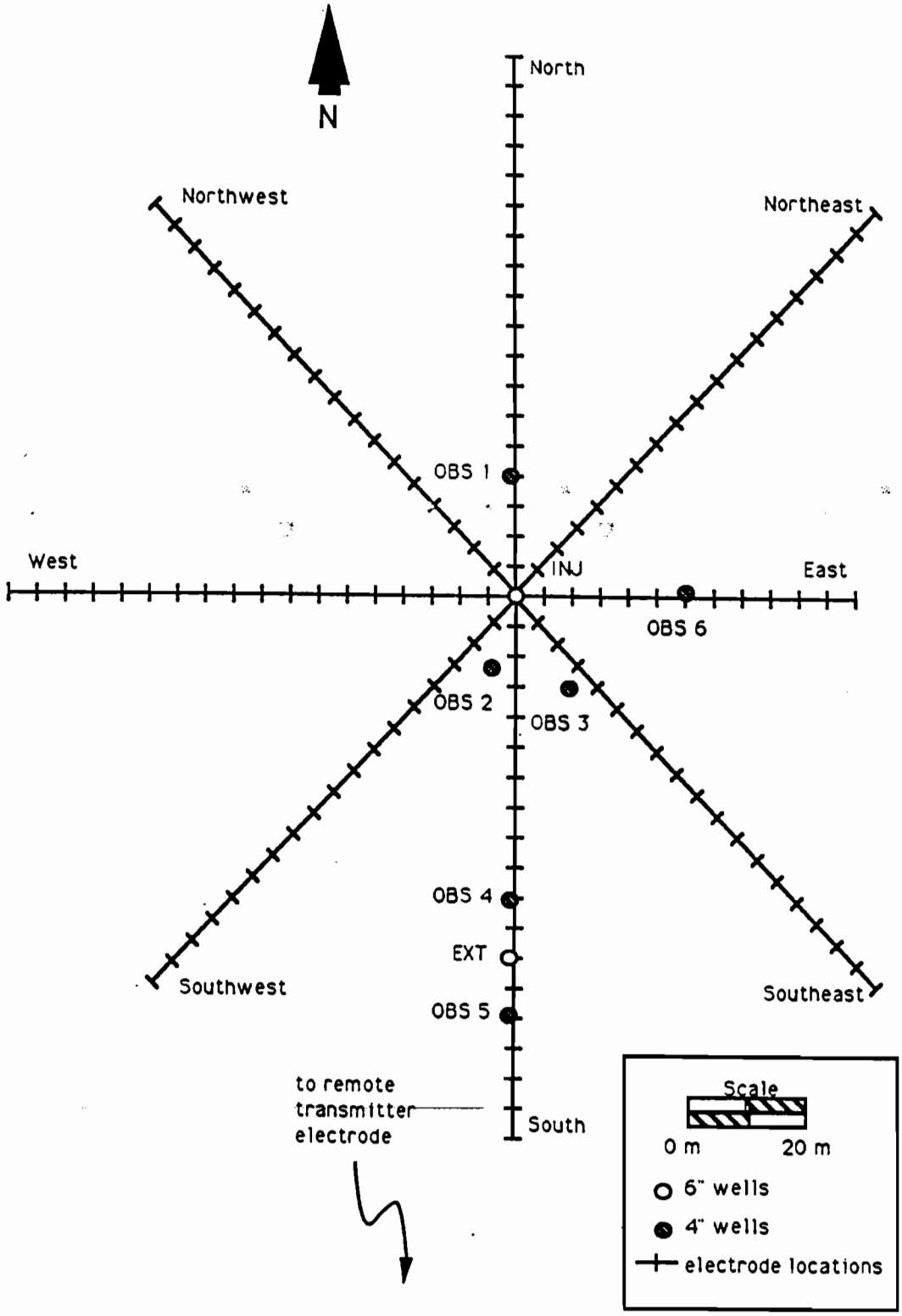

Figure 1.1. Plan map of the well field and resistivity array at the Richmond Field Station.

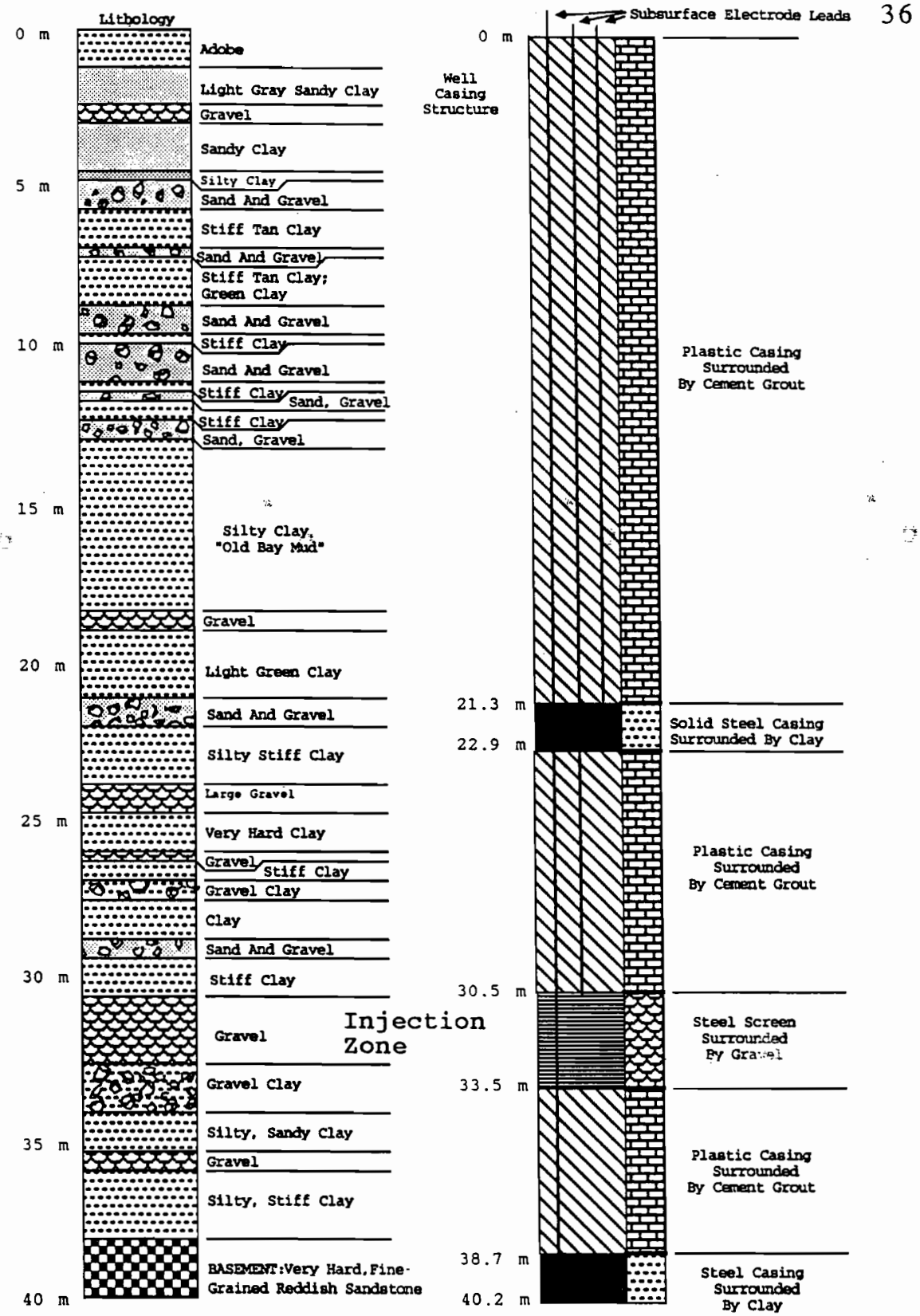

Figure 1.2. Stratigraphy and well construction at well EXT.

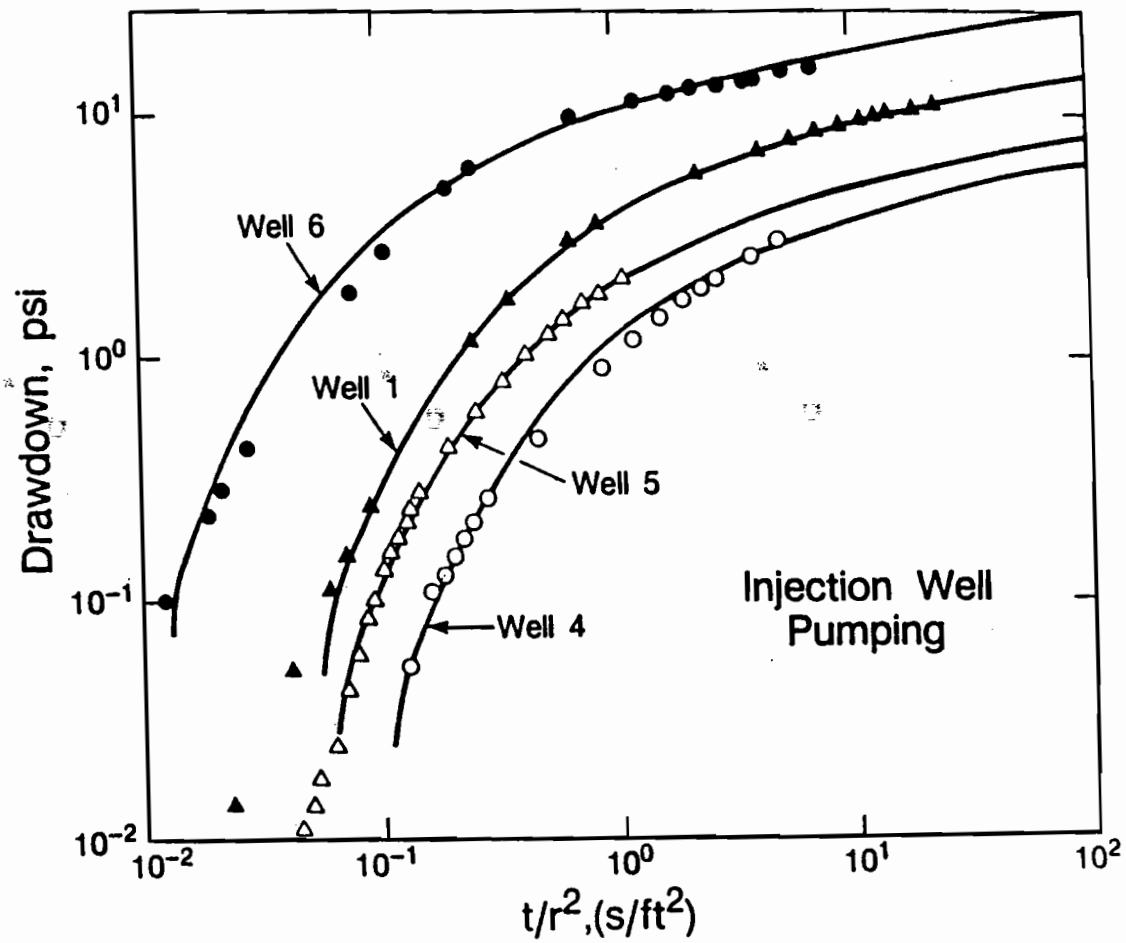

Figure 1.3. Comparison of drawdown from pumping tests at the Richmond Field Station (Javendel, 1987).

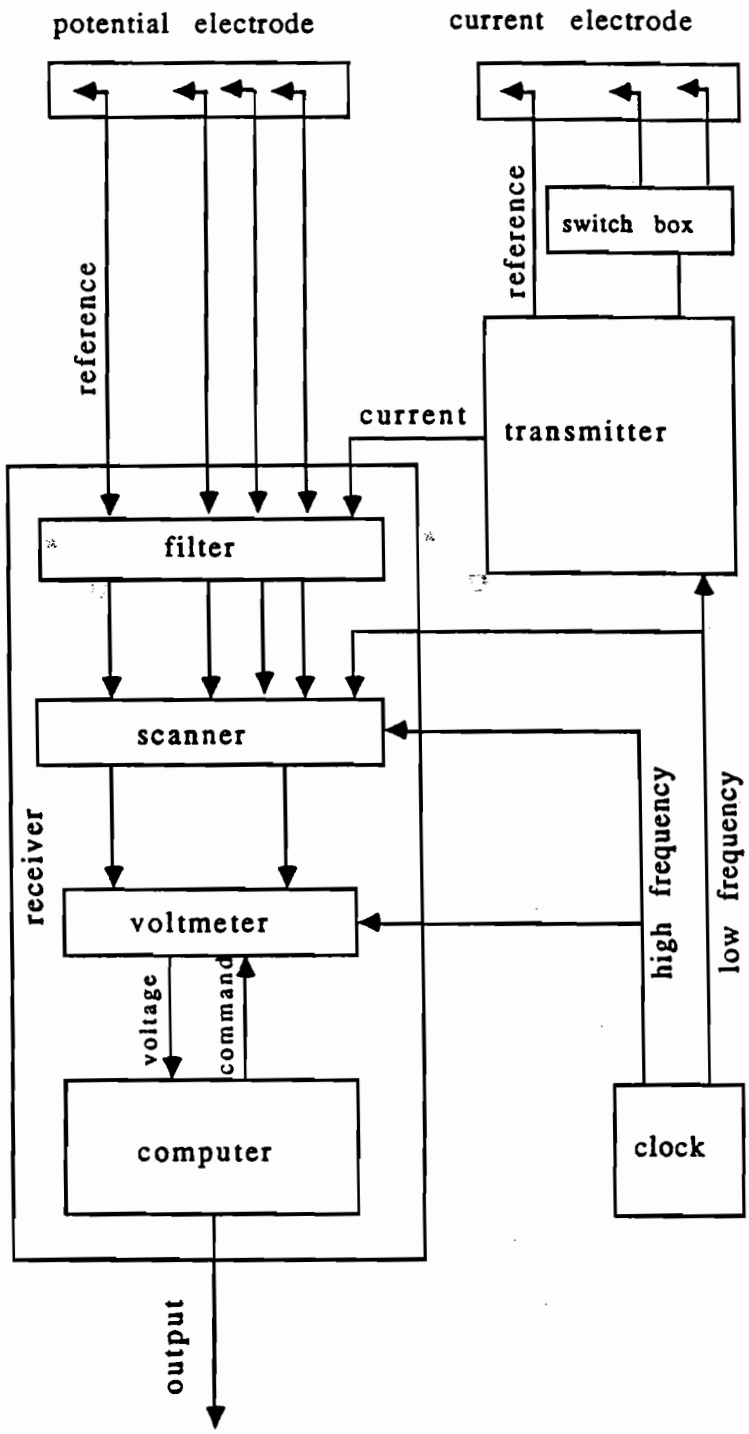

Figure 2.1. Schematic diagram of the multi-channel resistivity monitoring system.

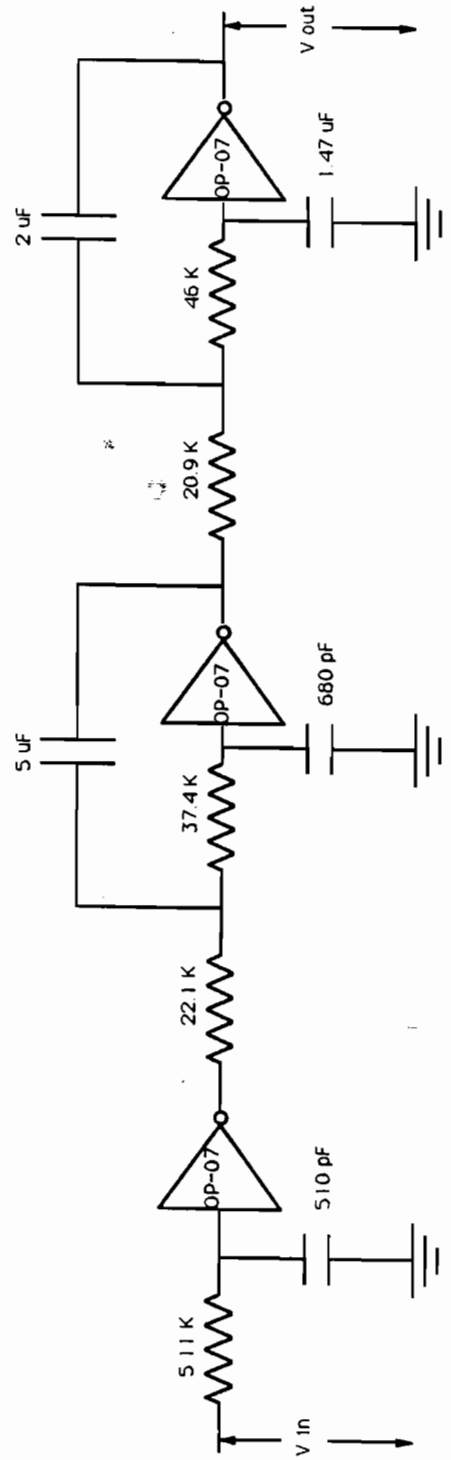

Figure 2.2. Circuit diagram of the 4 pole Butterworth filter with -3 dB point set at 3 Hz. Each filter chasis is powered by two 12 volt batteries and has eight of these circuits in it.

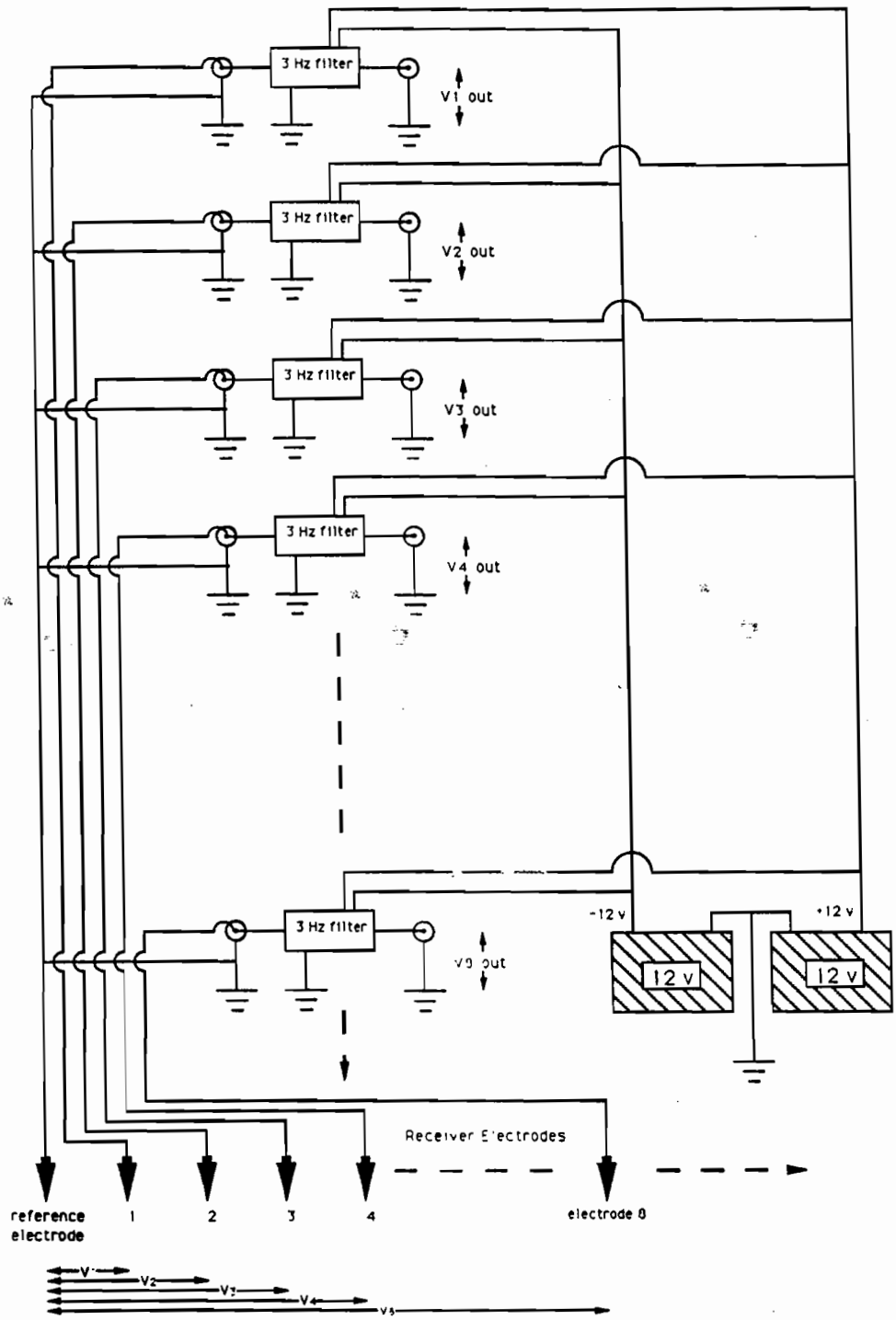

Figure 2.3. Schematic diagram of the filter set up for the pole-pole acquisition system

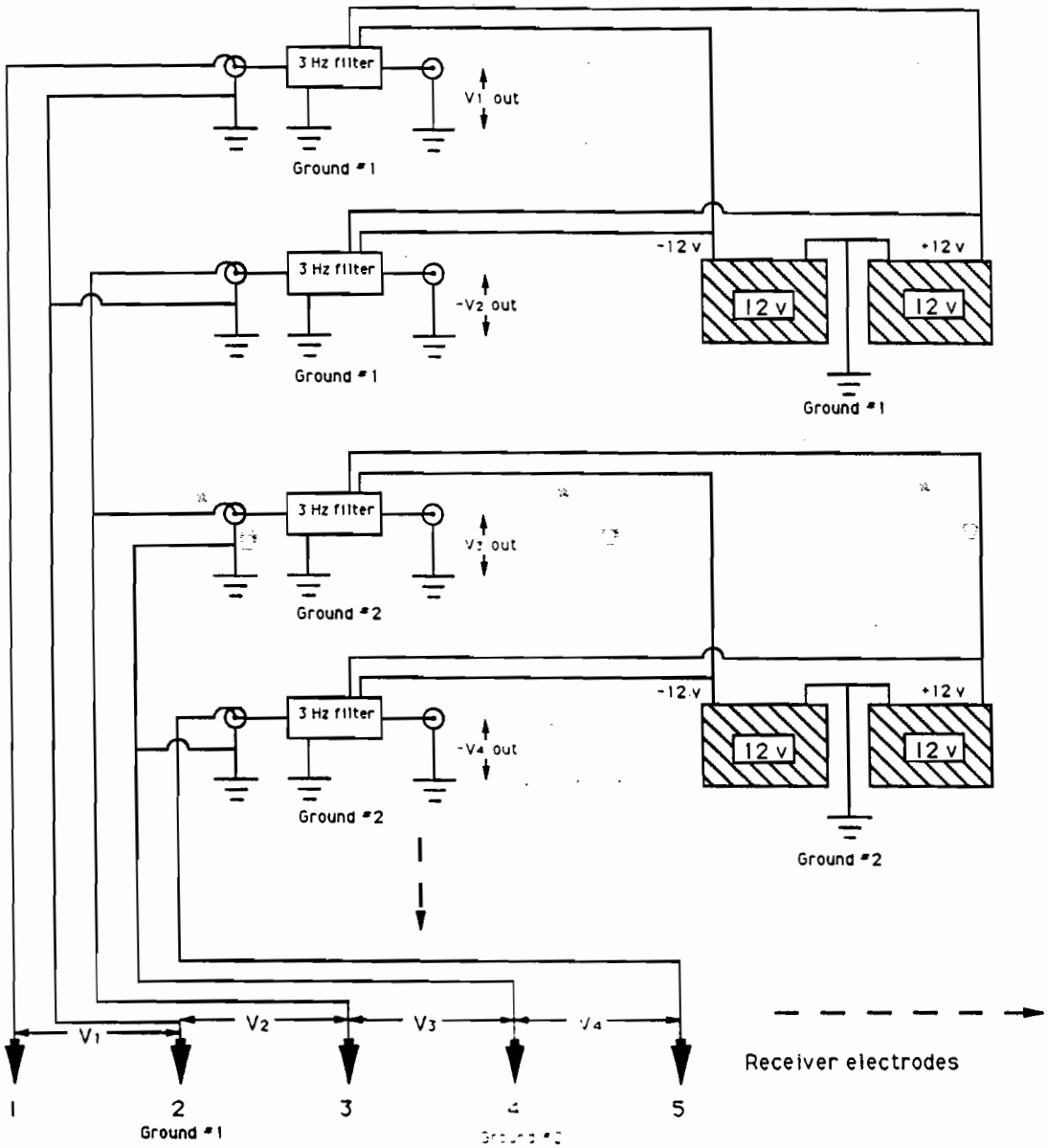

Figure 2.4. Schematic diagram of the filter set up for the pole-dipole acquisition system.

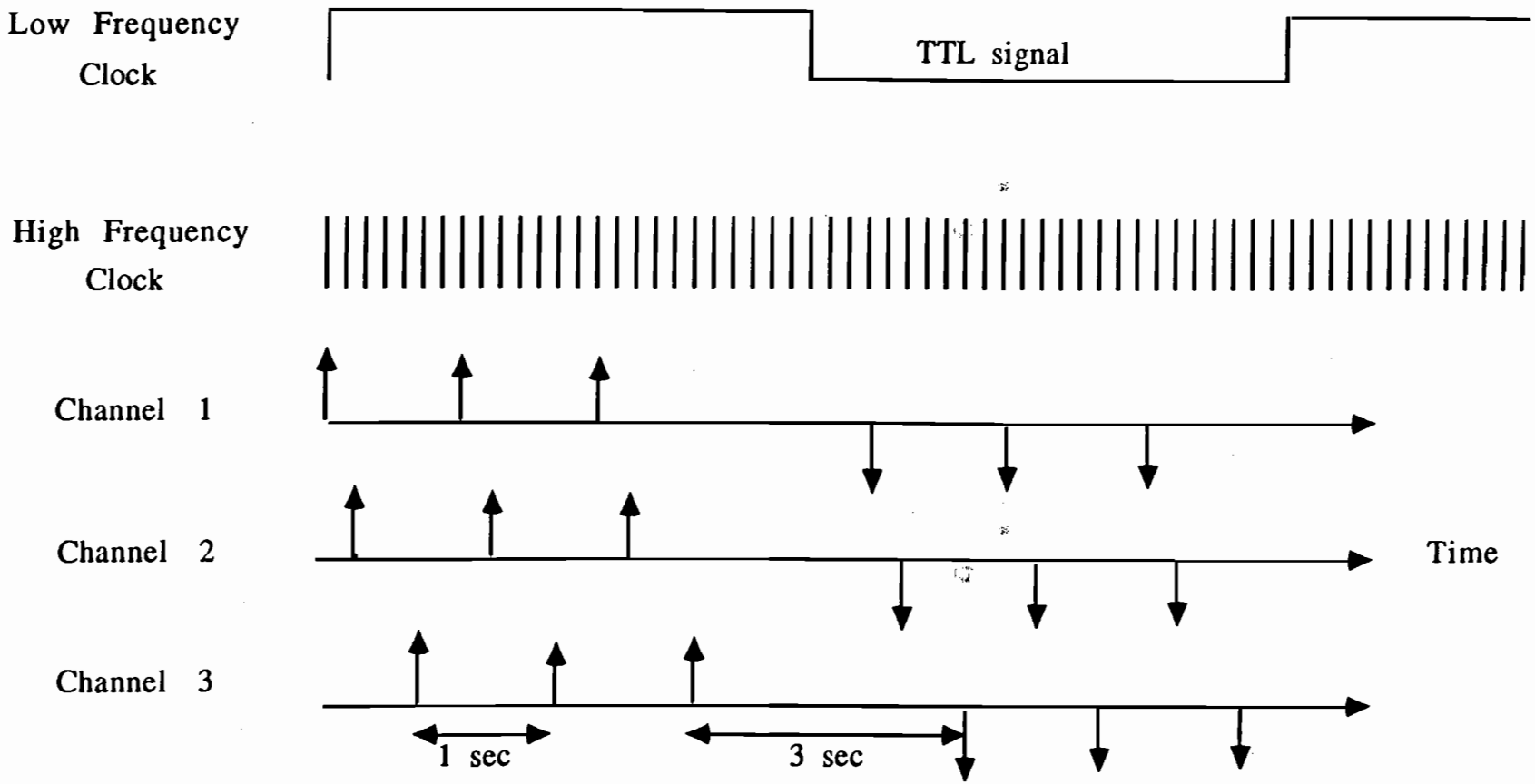

Figure 2.5. Timing and sampling sequence of the resistivity monitoring system for the pole-pole acquisition configuration.

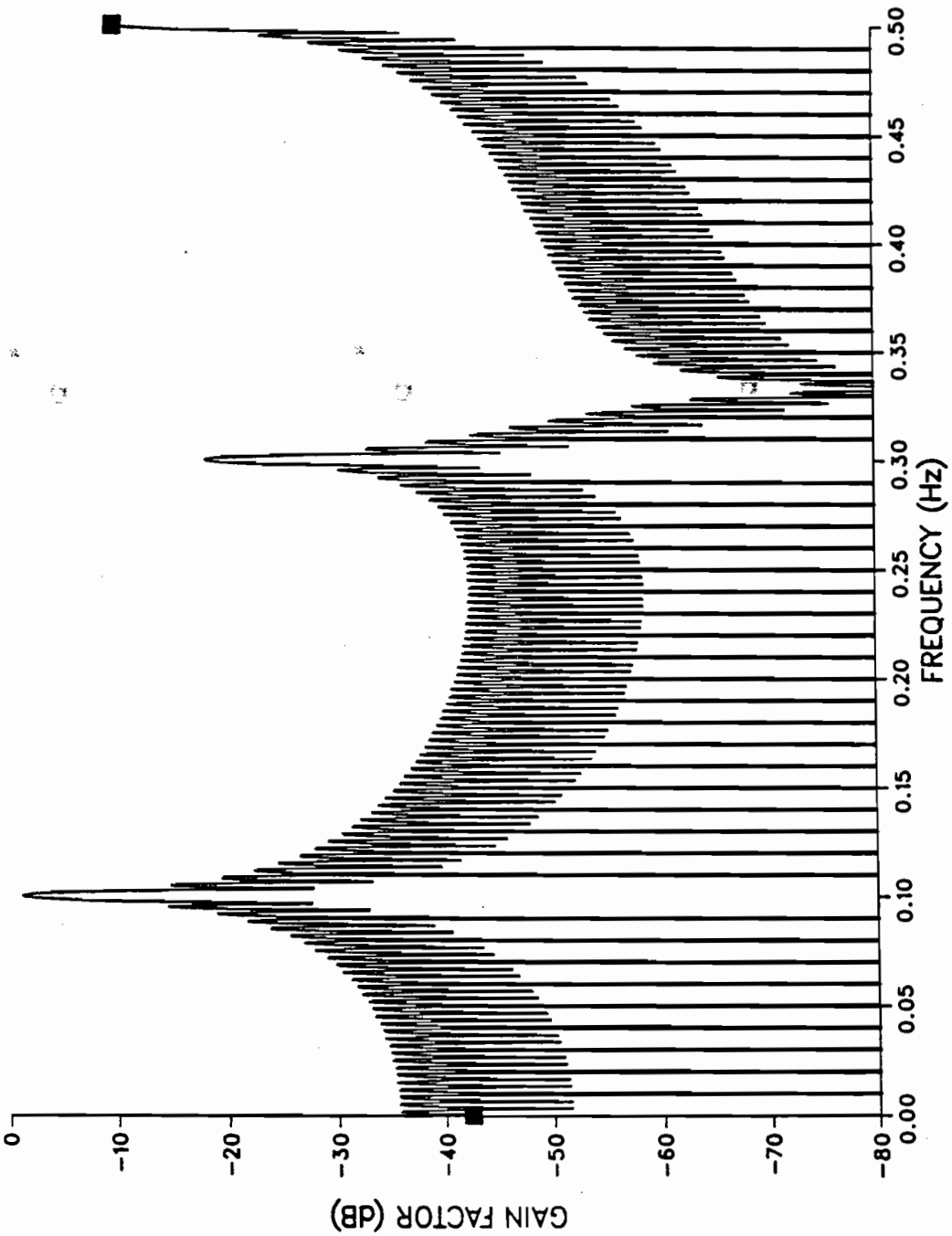

Figure 2.6. Frequency domain transfer function for the pole-pole configuration .

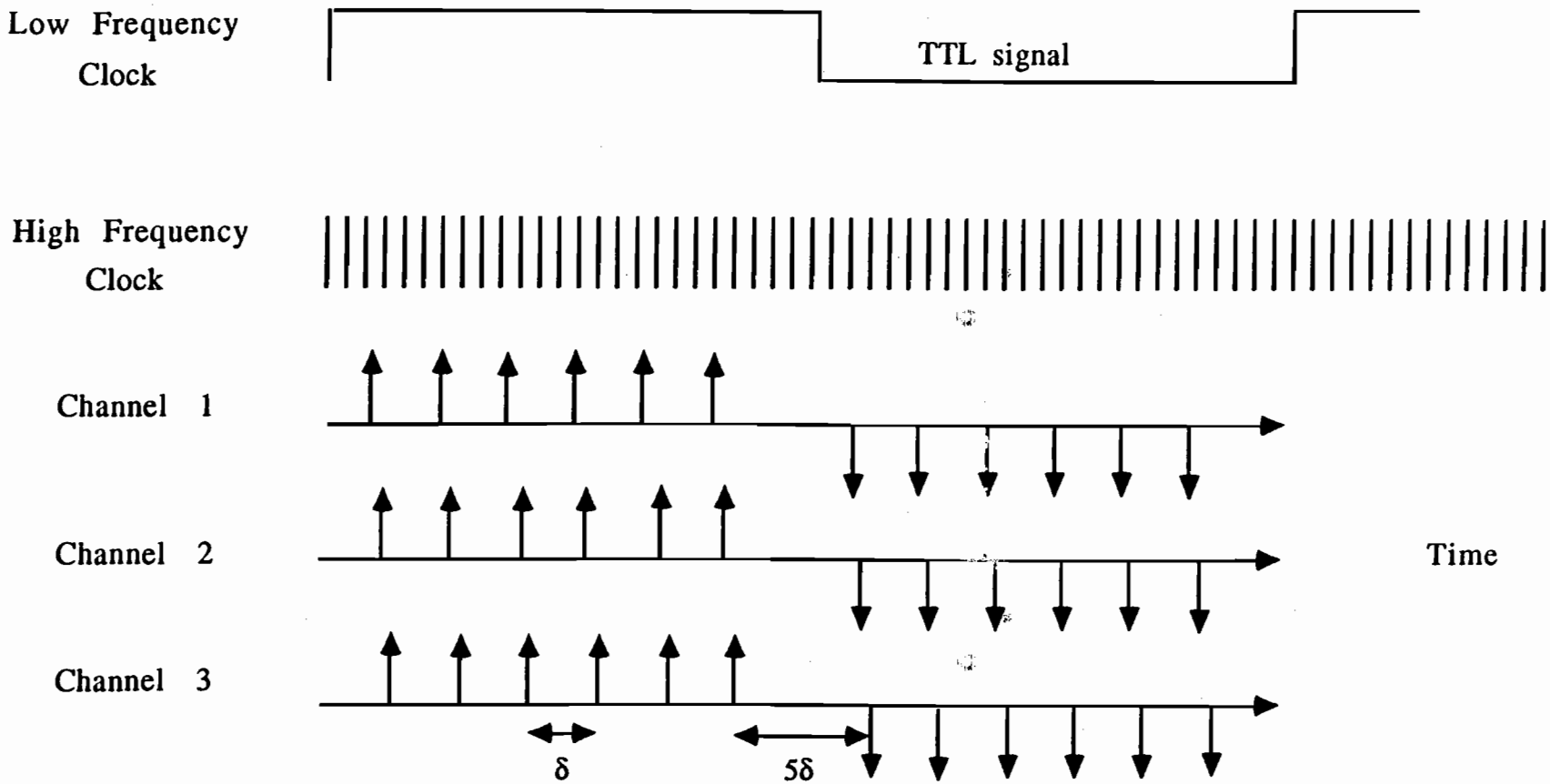

Figure 2.7. Timing and sampling sequence of the resistivity monitoring system for the pole-dipole acquisition configuration.

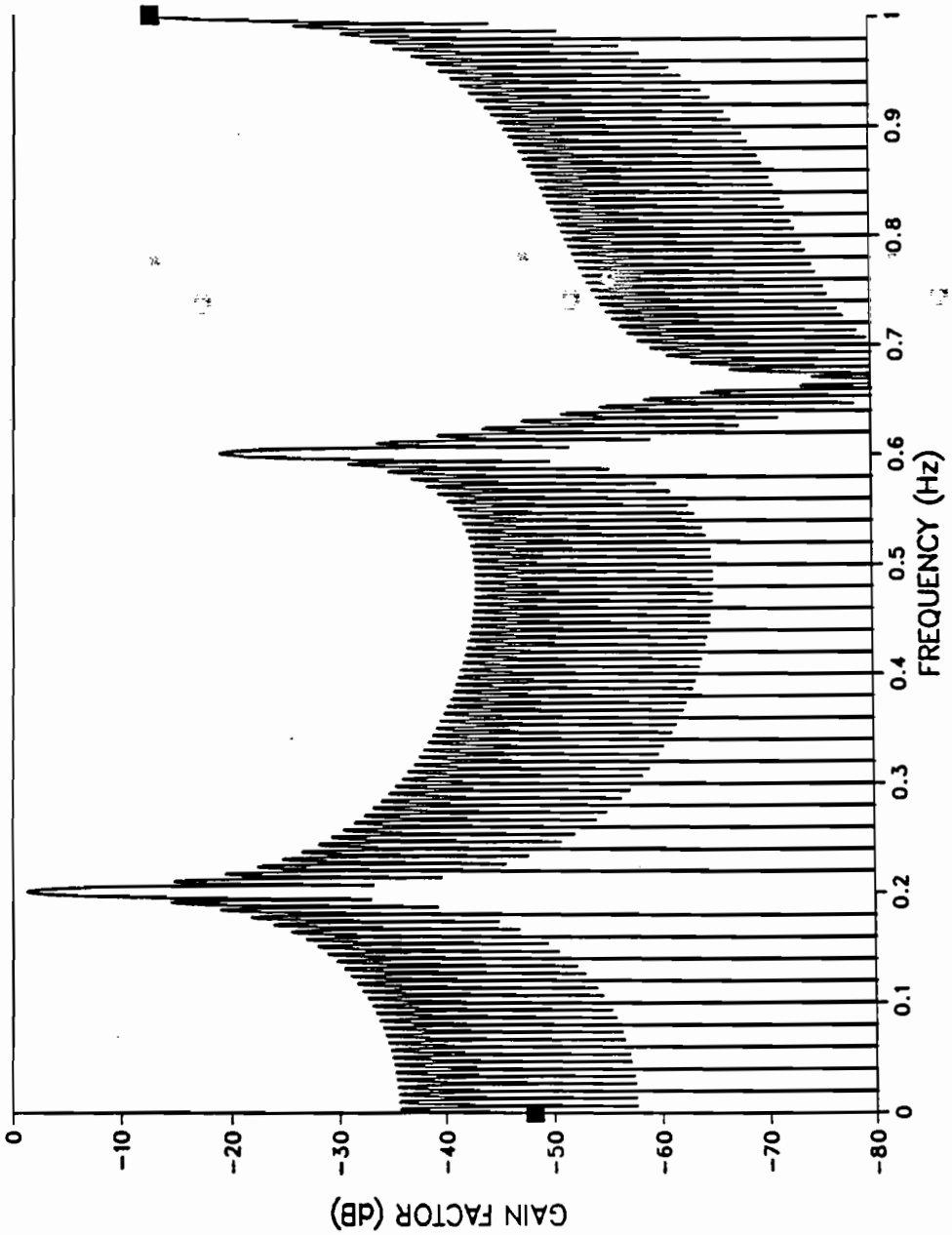

Figure 2.8. Frequency domain transfer function for the pole-dipole configuration .

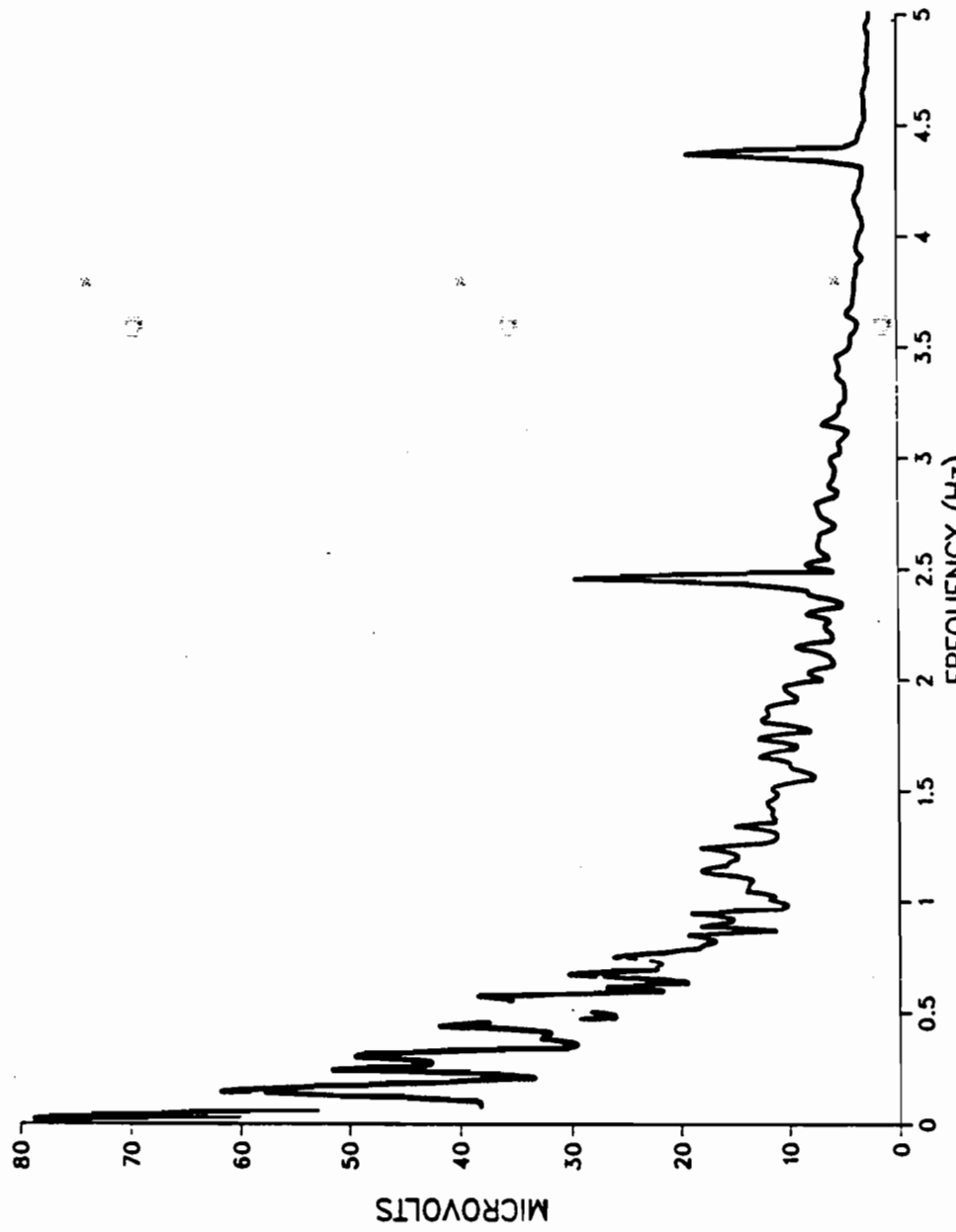

Figure 2.9. Telluric noise spectrum at the Richmond field station.

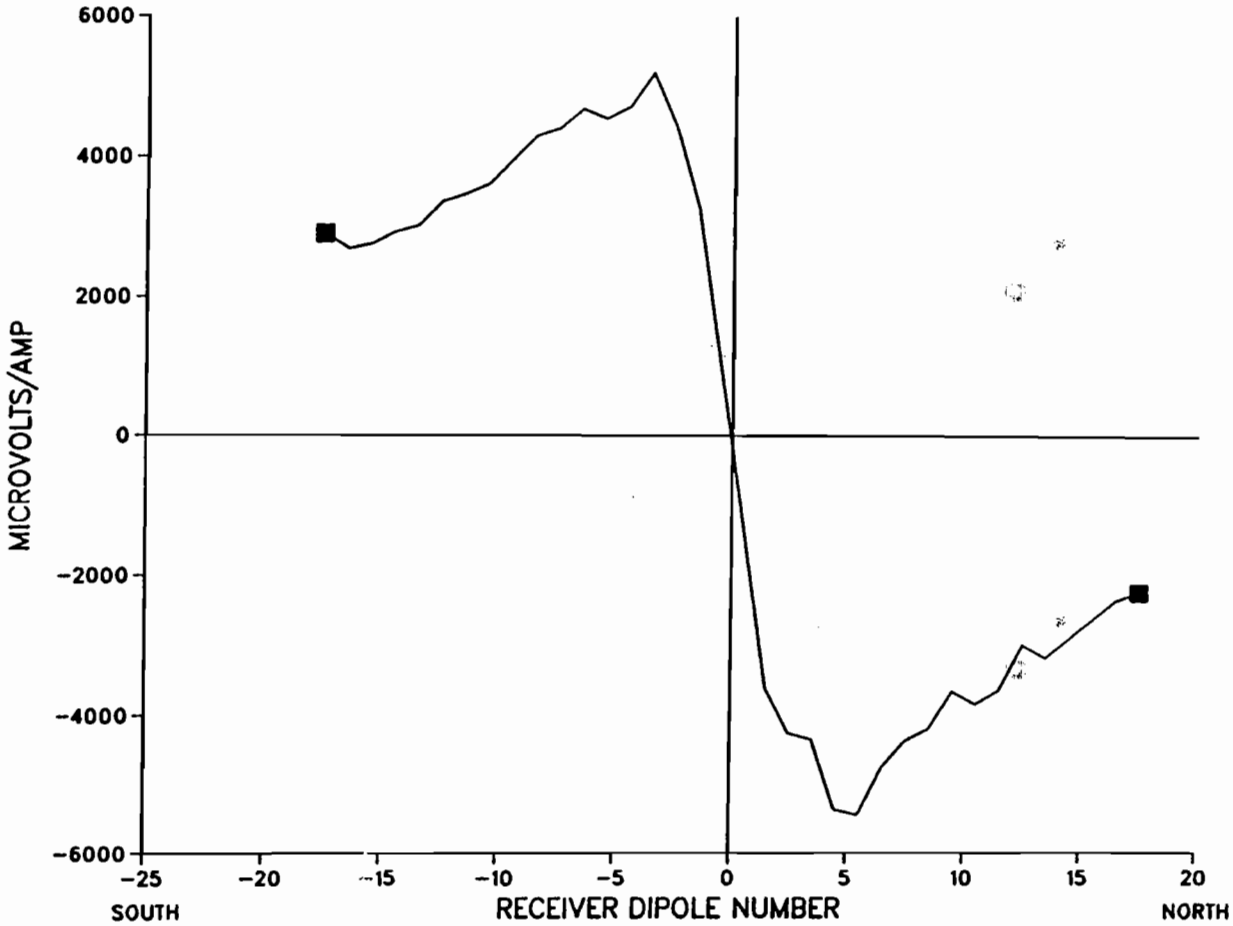

Figure 2.10. Baseline pole-dipole normalized voltage for a current electrode at 30 m depth in well INJ and 5 m receiver dipoles along the south-north line.

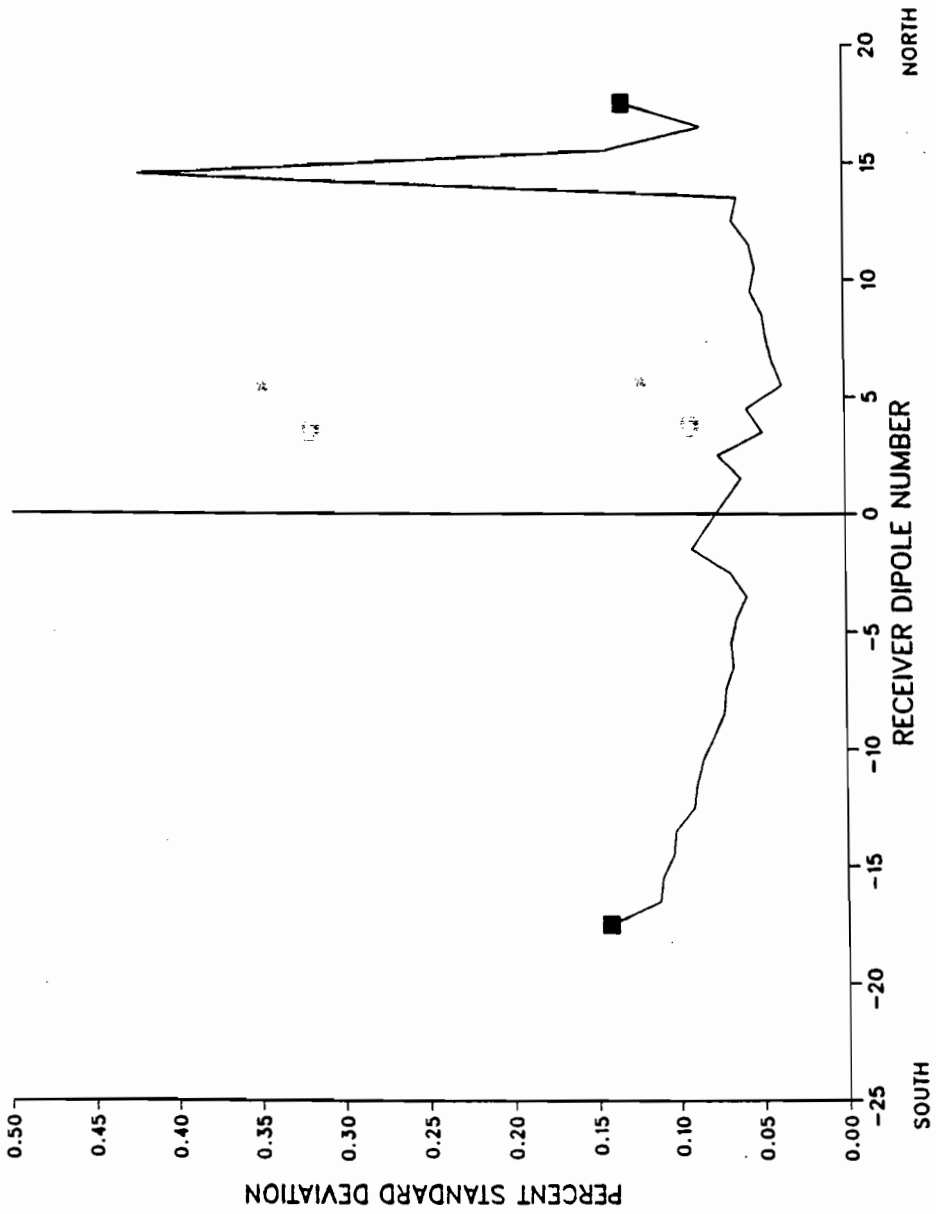

Figure 2.11. Percent standard deviation of pole-dipole data.

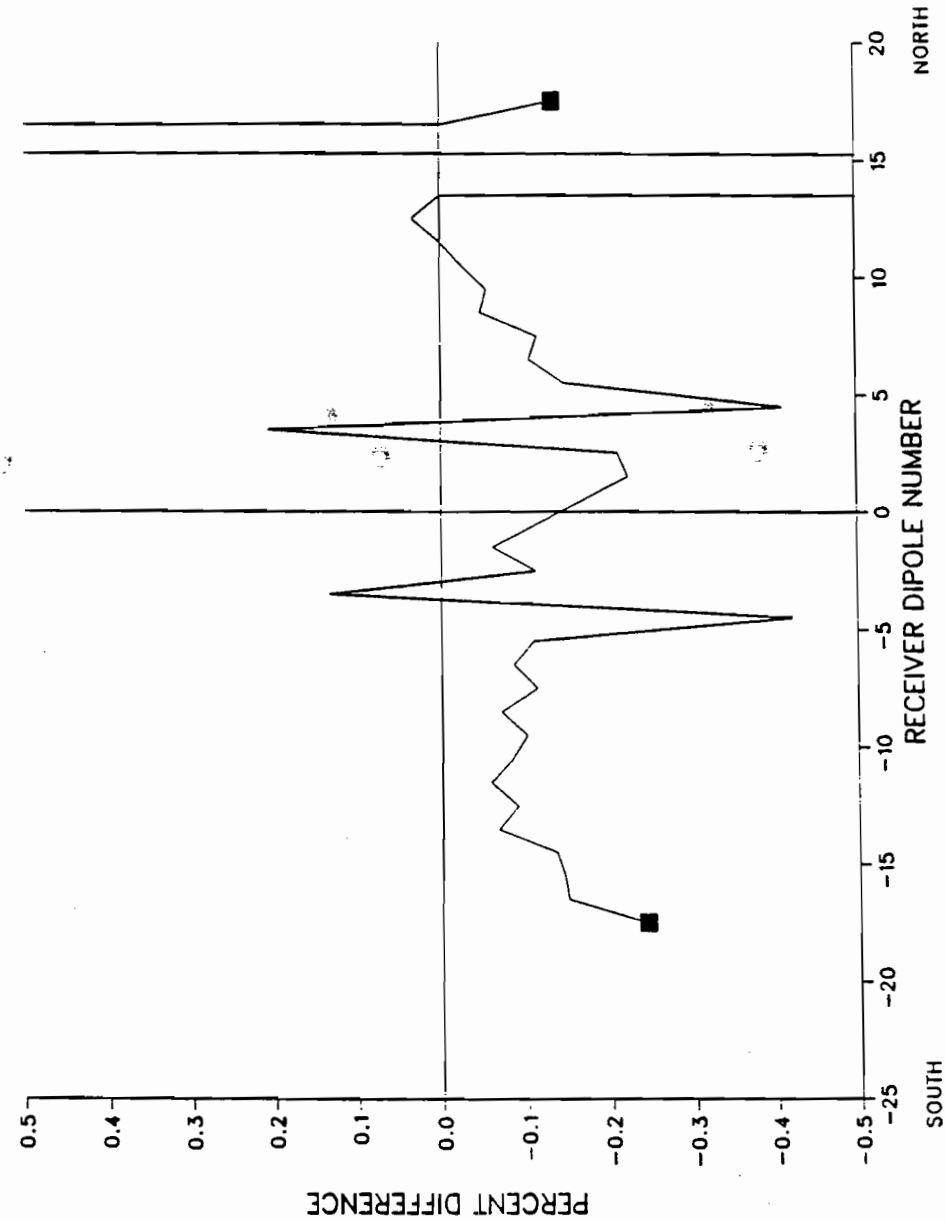

Figure 2.12. Percent difference of pole-dipole data taken on two consecutive days.

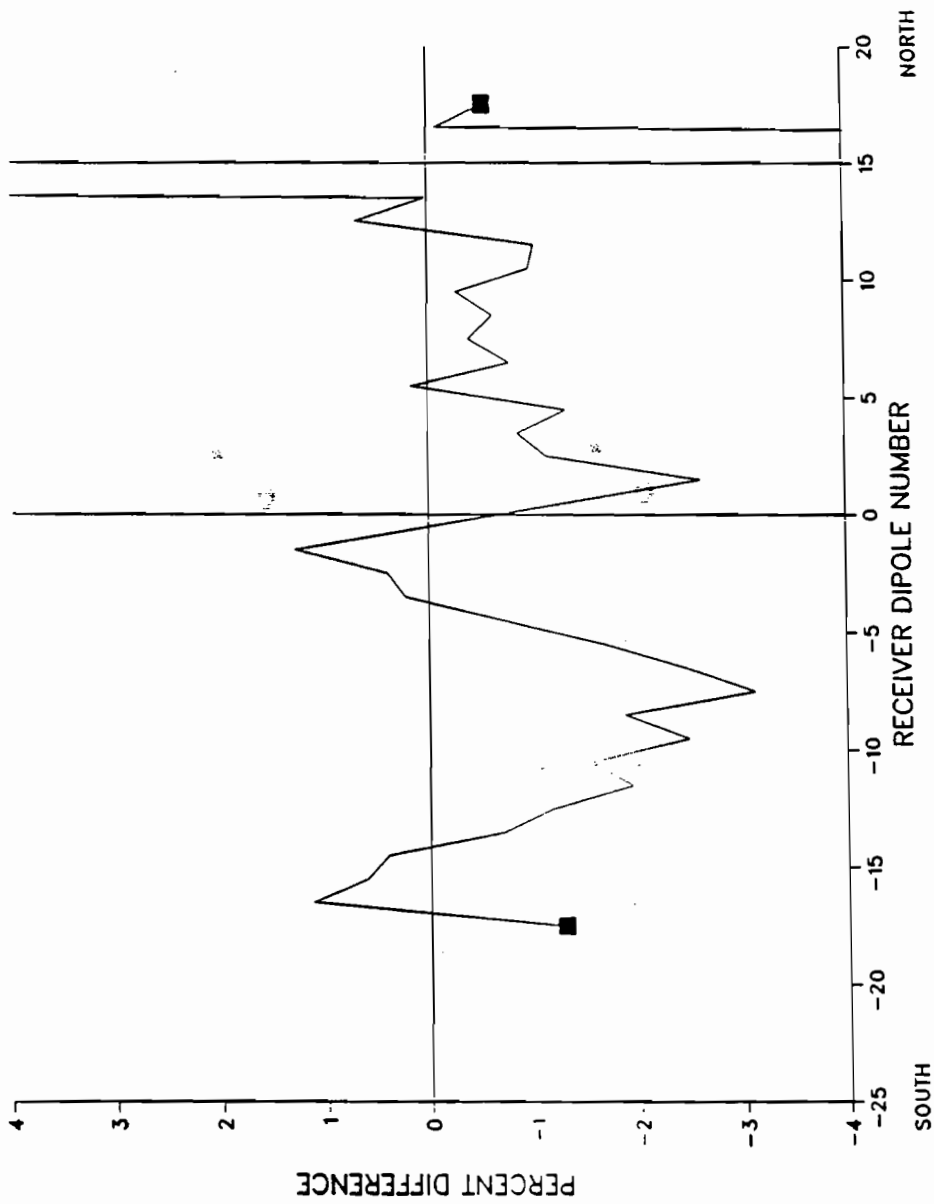

Figure 2.13. Percent difference of pole-dipole data taken before and after half an inch of rain.

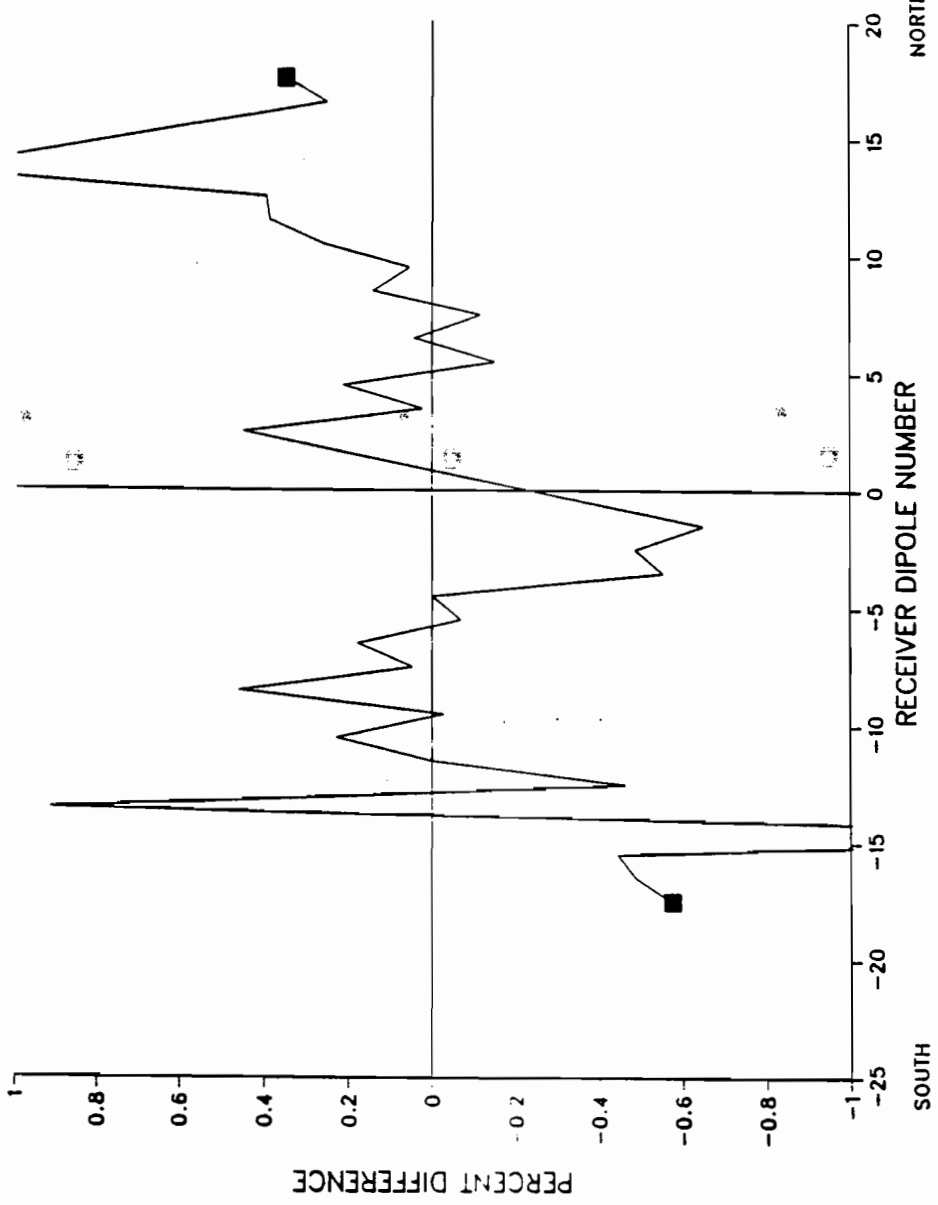

Figure 2.14. Percent difference of pole-dipole data taken on two consecutive days with maximum salt water injected and light rain fall overnight.

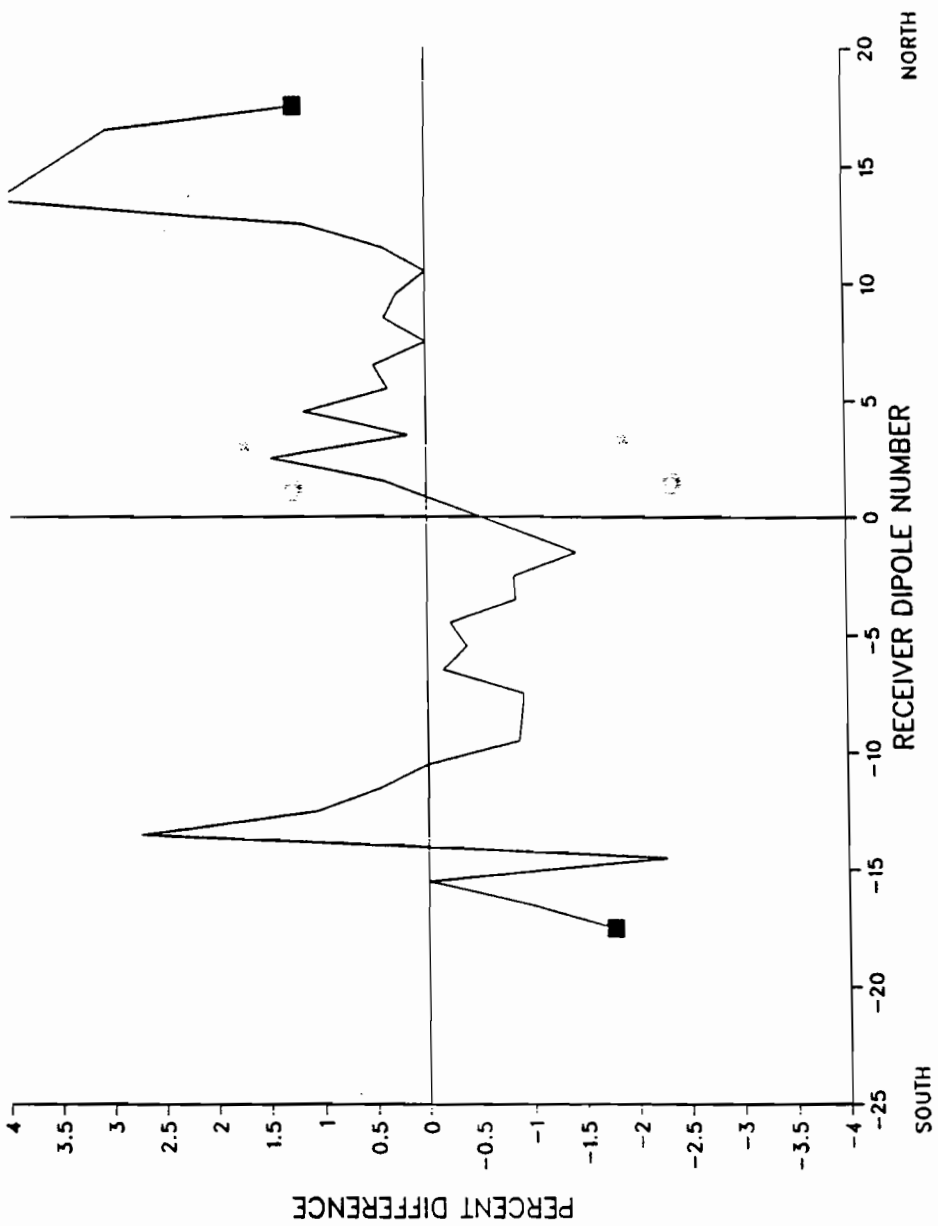

Figure 2.15. Percent difference of superposed dipole-dipole data taken on the same days as the data in Figure 2.14.

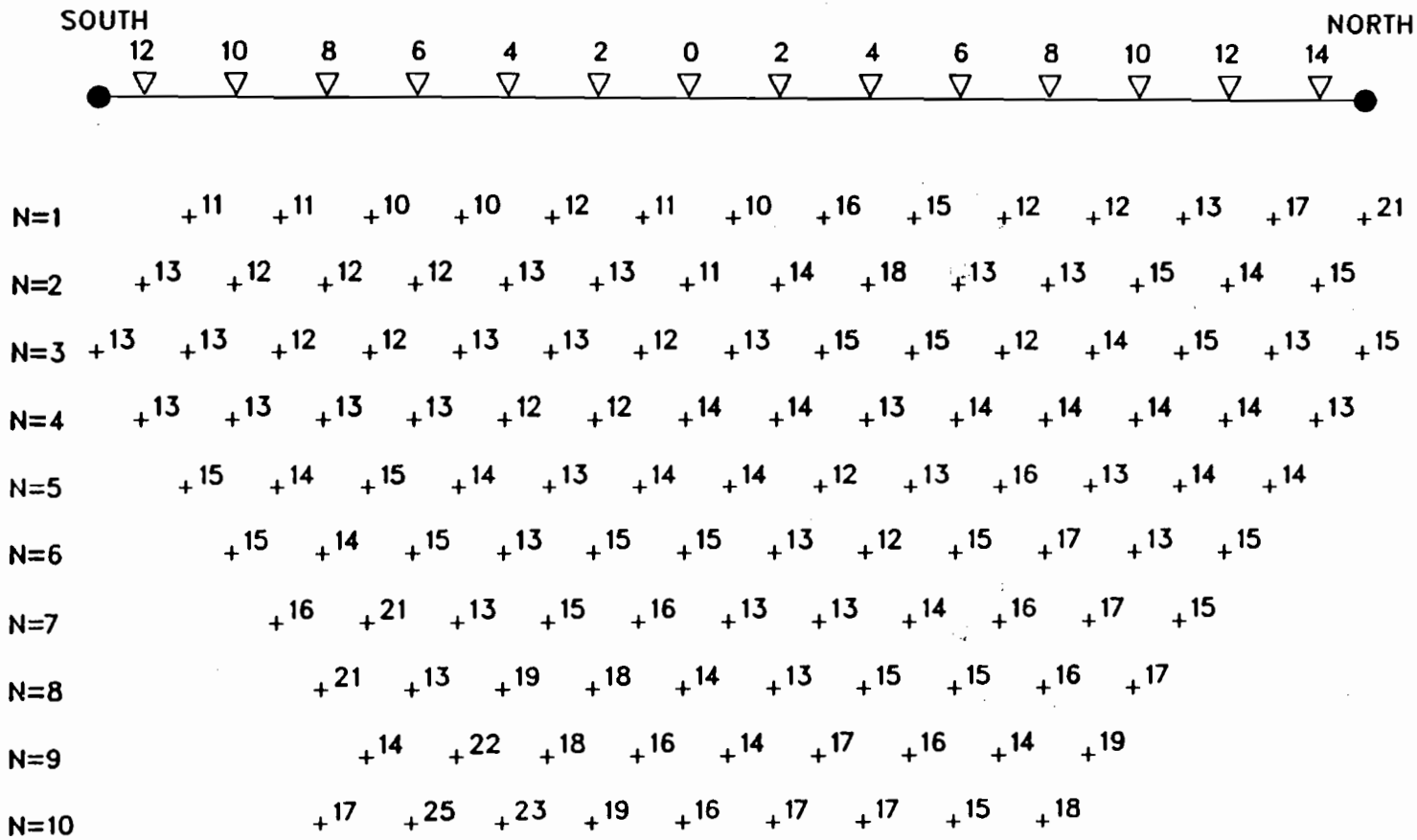

Figure 3.1. Surface dipole-dipole pseudosection before salt water injection. Apparent resistivities in ohm-m.

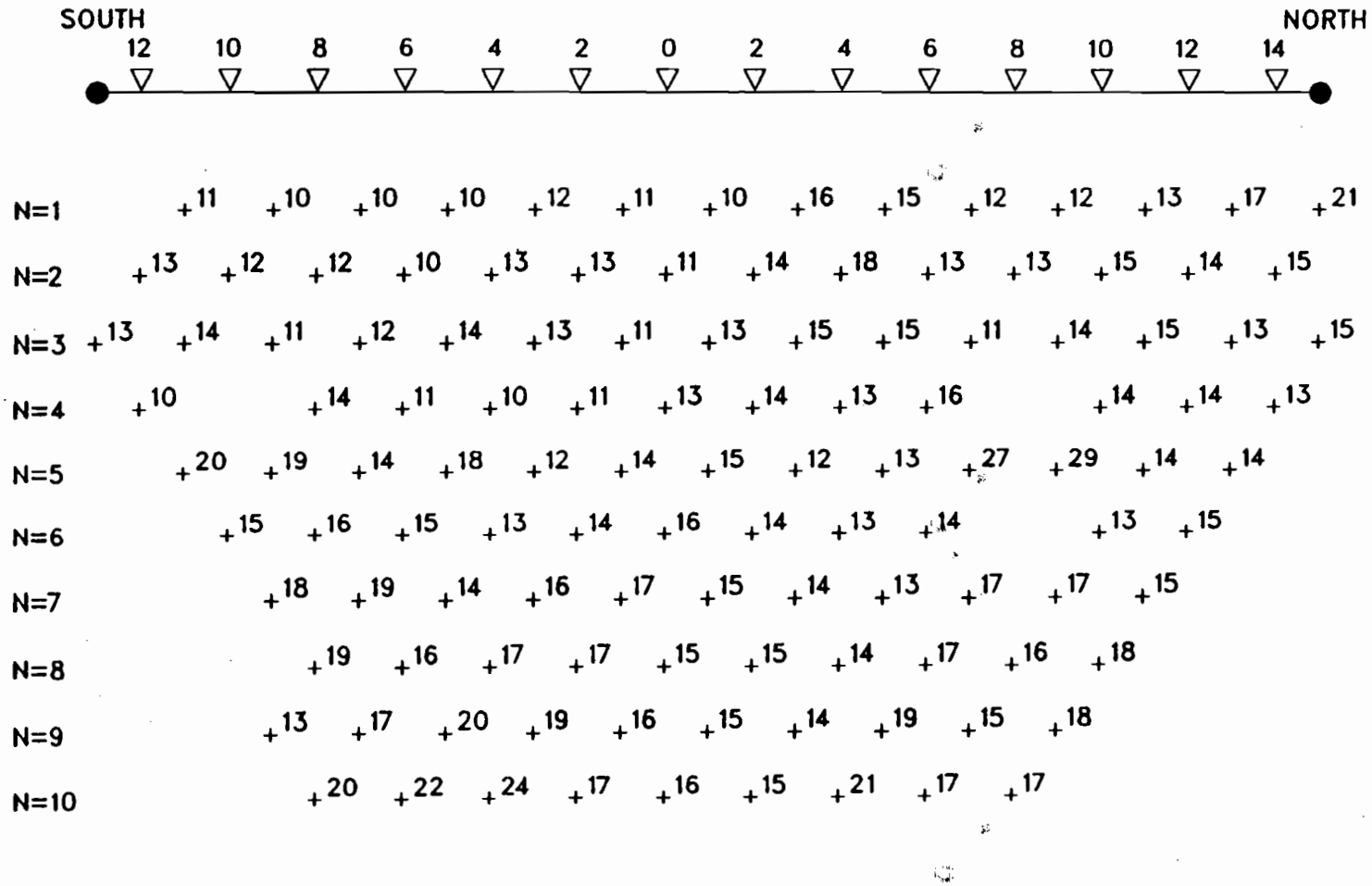

Figure 3.2. Surface dipole-dipole pseudosection at maximum salt water injection. Apparent resistivities in ohm-m.

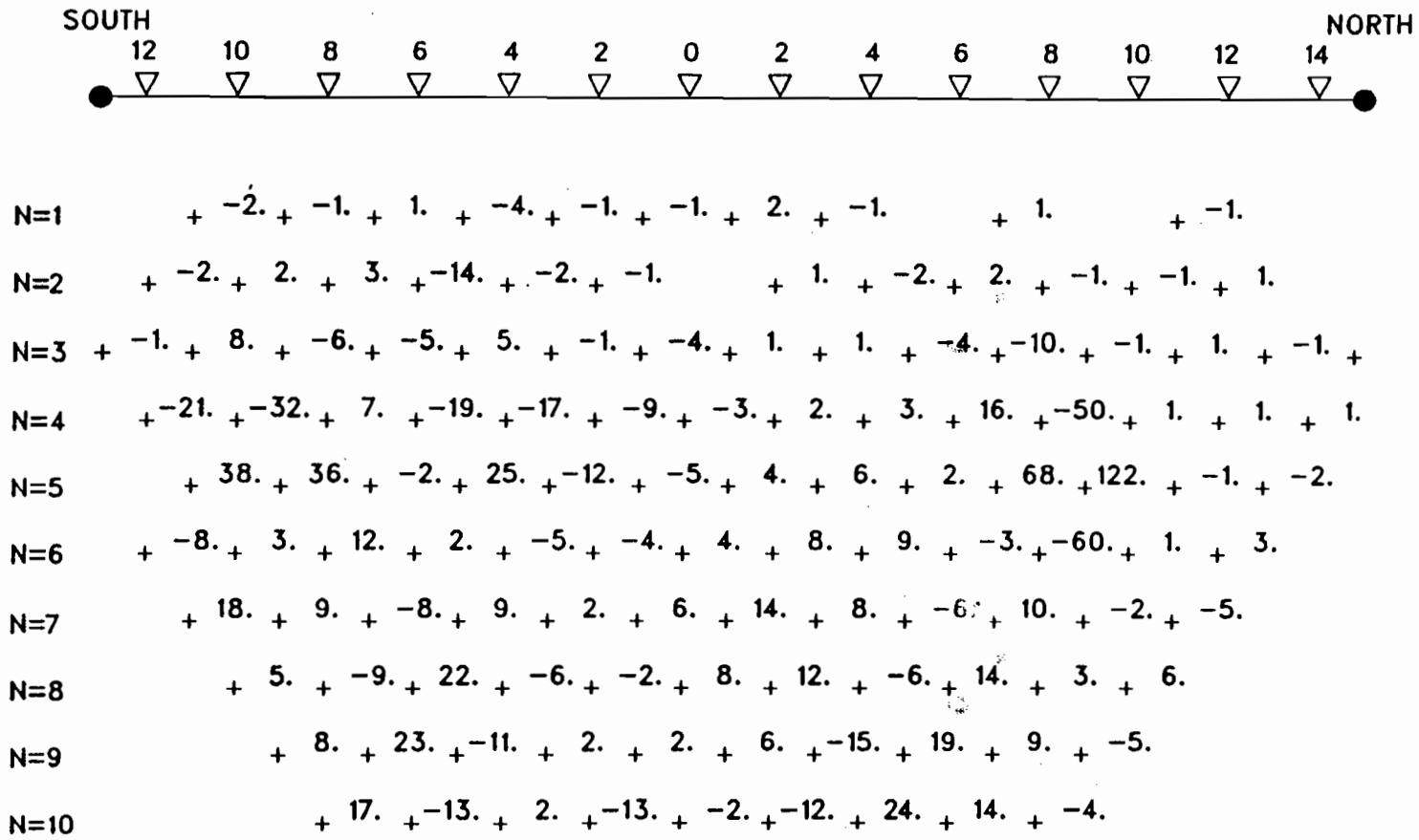

Figure 3.3. Percent difference surface dipole-dipole pseudosection.

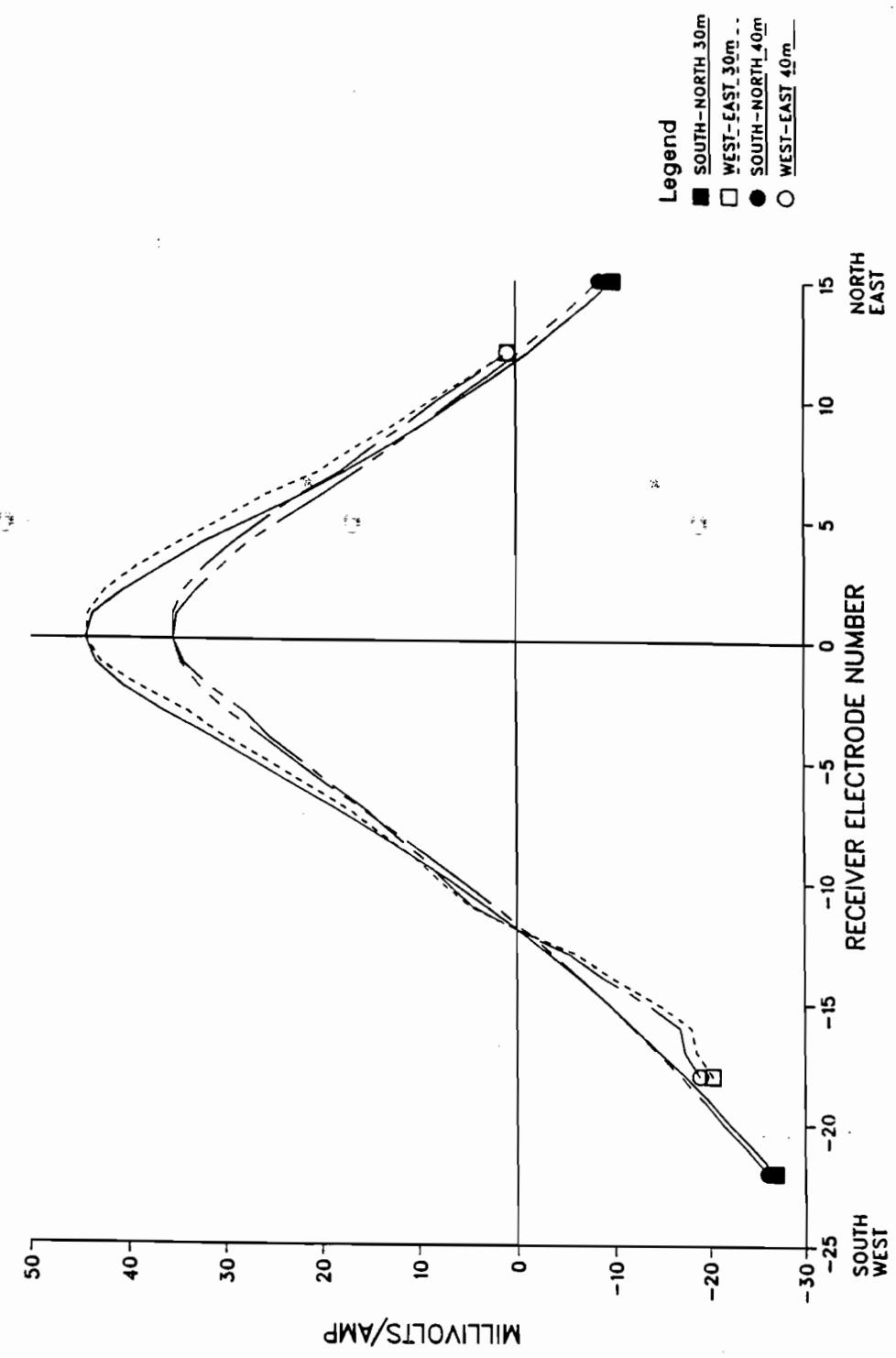

Figure 3.4. Borehole to surface pole-pole potential before salt water injection.

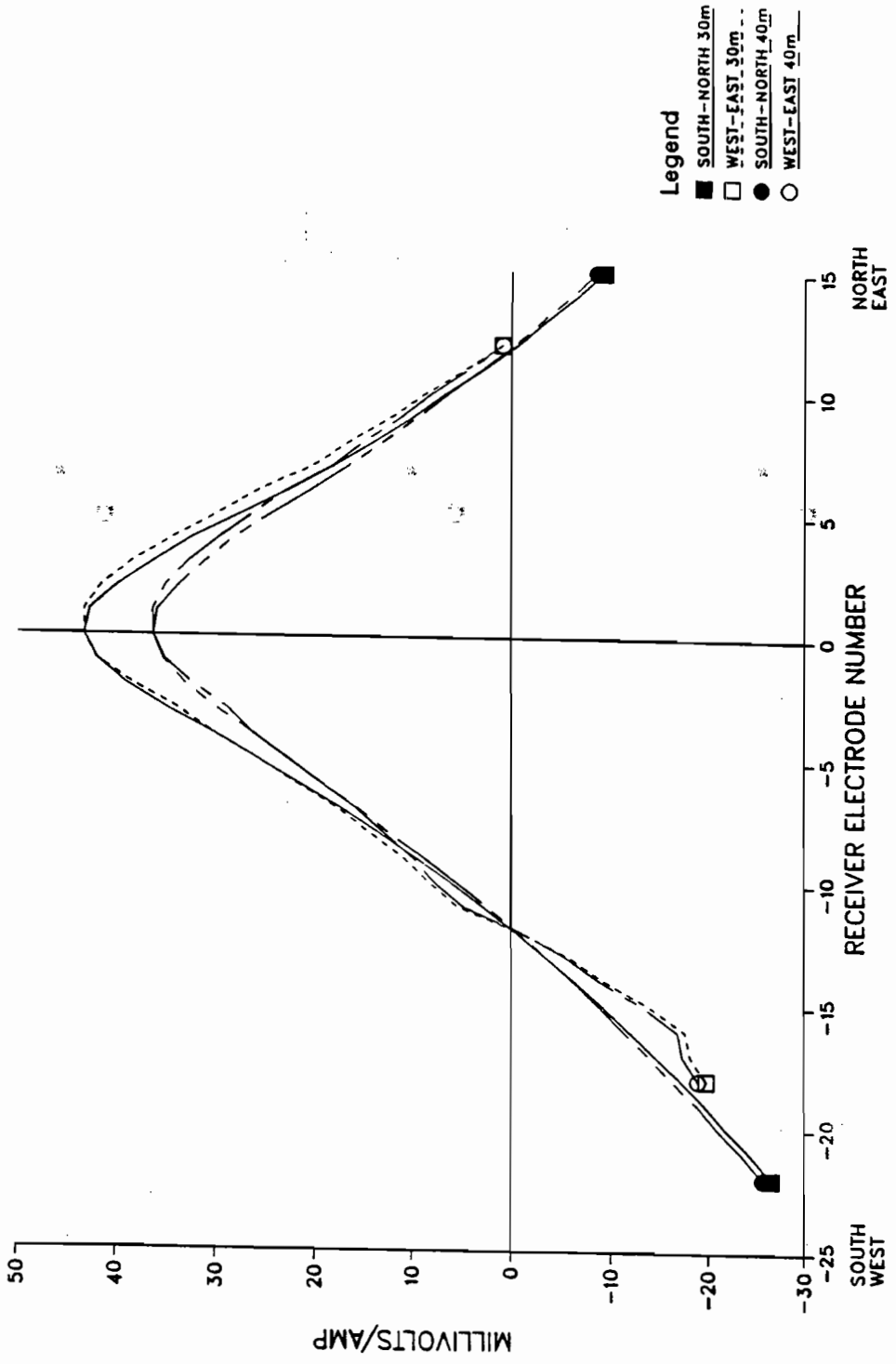

Figure 3.5. Borehole to surface pole-pole potential at maximum salt water injection.

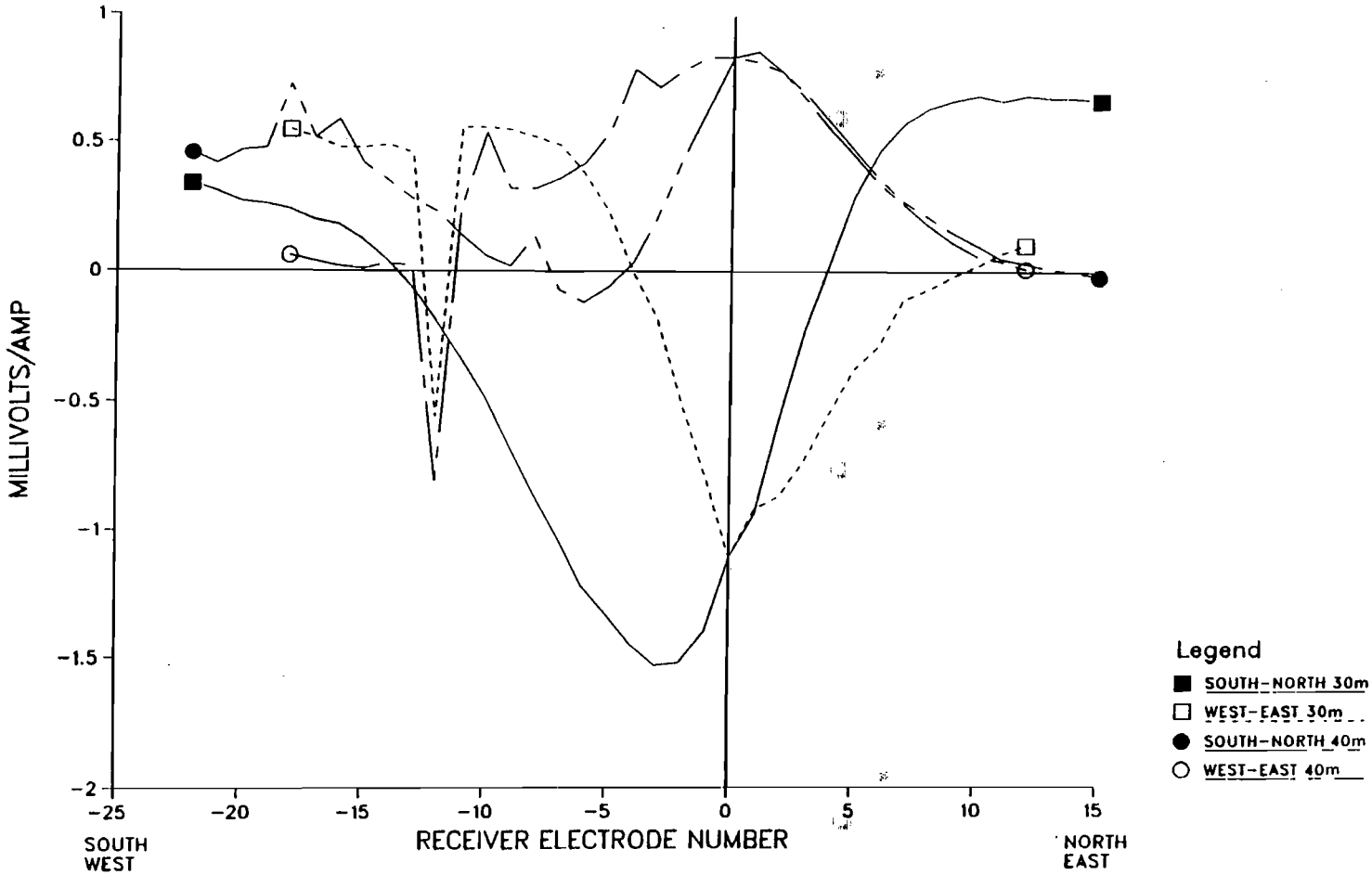

Figure 3.6. Time difference of borehole to surface pole-pole potential. This is the result of subtracting the data in Figure 3.4 from the data in Figure 3.5.

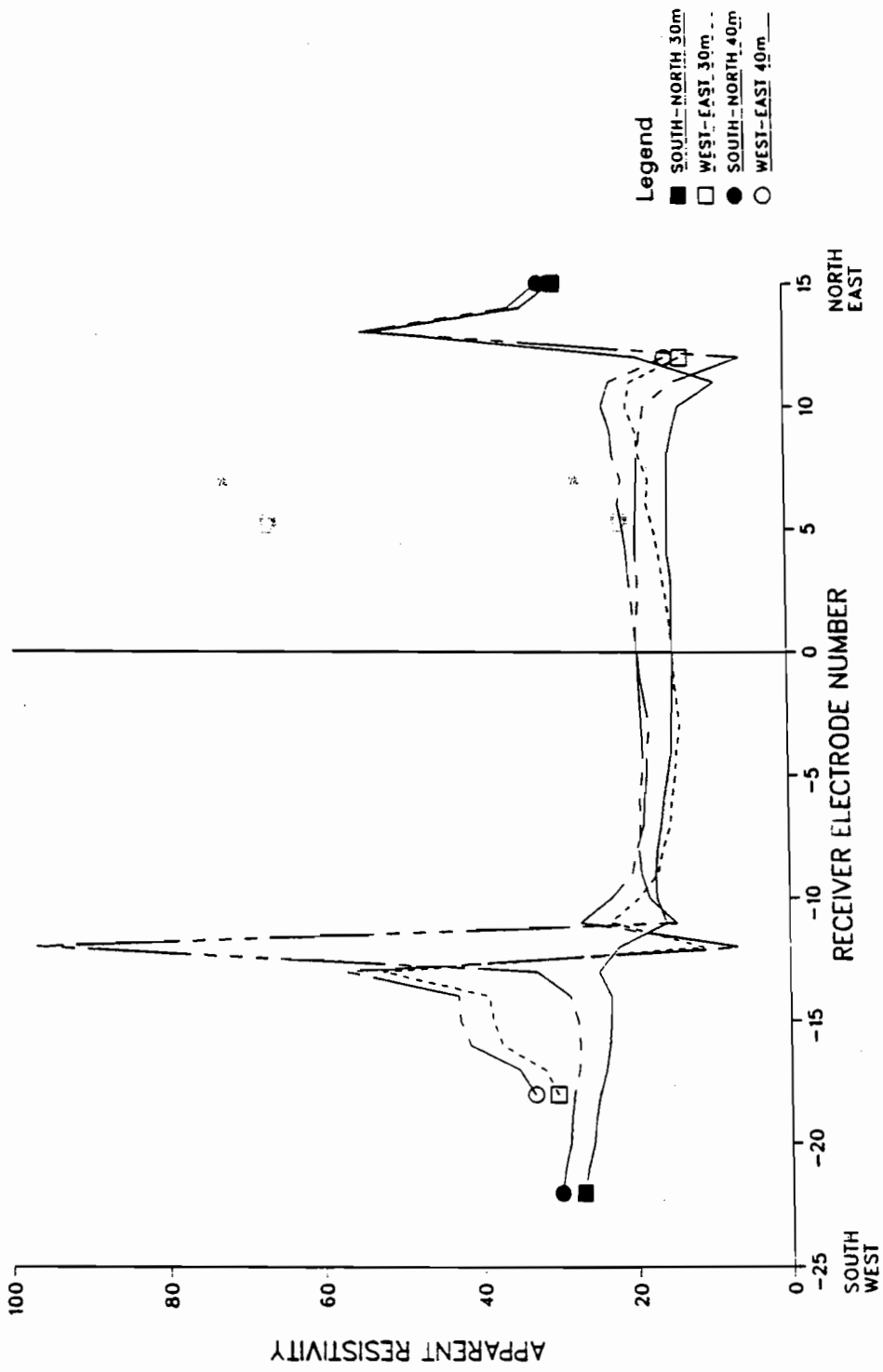

Figure 3.7. Pole-pole apparent resistivity before salt water injection.

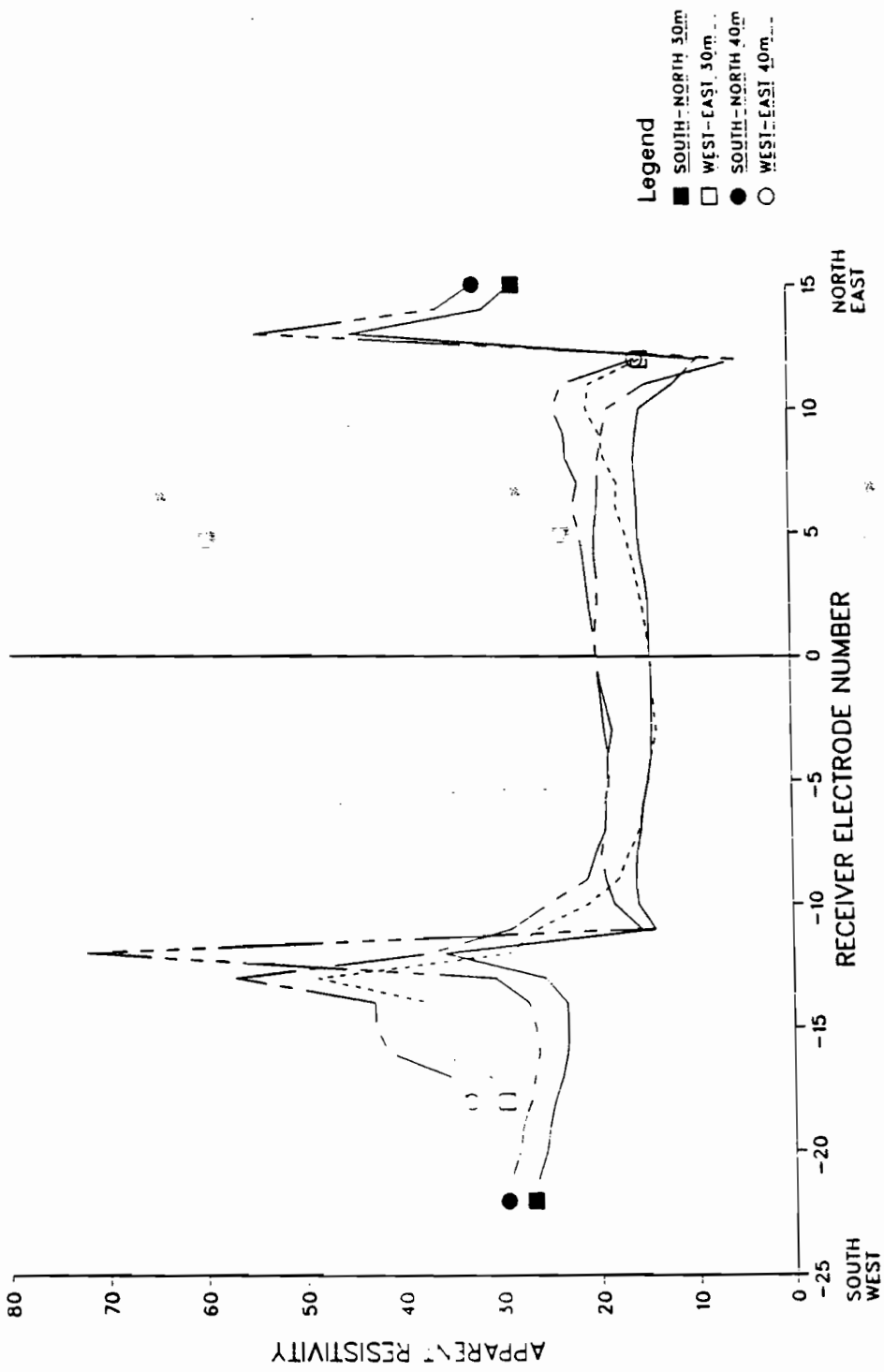

Figure 3.8. Pole-pole apparent resistivity at maximum salt water injection.

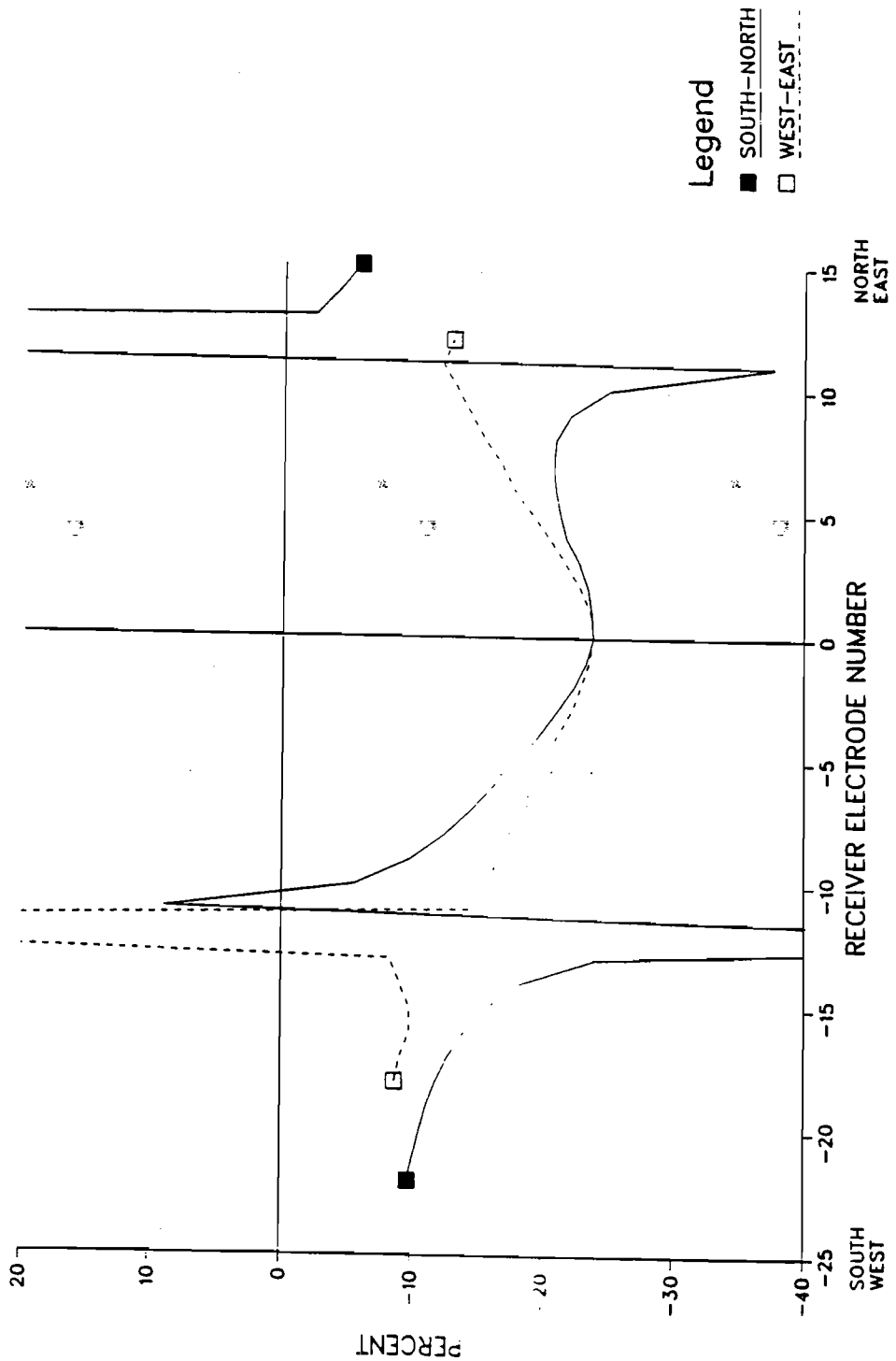

Figure 3.9. Spatial percent difference of the baseline pole-pole apparent resistivities.

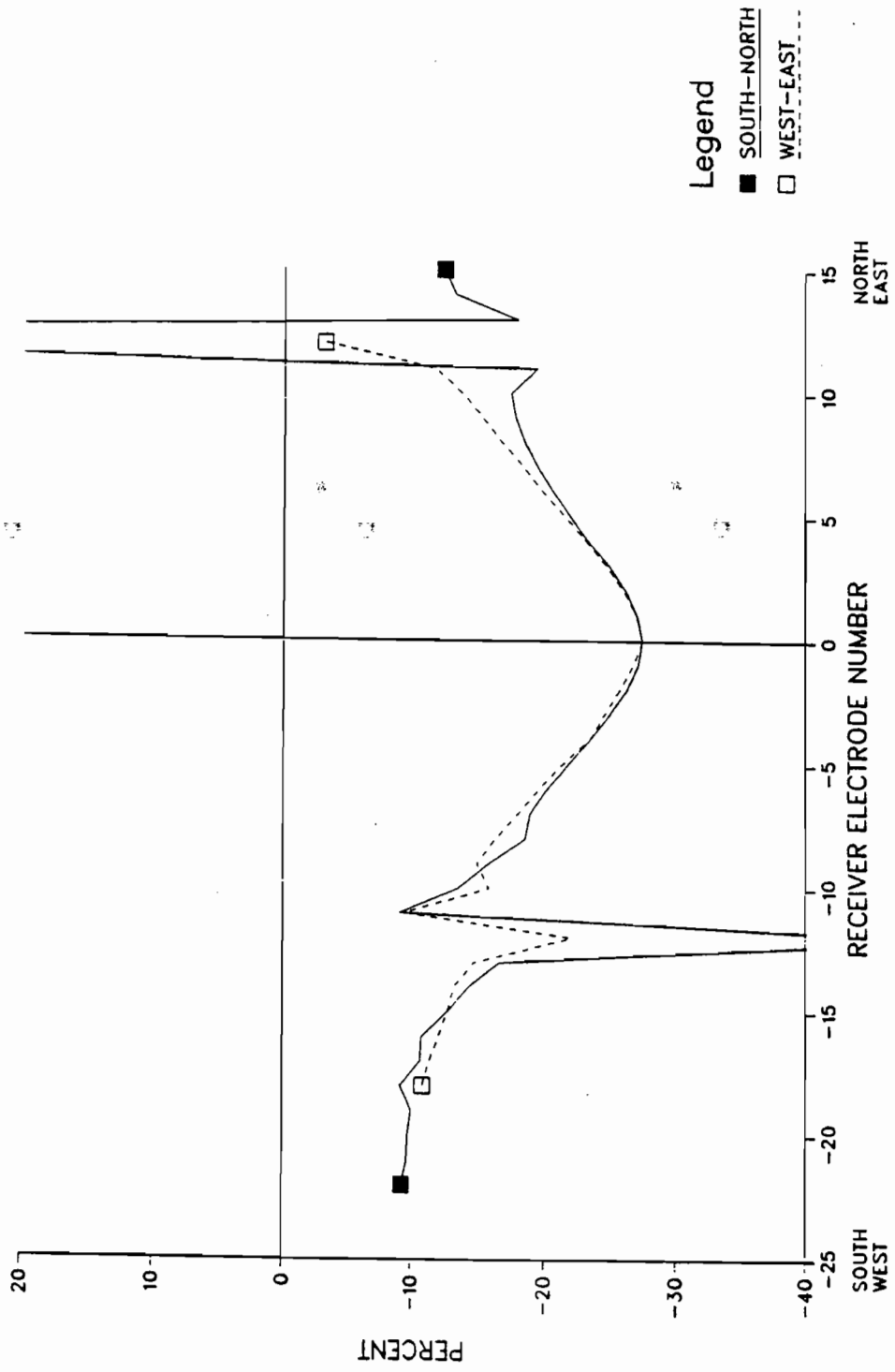

Figure 3.10. Spatial percent difference of the maximum injection pole-pole apparent resistivities.

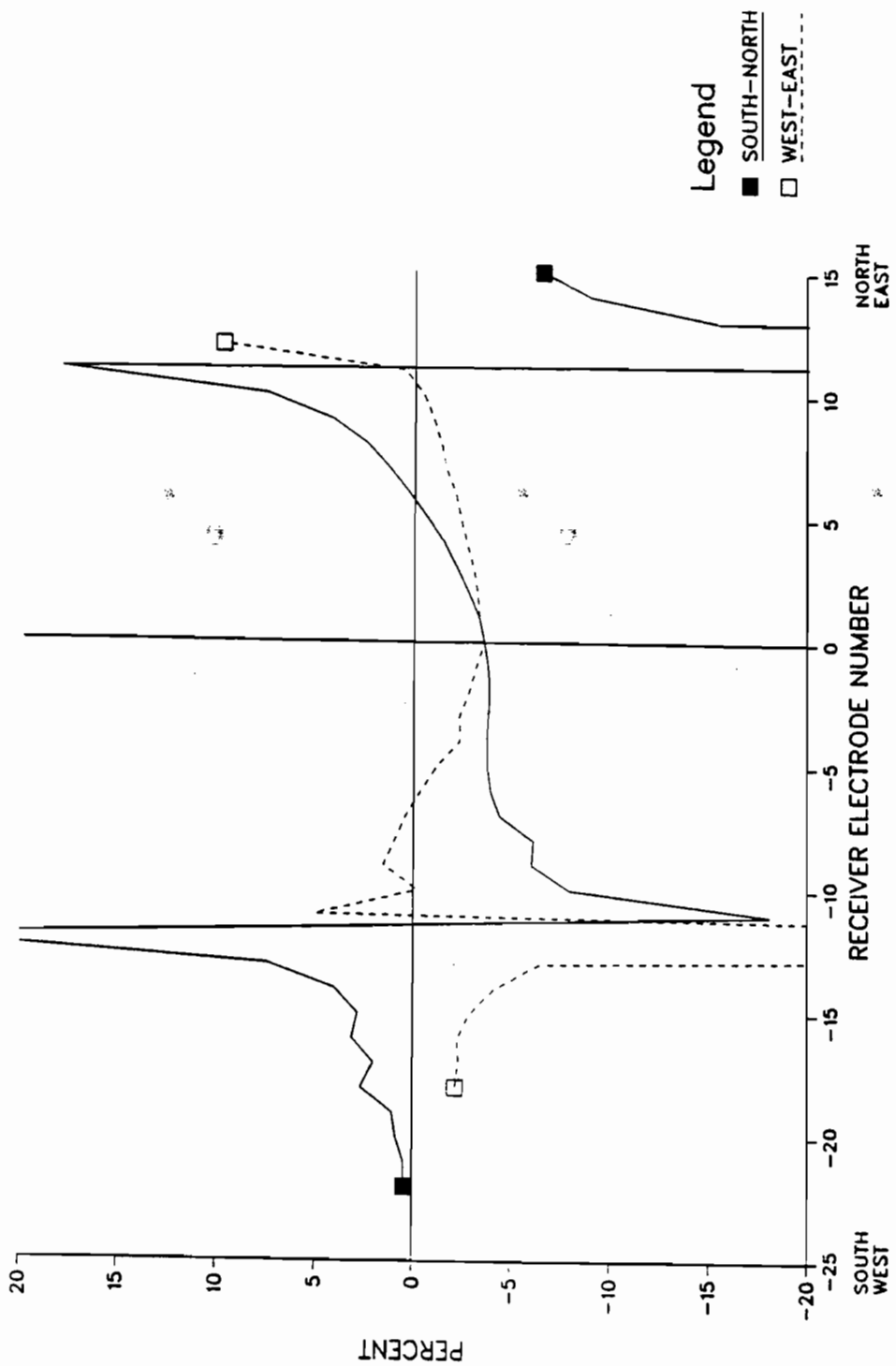

Figure 3.11. Temporal difference of the pole-pole apparent resistivities. This is the result of subtracting the data in Figure 3.9 from the data in Figure 3.10.

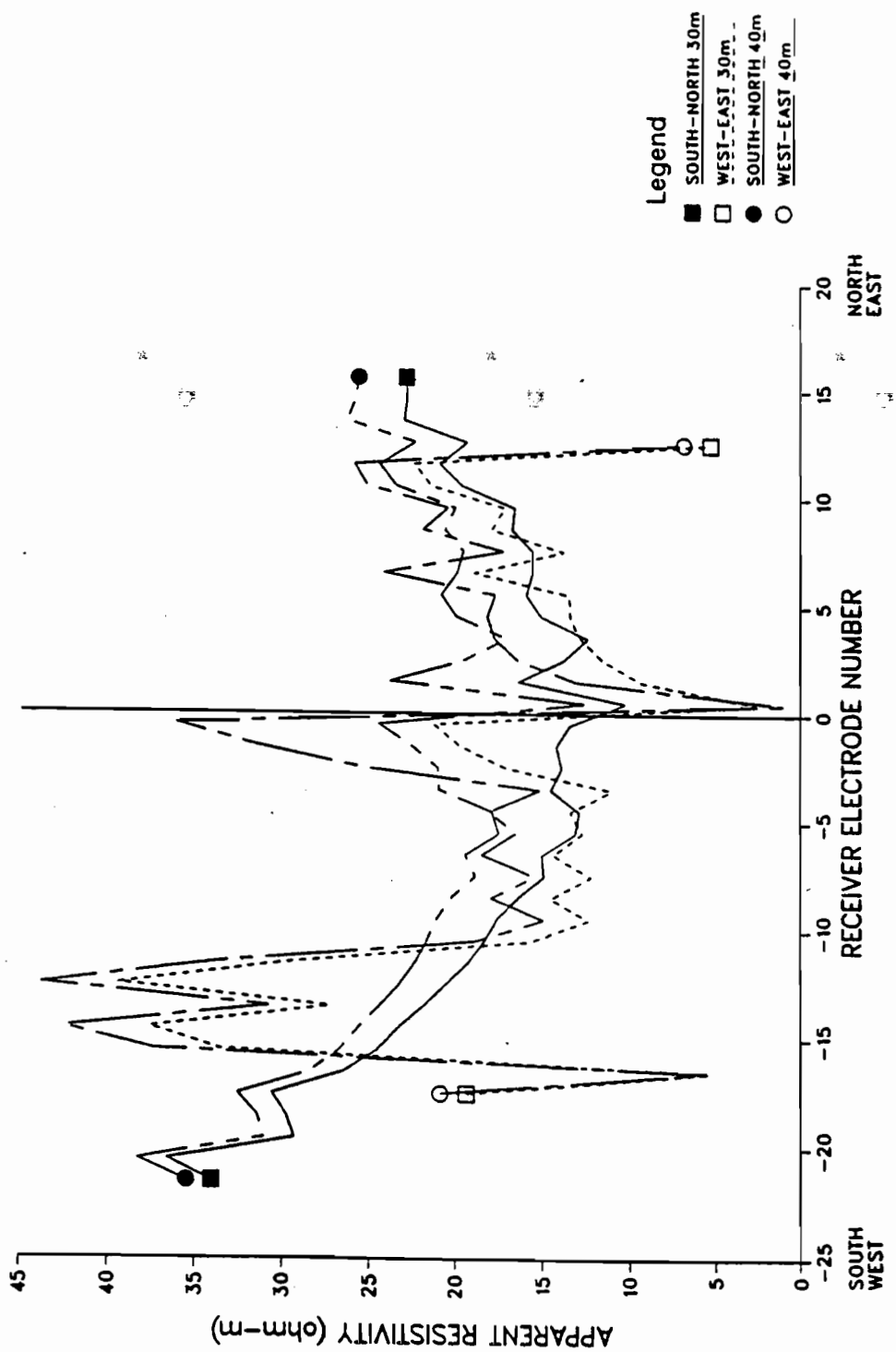

Figure 3.12. Baseline apparent resistivity calculated from the superposed pole-dipole potential. The pole-pole data was superposed to create pole-dipole voltages for apparent resistivity calculation.

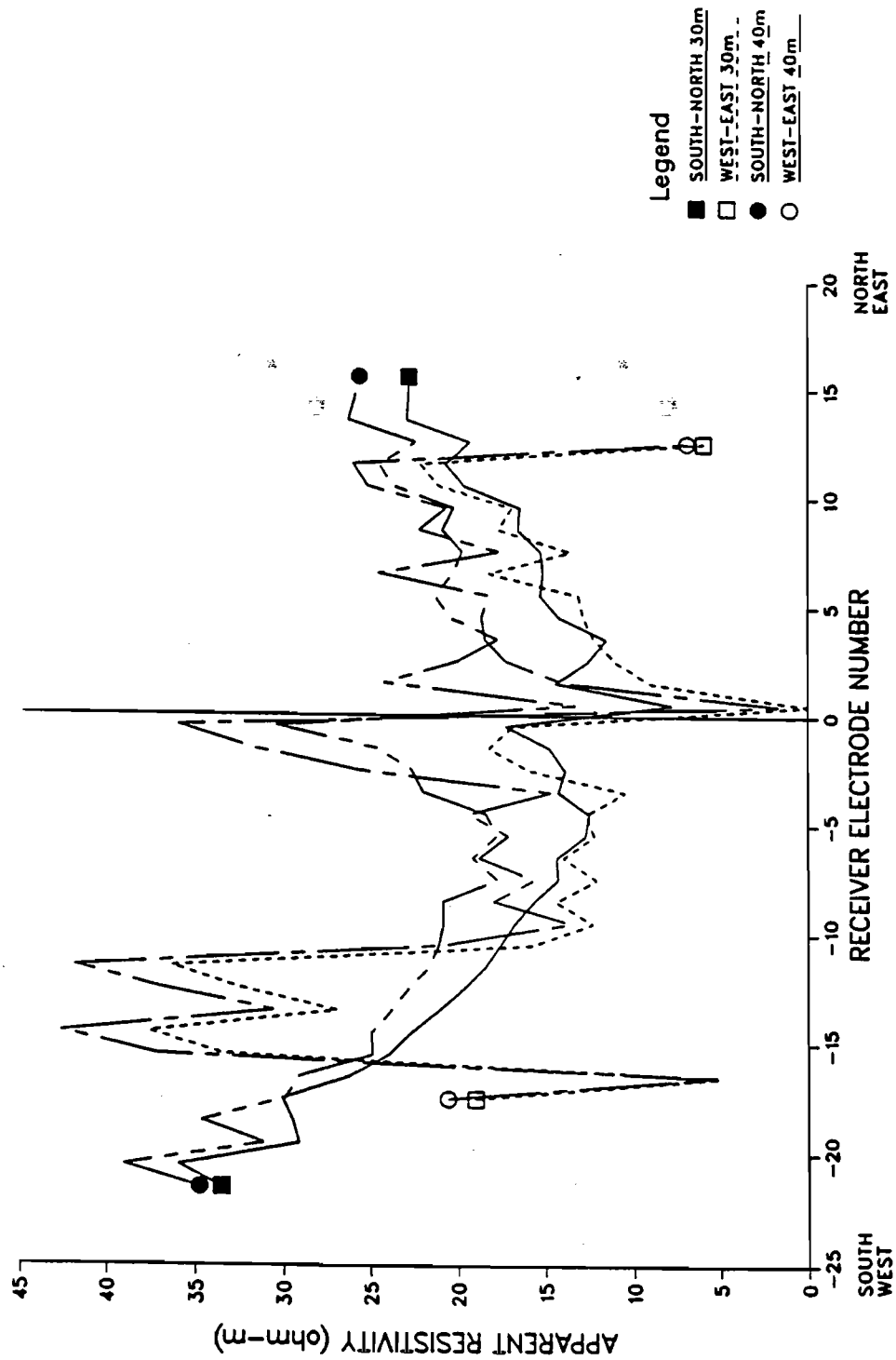

Figure 3.13. Apparent resistivity at maximum injection calculated from the superposed pole-dipole potential.

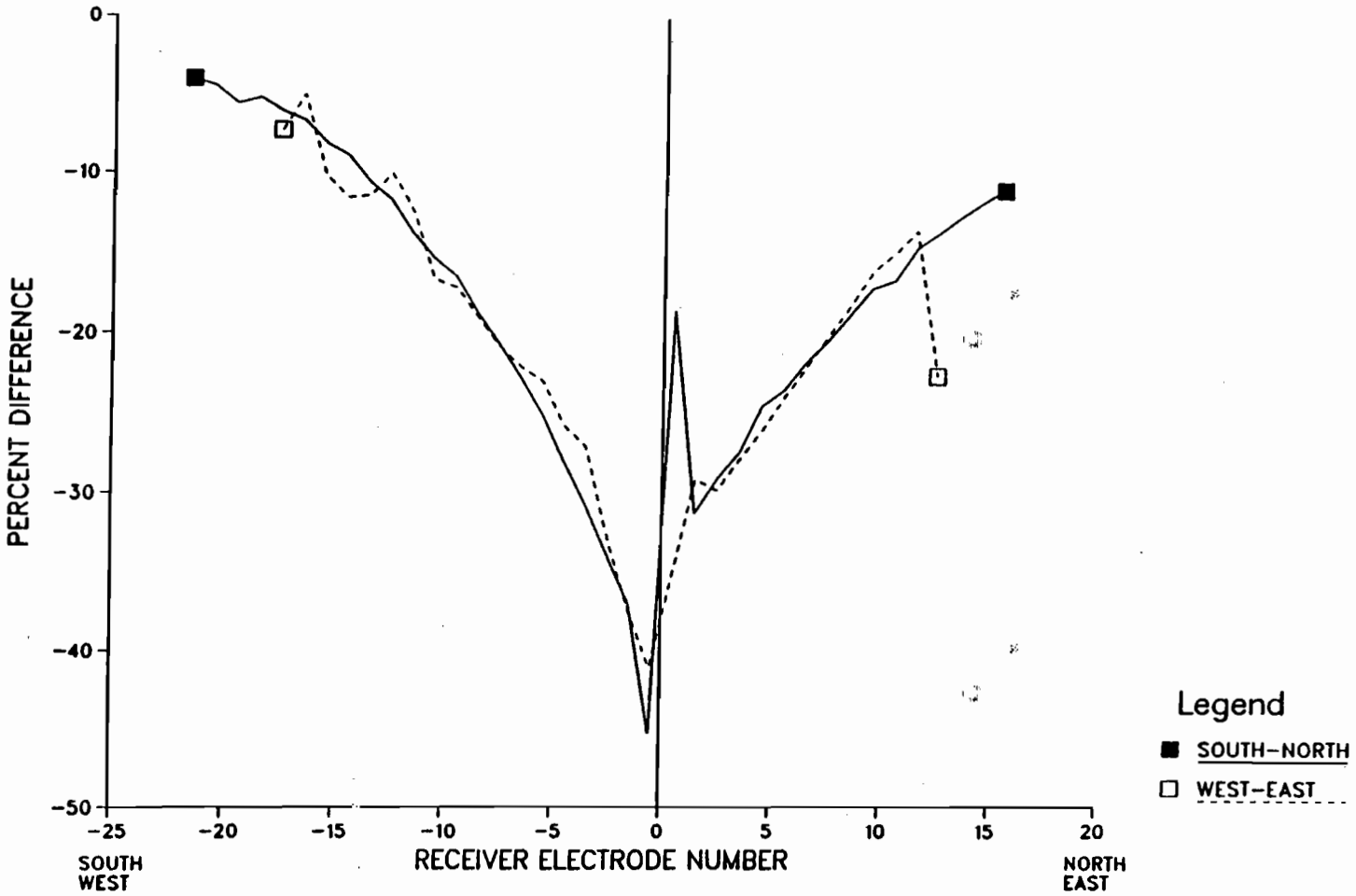

Figure 3.14. Baseline apparent resistivity data from the 30 m current electrode percent differenced against the data from the 40 m current electrode.

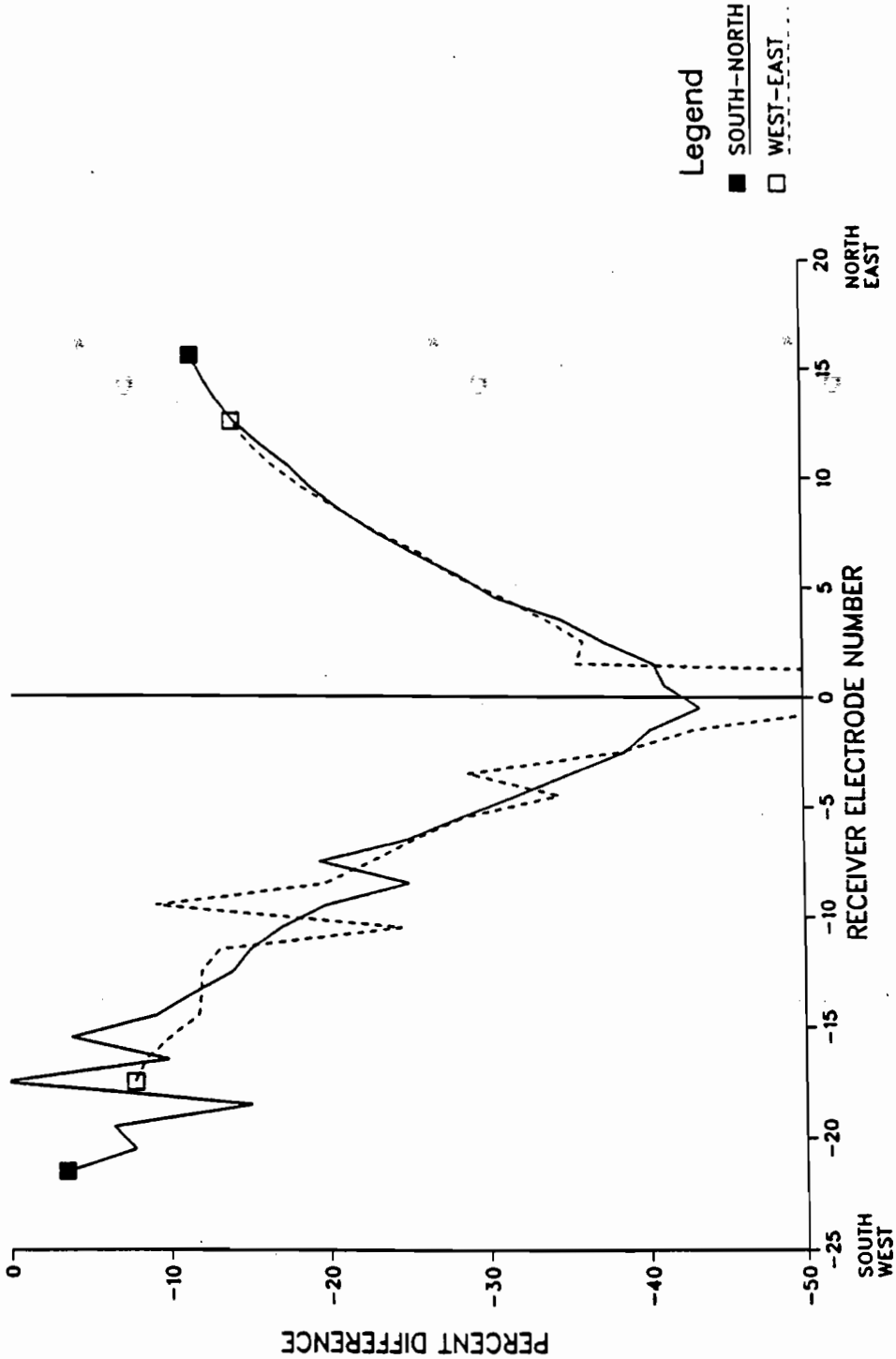

Figure 3.15. Maximum injection apparent resistivity data from the 30 m current electrode percent differenced against the data from the 40 m current electrode.

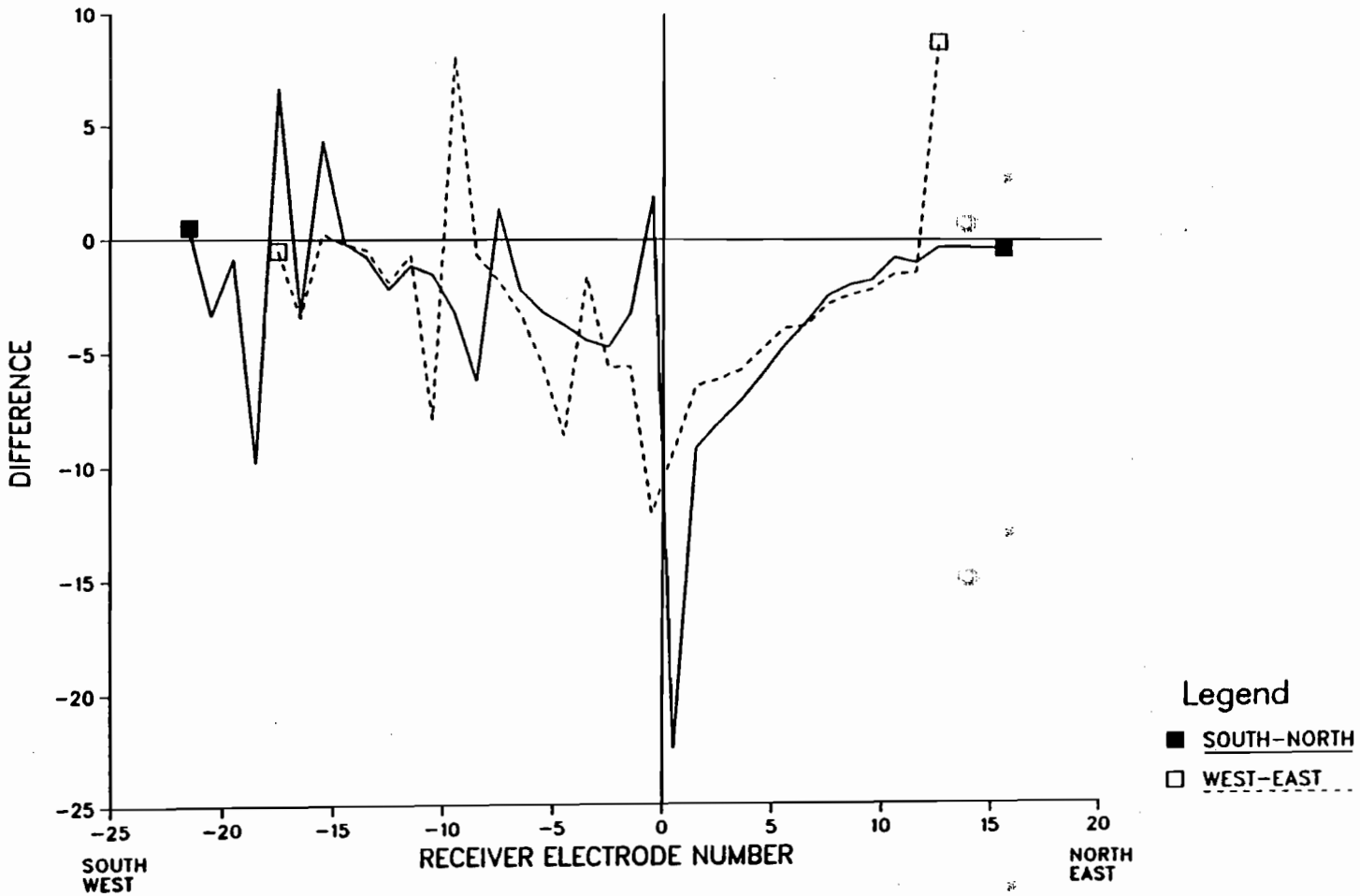

Figure 3.16. Temporal difference of the superposed pole-dipole data. This is the result of subtracting the data in Figure 3.14 from the data in Figure 3.15.

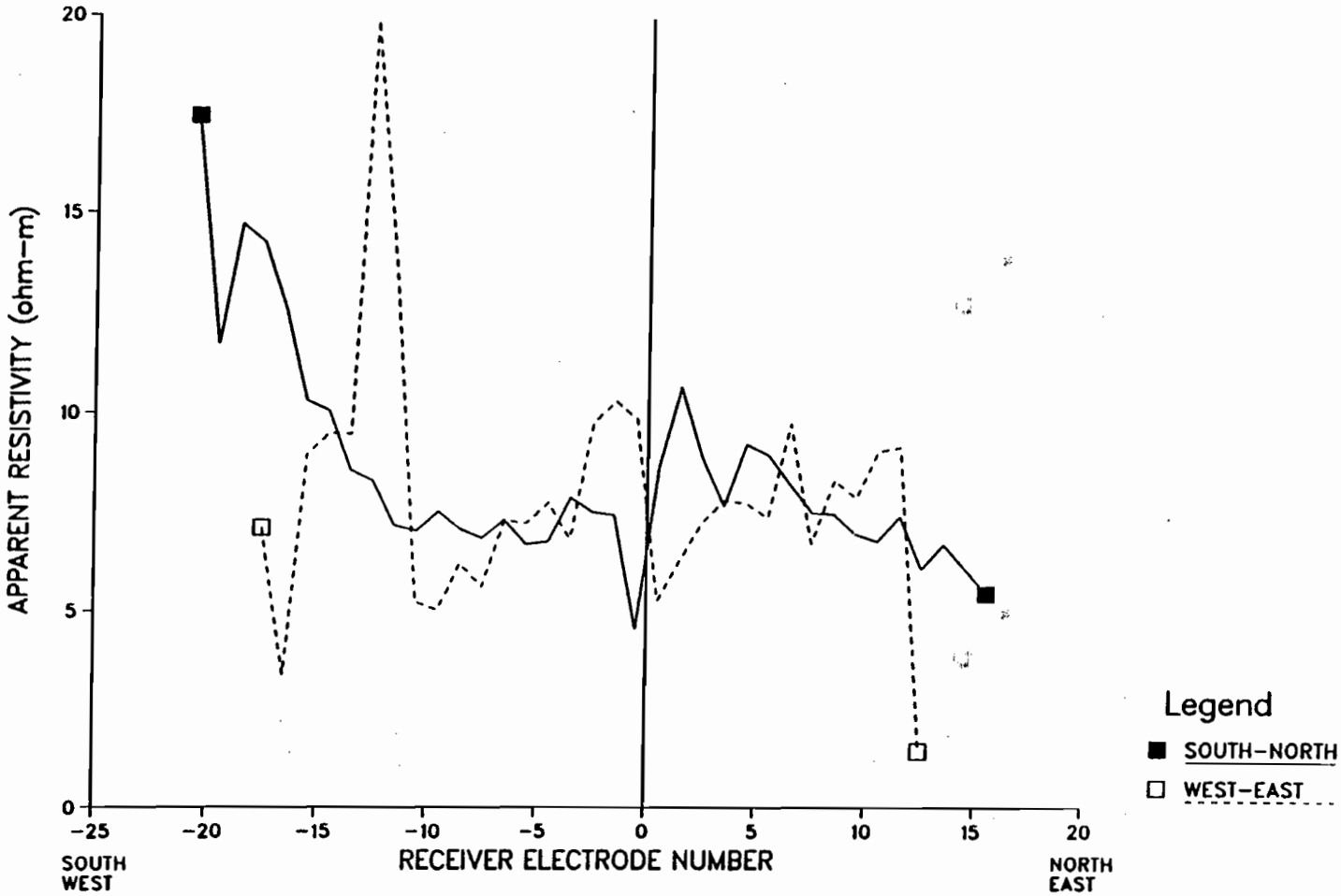

Figure 3.17. Baseline apparent resistivity calculated from the superposed dipole-dipole potential. The pole-pole data was superposed to create dipole-dipole voltages for apparent resistivity calculation.

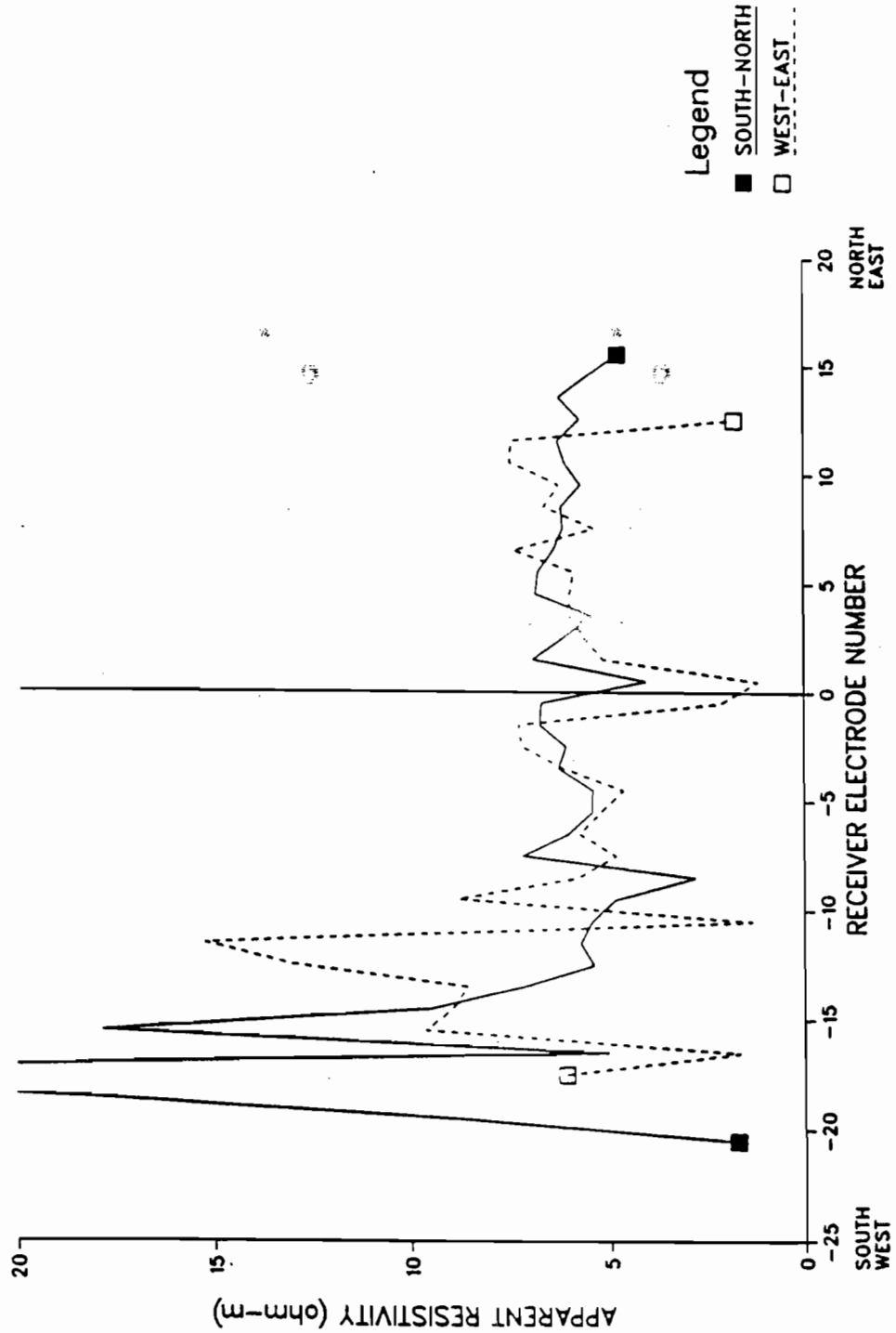

Figure 3.18. Apparent resistivity at maximum injection calculated from the superposed dipole-dipole data.

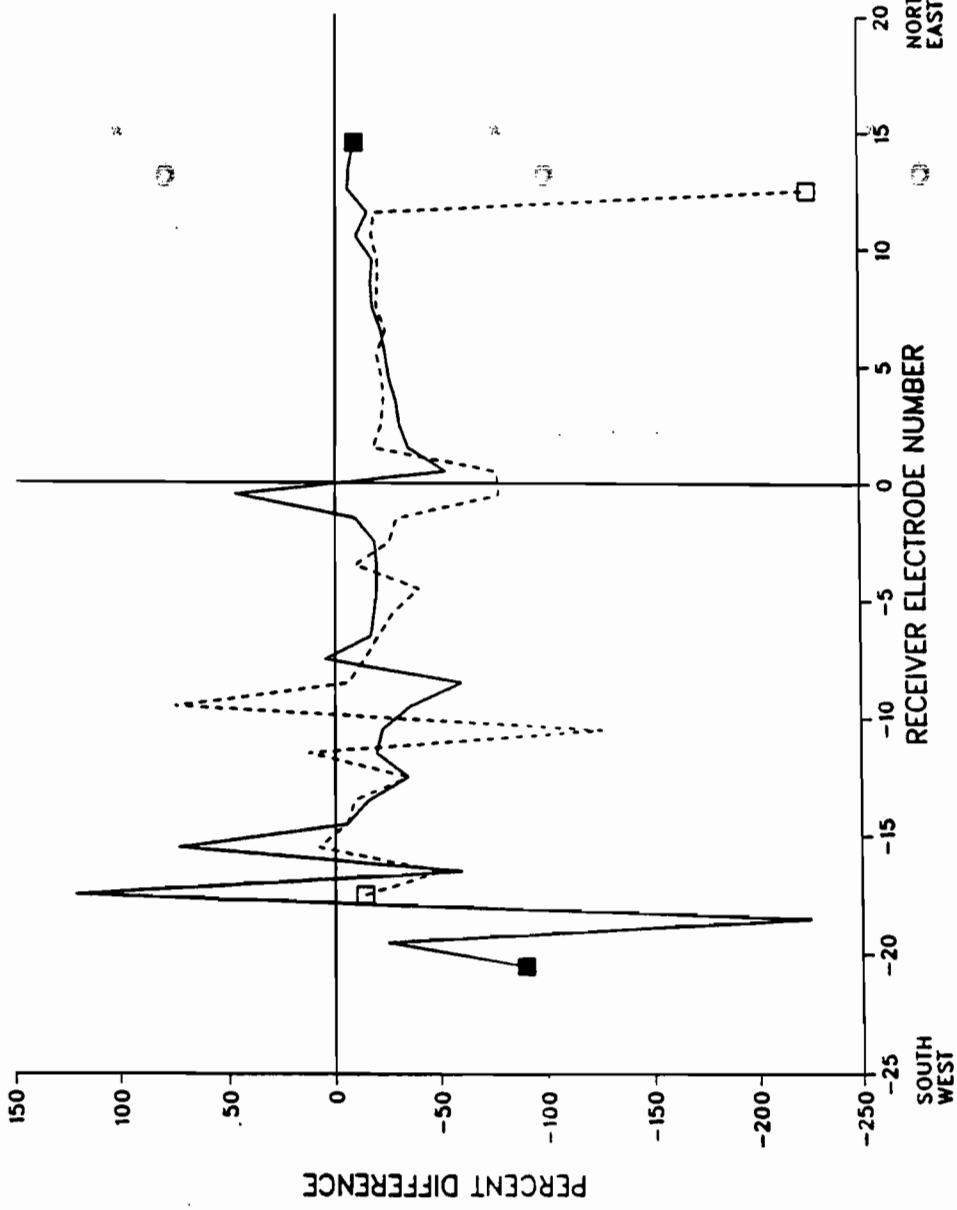

Figure 3.19. Temporal percent difference of the superposed dipole-dipole data. This is the result of taking the percent difference of the data in Figure 3.18 relative to the data of Figure 3.17.

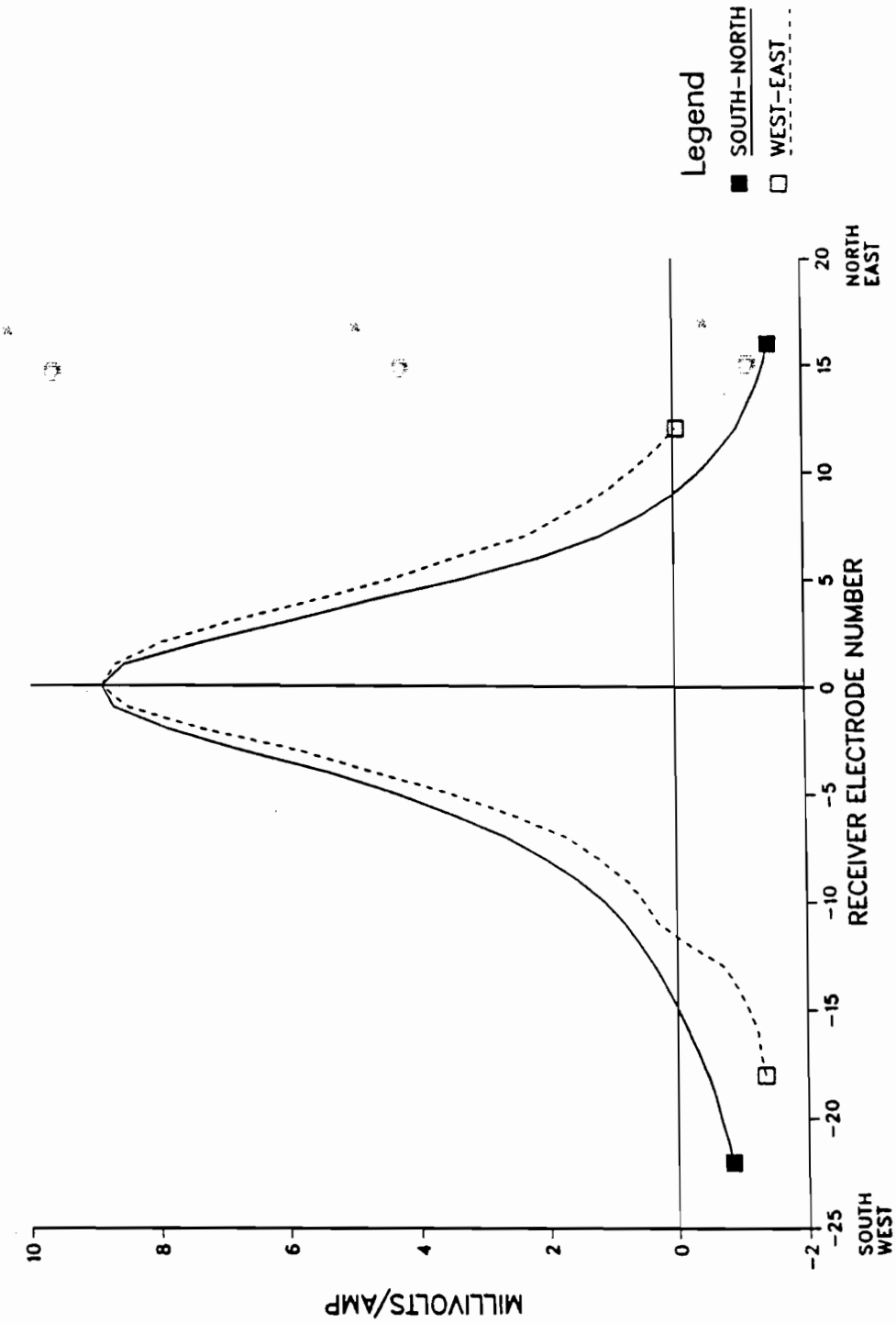

Figure 3.20. Baseline potential for the superposed dipole-pole configuration.

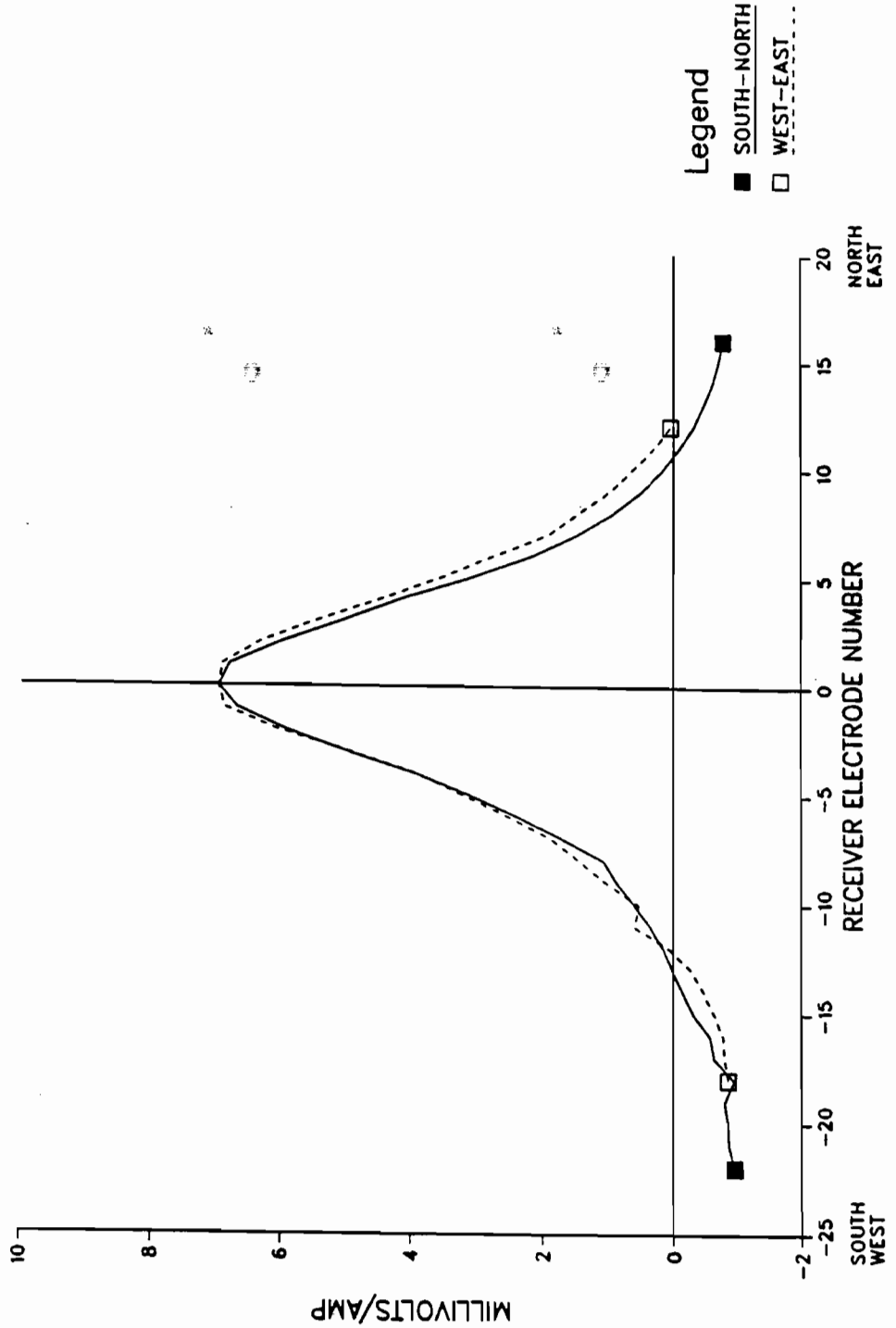

Figure 3.21. Potential at maximum injection for the superposed dipole-pole configuration.

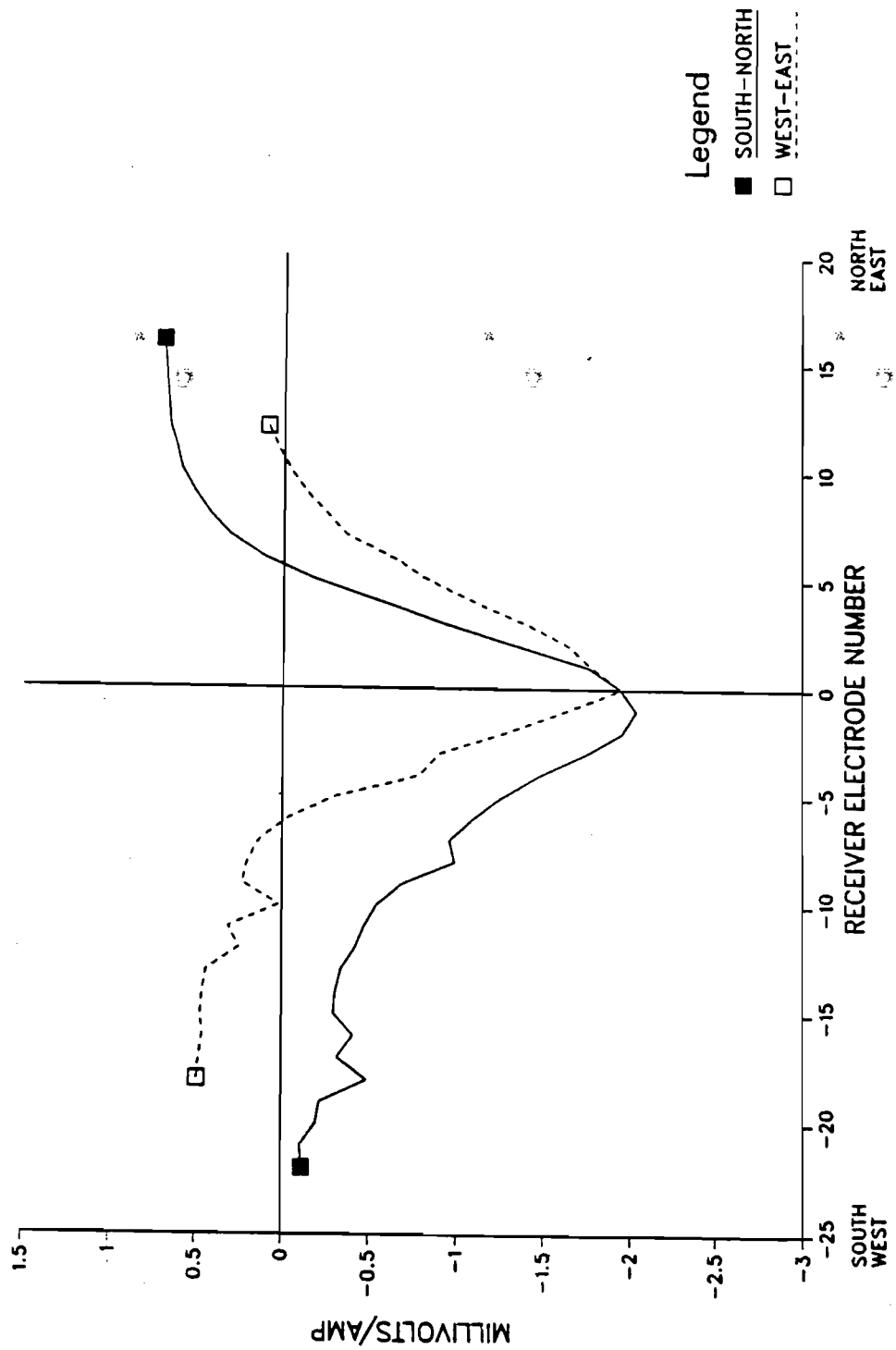

Figure 3.22. Potential difference relative to baseline for the superposed dipole-pole configuration.

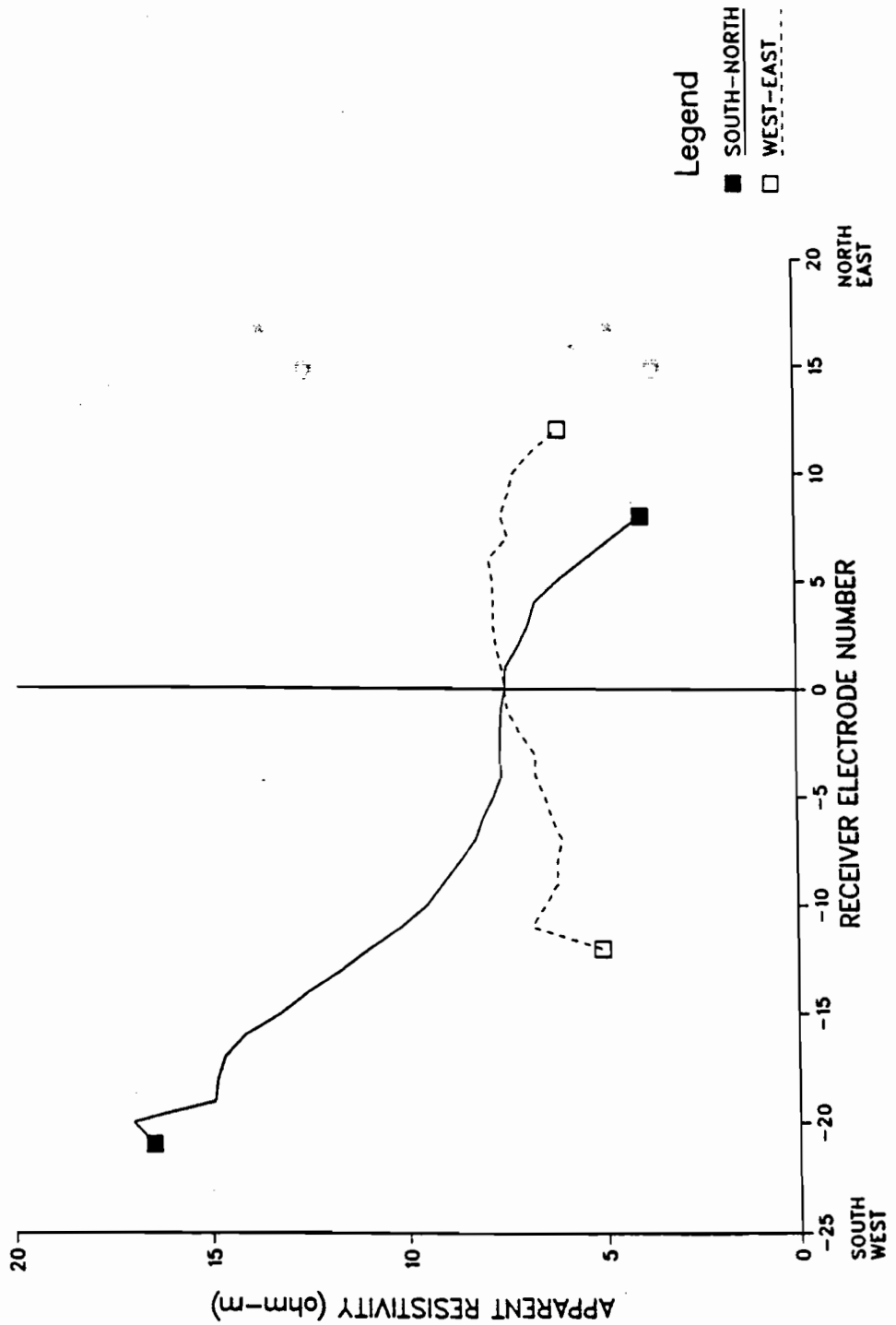

Figure 3.23. Baseline apparent resistivity calculated from the superposed dipole-pole potential.

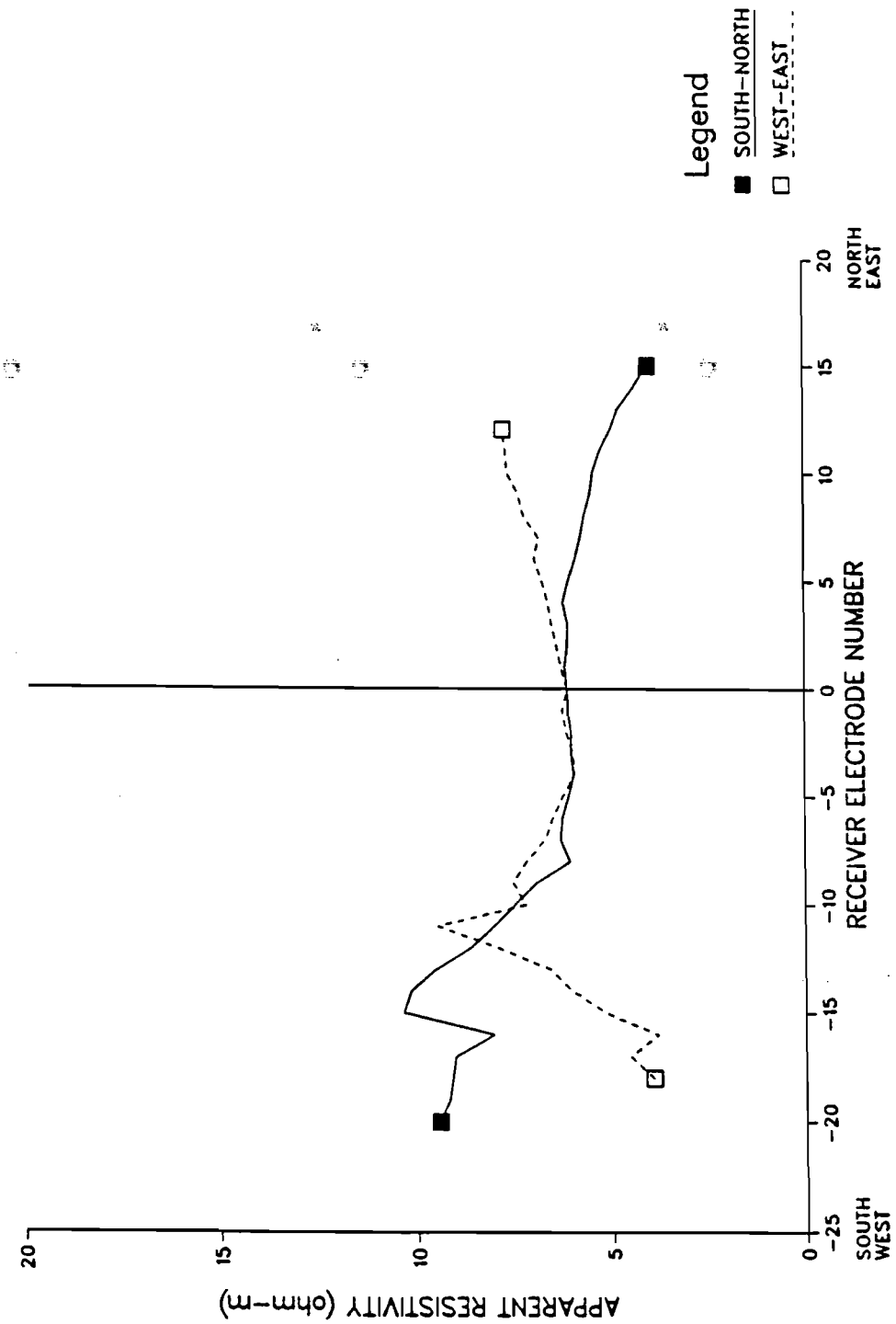

Figure 3.24. Apparent resistivity at maximum injection calculated from the superposed dipole-pole potential.

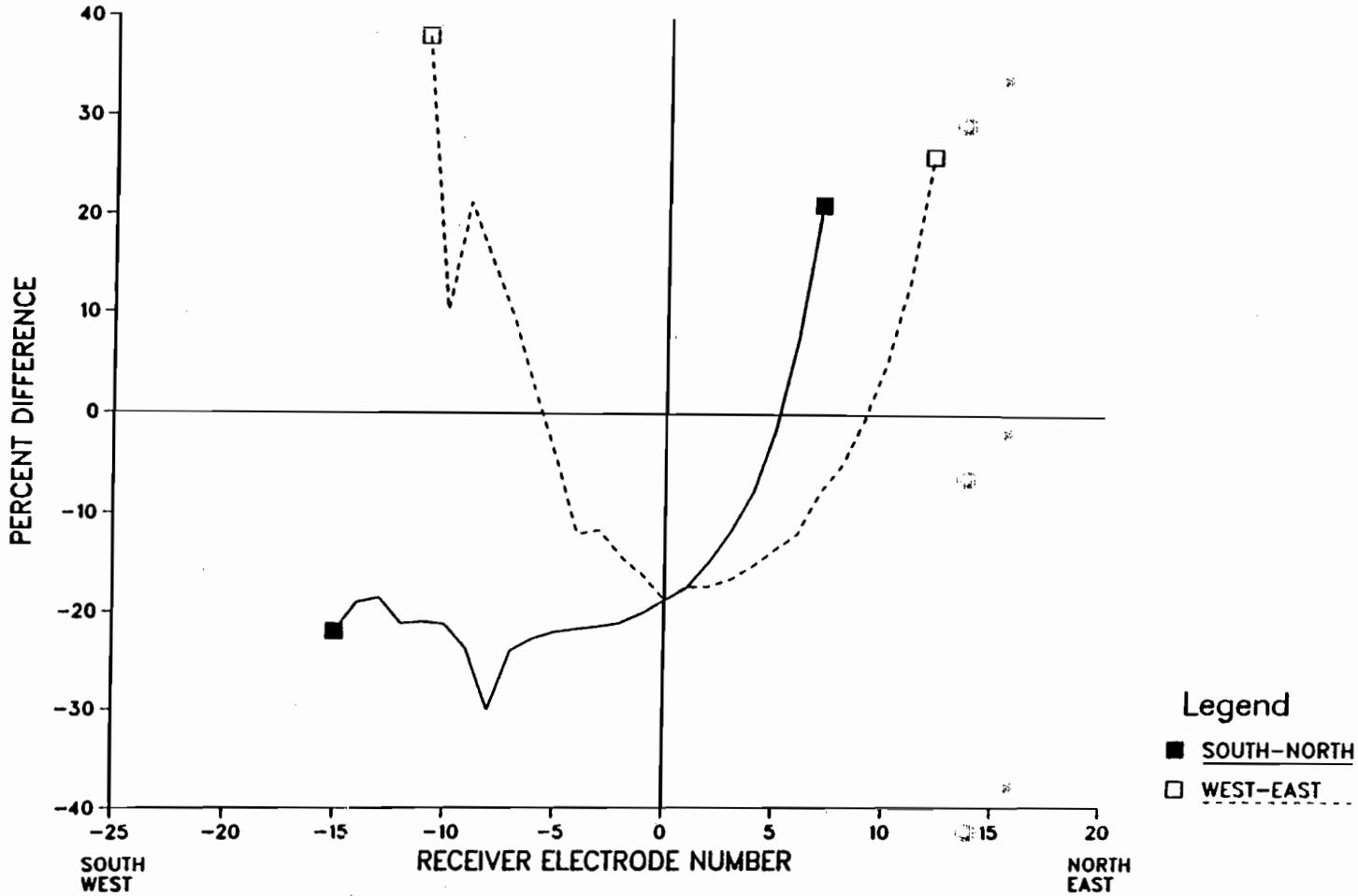

Figure 3.25. Temporal percent difference of the superposed dipole-pole data. This is the result of taking the percent difference of the data in Figure 3.24 relative to the data of Figure 3.23.

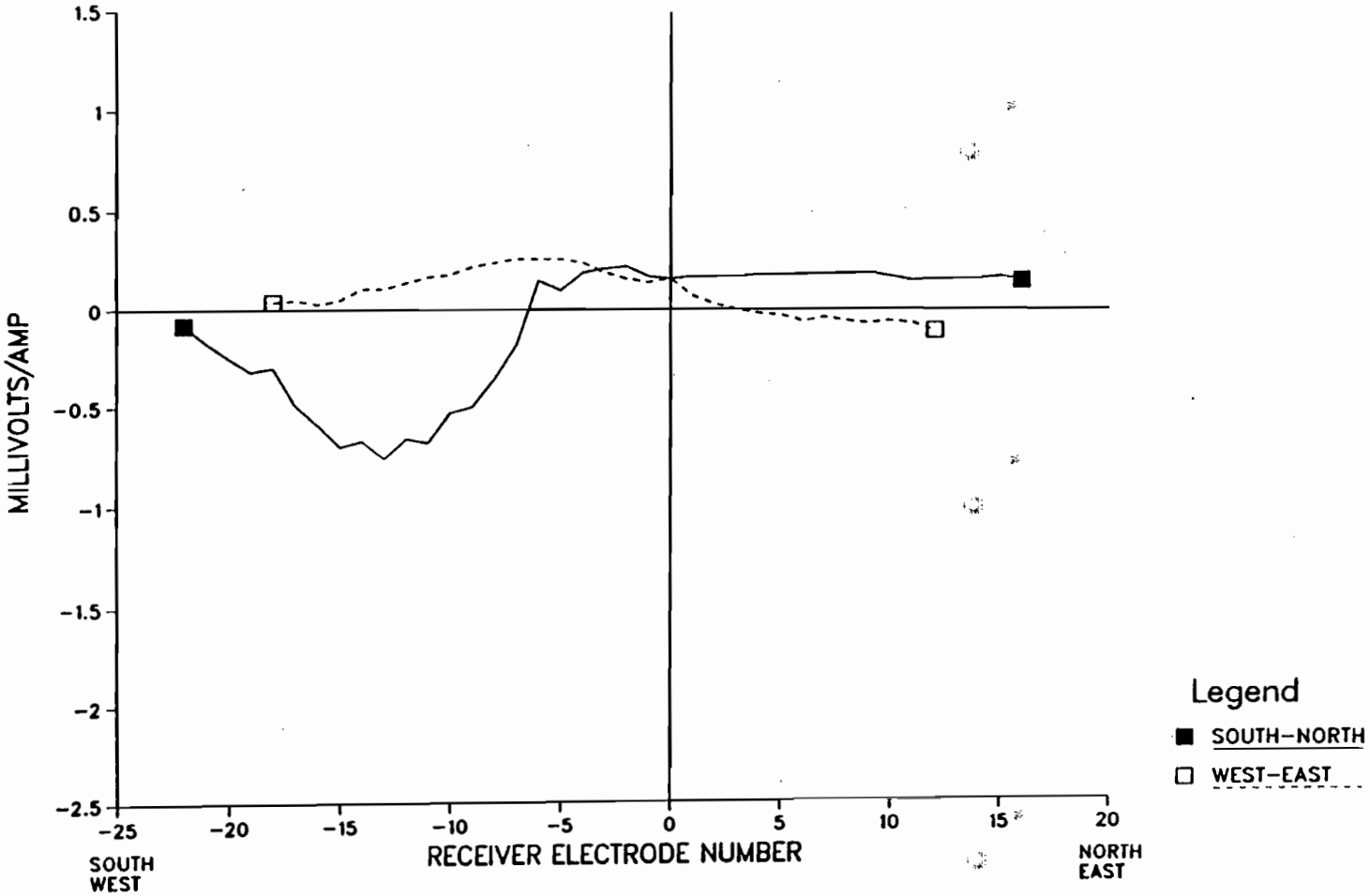

Figure 3.26. Dipole-pole potential difference relative to baseline for a dipole with current electrodes at the surface and at 30 m depth in well EXT.

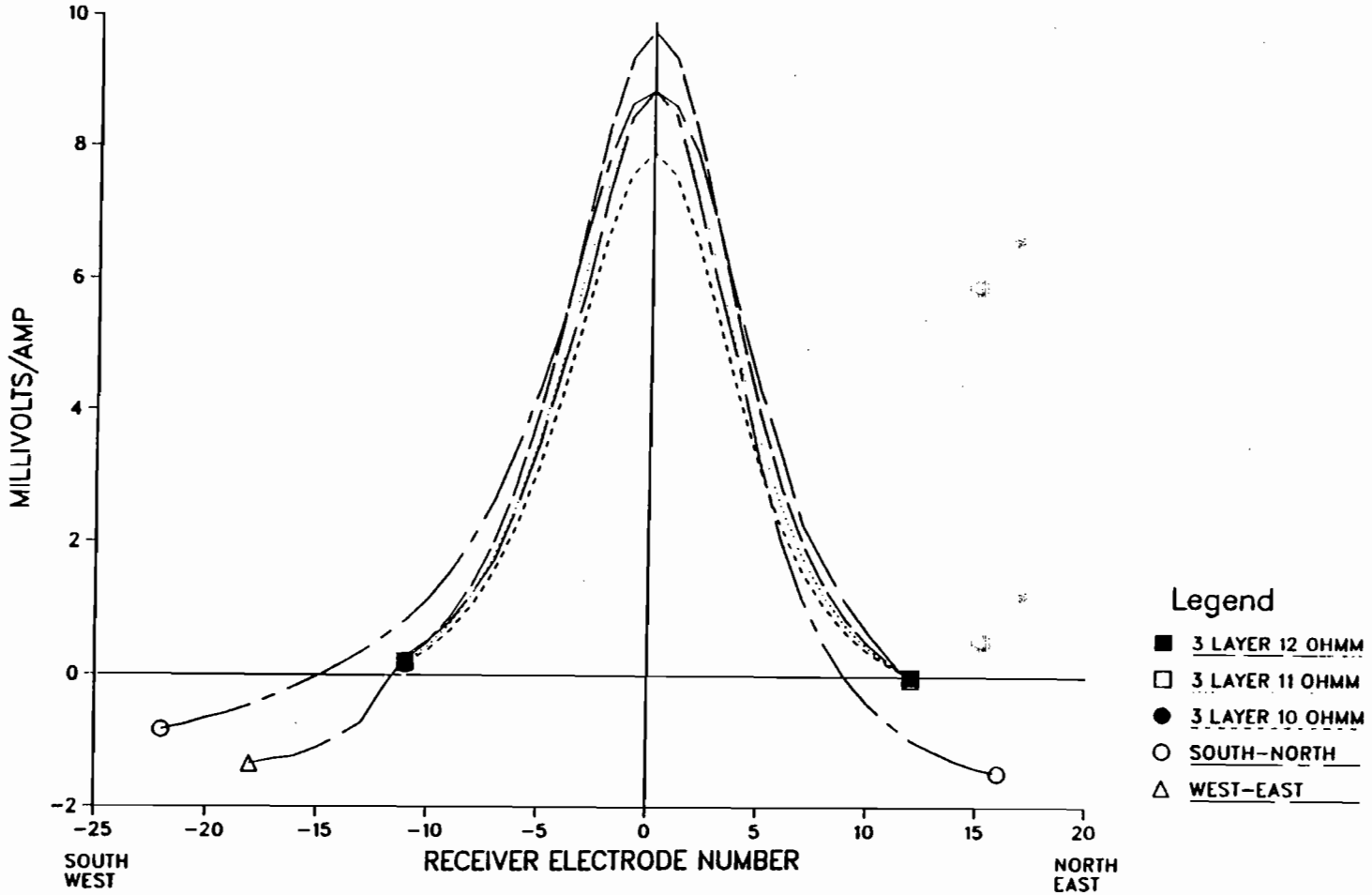

Figure 3.27. Baseline dipole-pole data compared to three layer analytical model results. The middle layer resistivity was varied from 10 to 12 ohm-m.

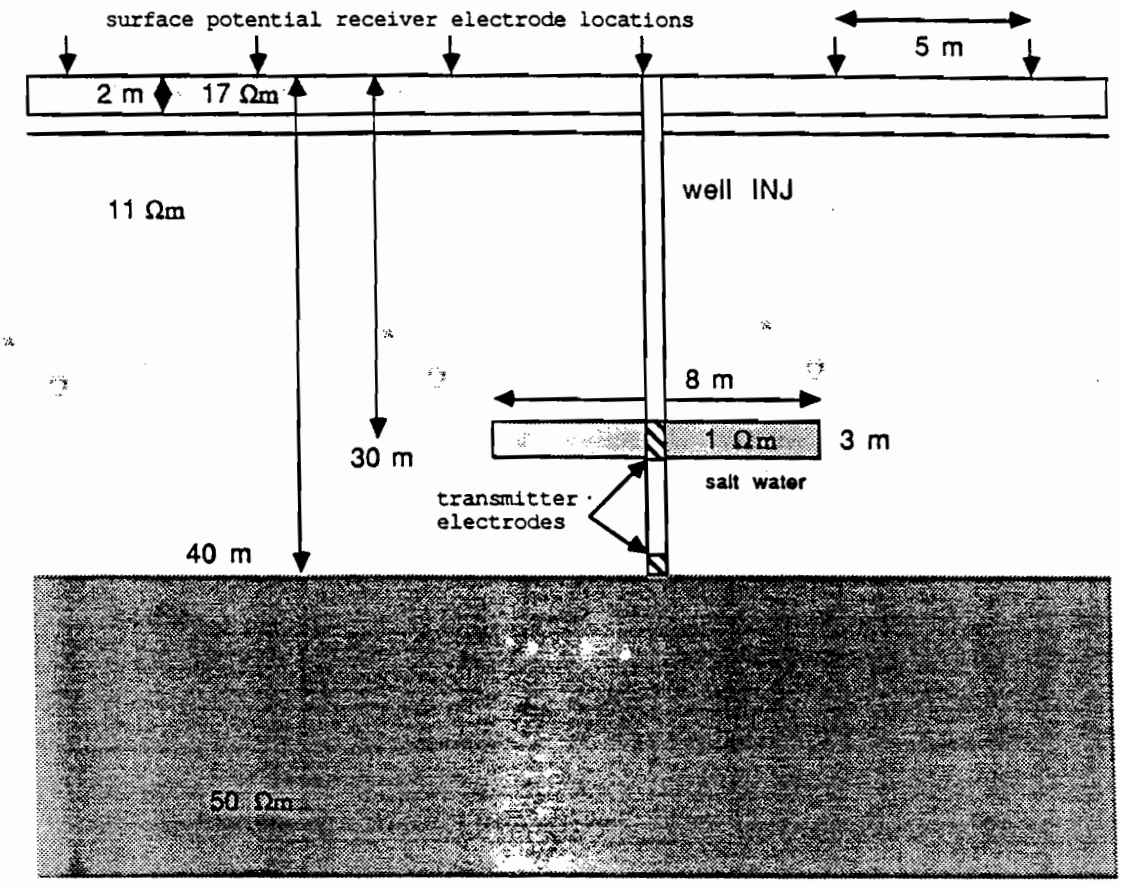

Figure 3.28. Cross-section of the three-dimensional model used to simulate the salt water injection experiment.

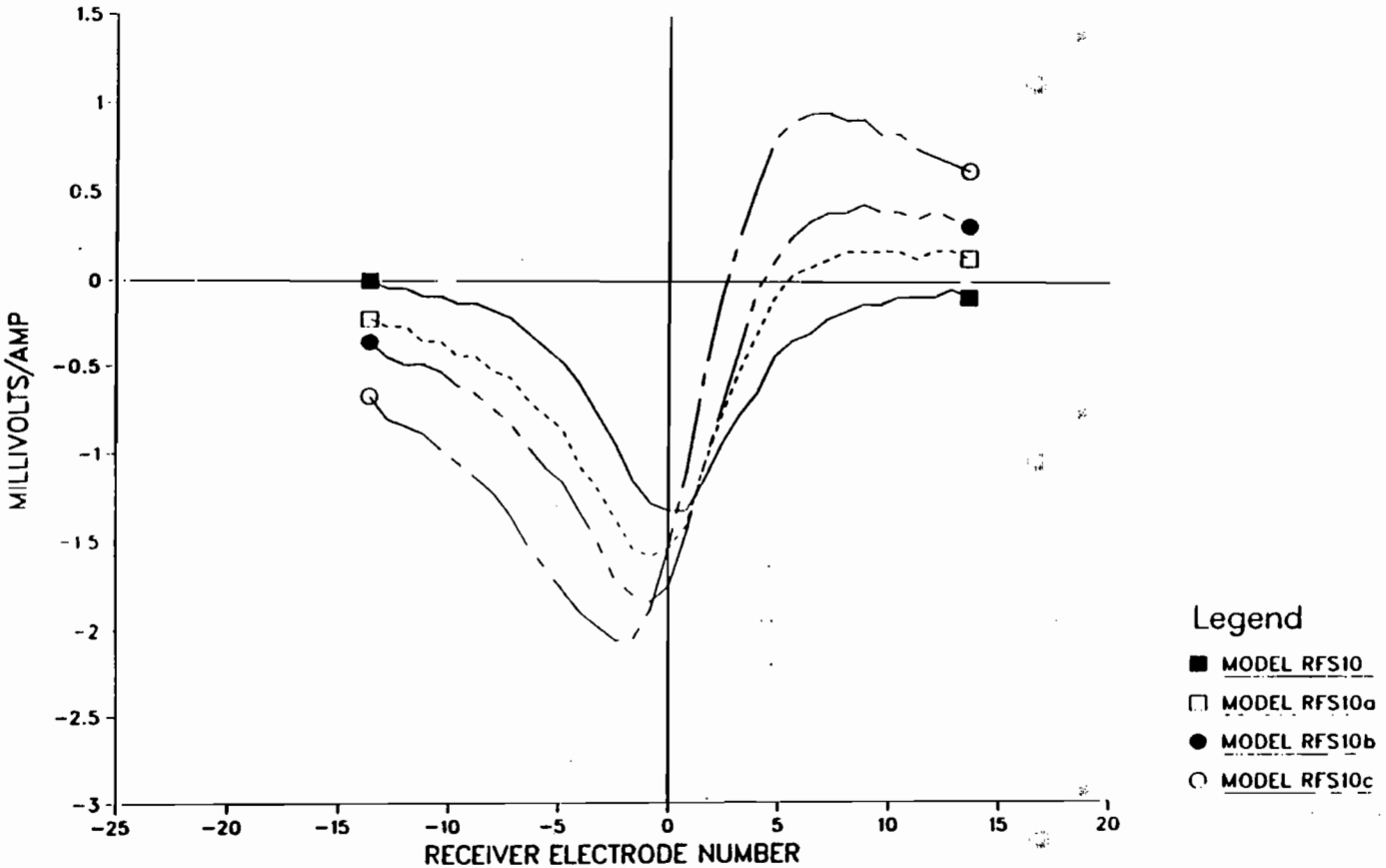

Figure 3.29. Three-dimensional model results for the borehole to surface dipole-pole configuration. These curves of potential difference are for 2 m thick salt water block models corresponding to 30 percent formation porosity.

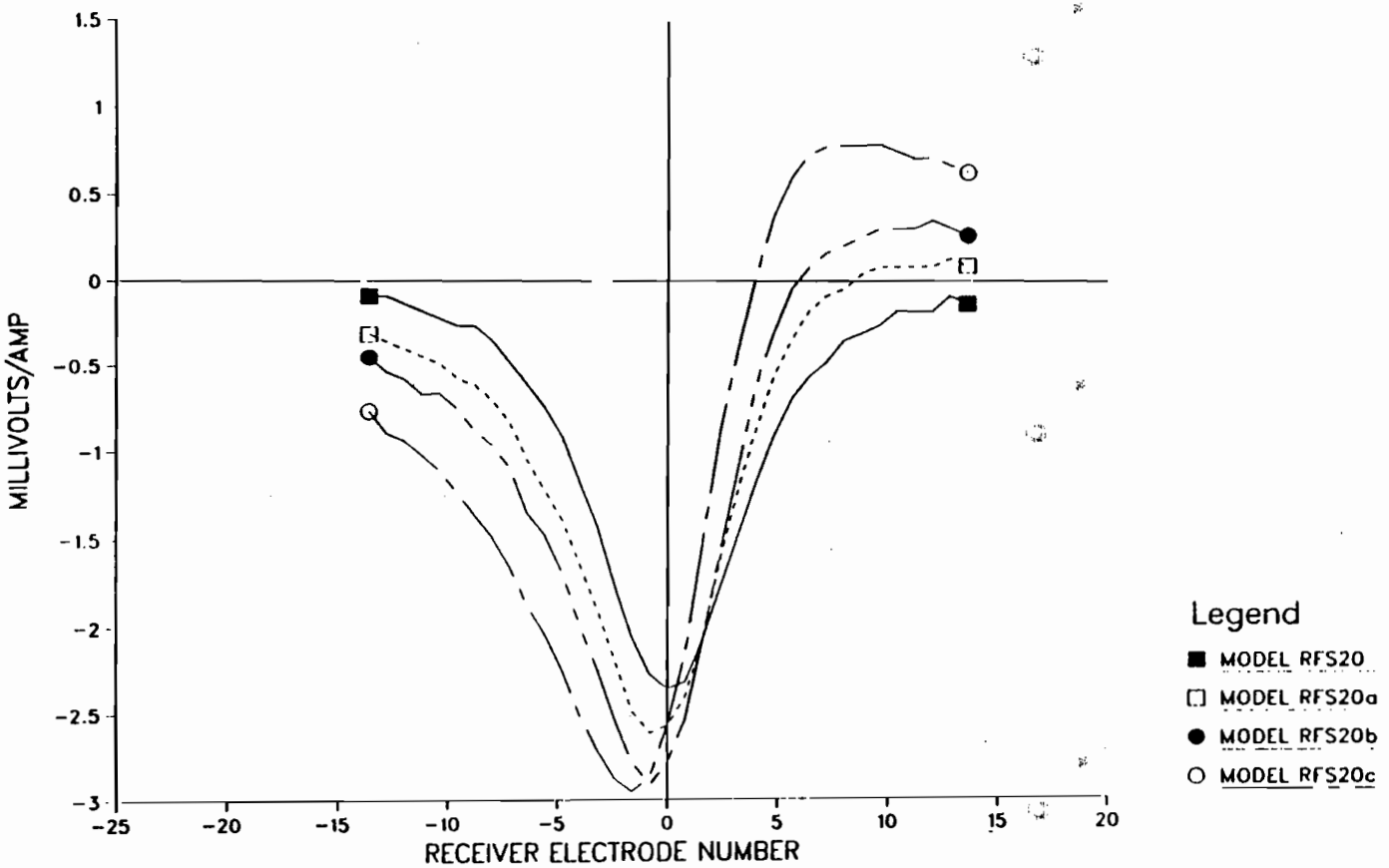

Figure 3.30. Three-dimensional model results for the borehole to surface dipole-pole configuration. These curves of potential difference are for 3 m thick salt water block models corresponding to 20 percent formation porosity.

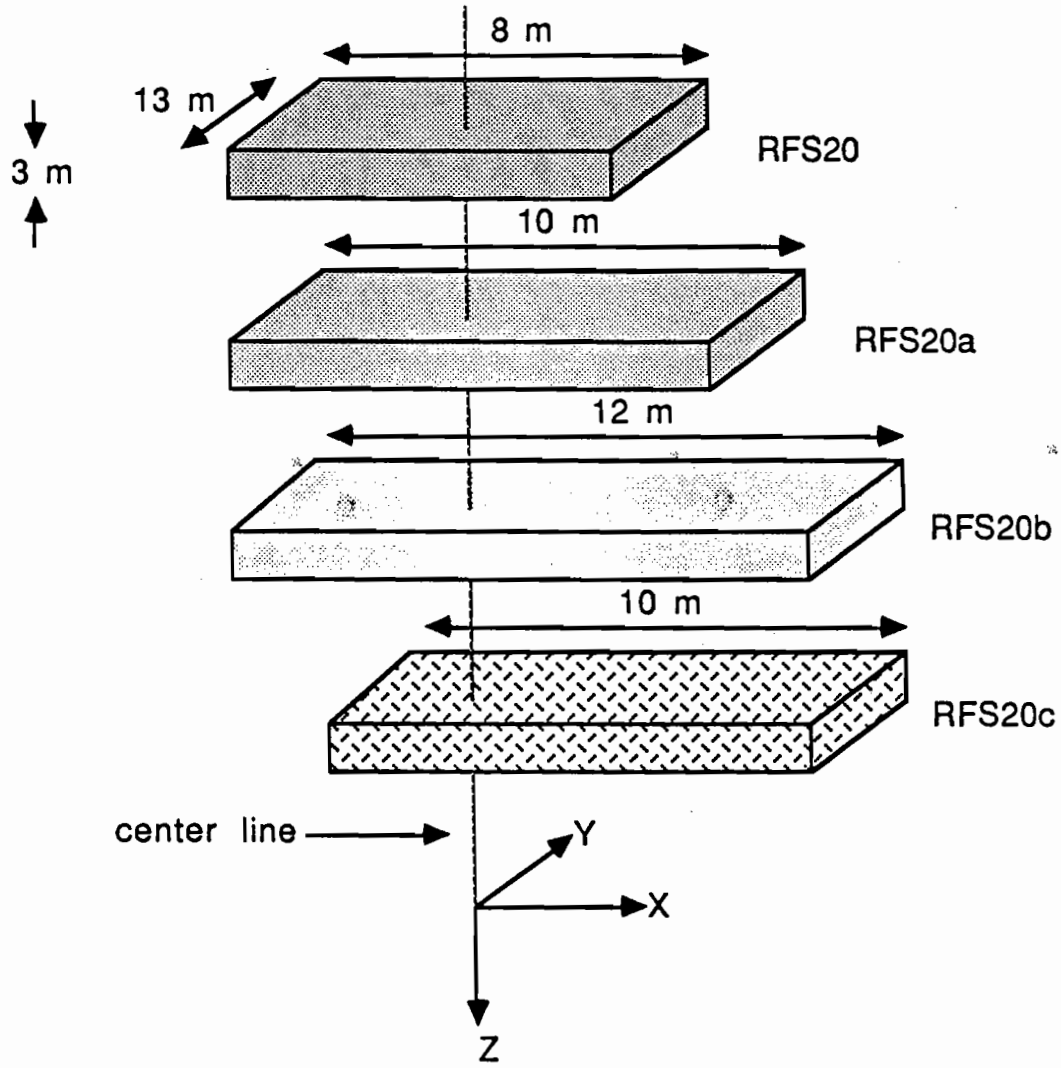

Figure 3.31. Relative positions and dimensions of the RFS20 salt water models. All models are 3 m in the z direction, 13 m in the y direction, and from 8 to 12 m in the x direction. The point where the center line intersects the blocks represents the location of the 30 m INJ electrode. The blocks are symetric about the center line in the y direction.

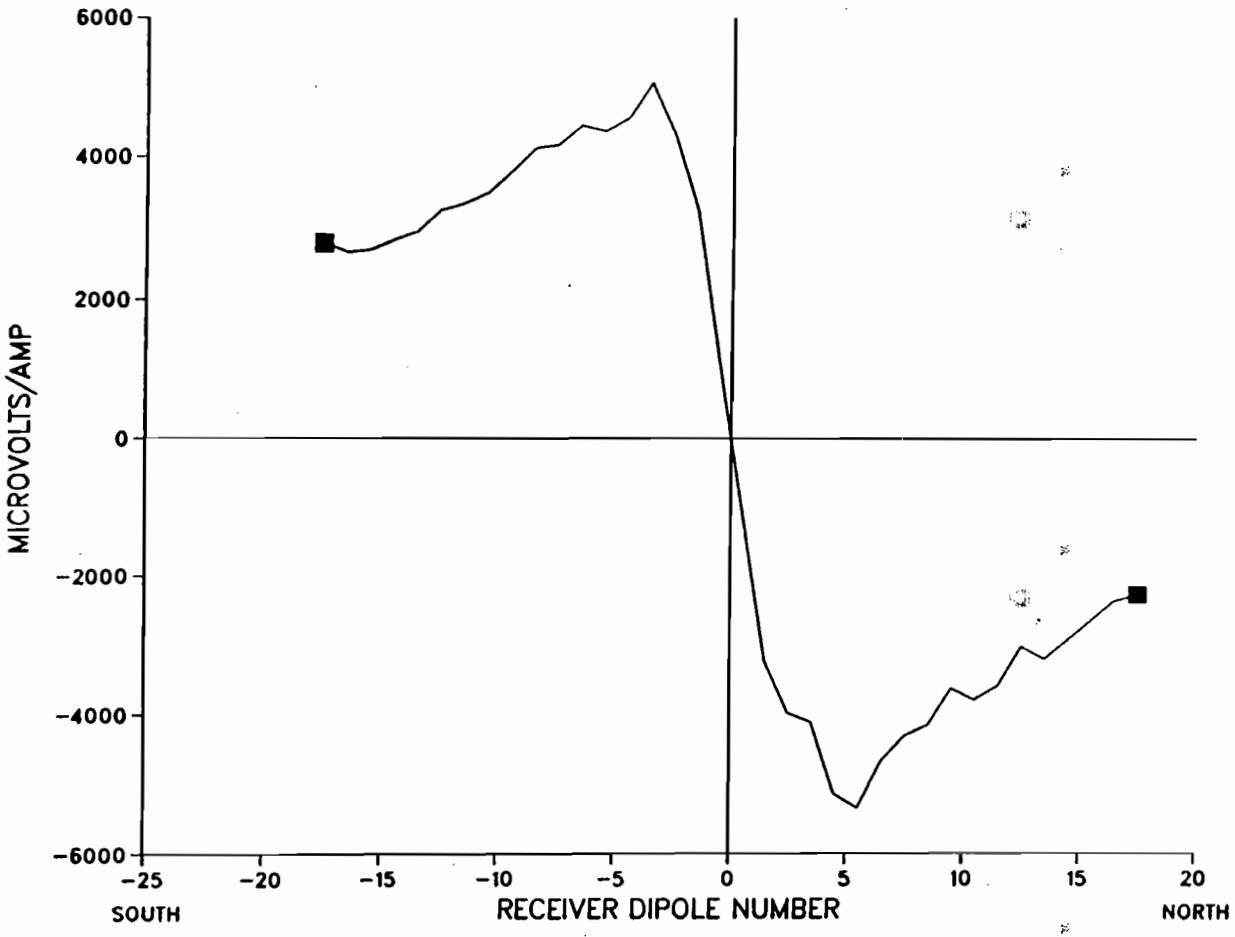

Figure 3.32. Pole-dipole normalized voltage at maximum salt water injection for a current electrode at 30 m depth in well INJ.

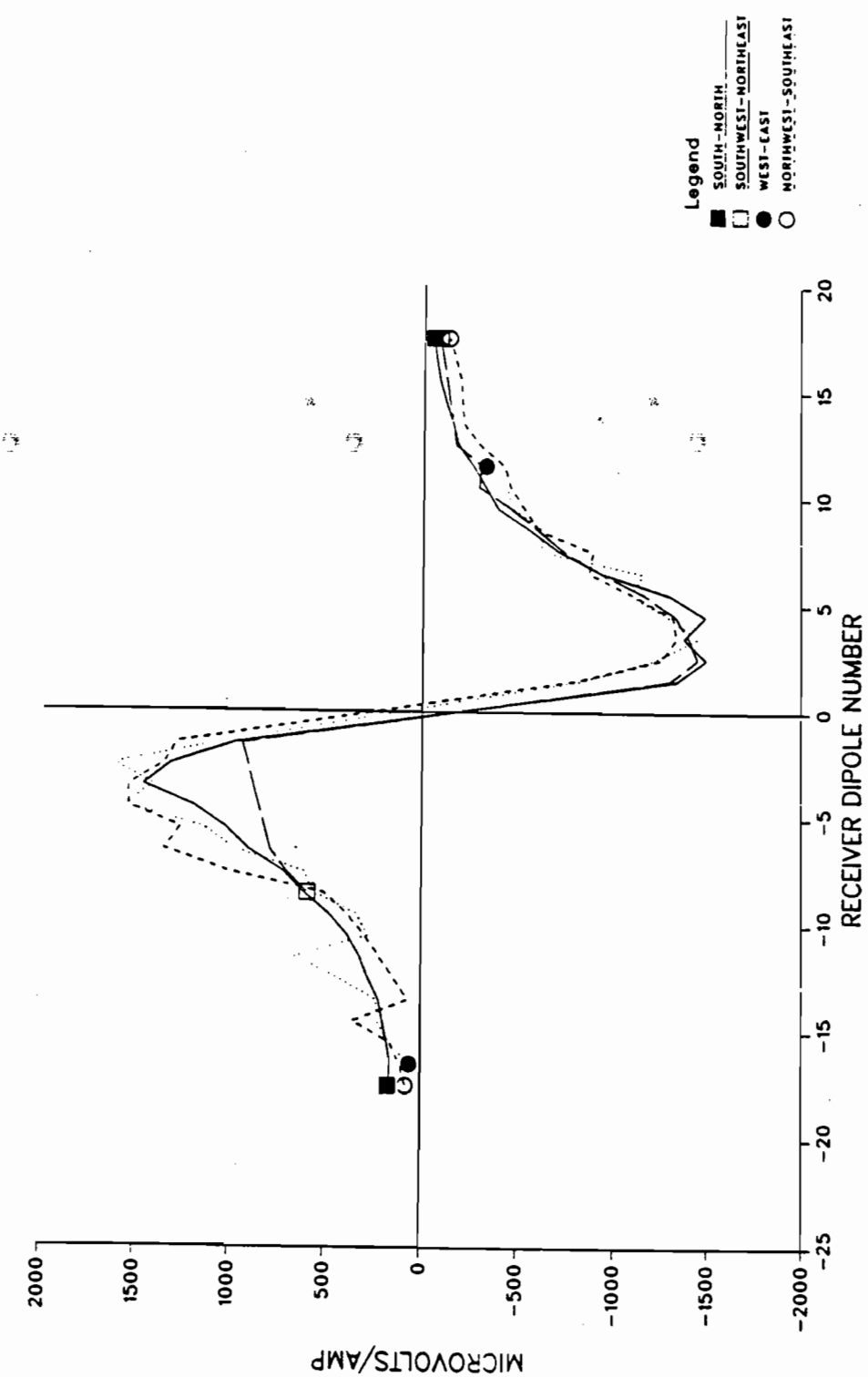

Figure 3.33. Baseline dipole-dipole normalized voltage obtained by superposition of the 30 m and 40 m depth pole-dipole data.

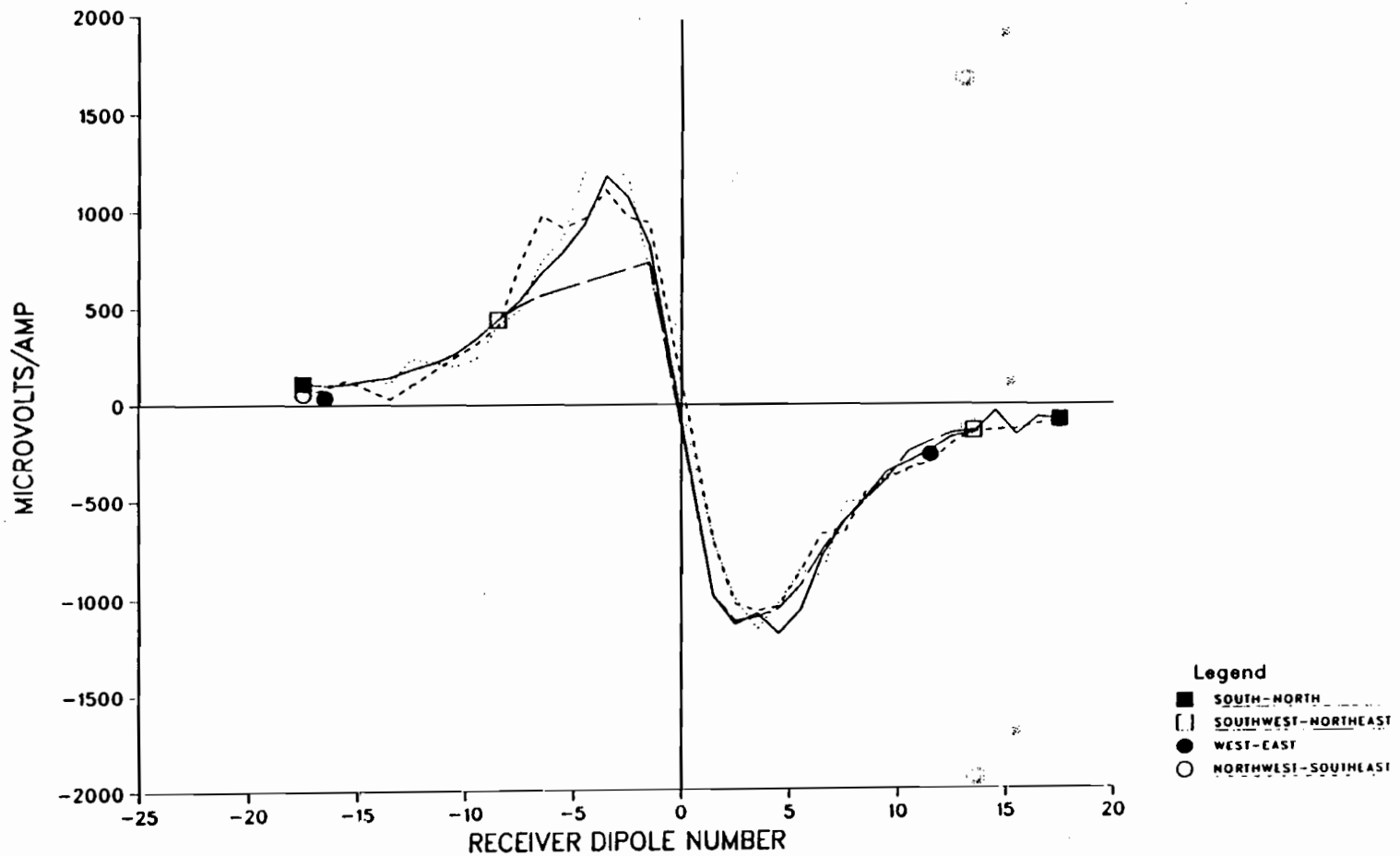

Figure 3.34. Maximum injection dipole-dipole normalized voltage obtained by superposition of the 30 m and 40 m depth pole-dipole data.

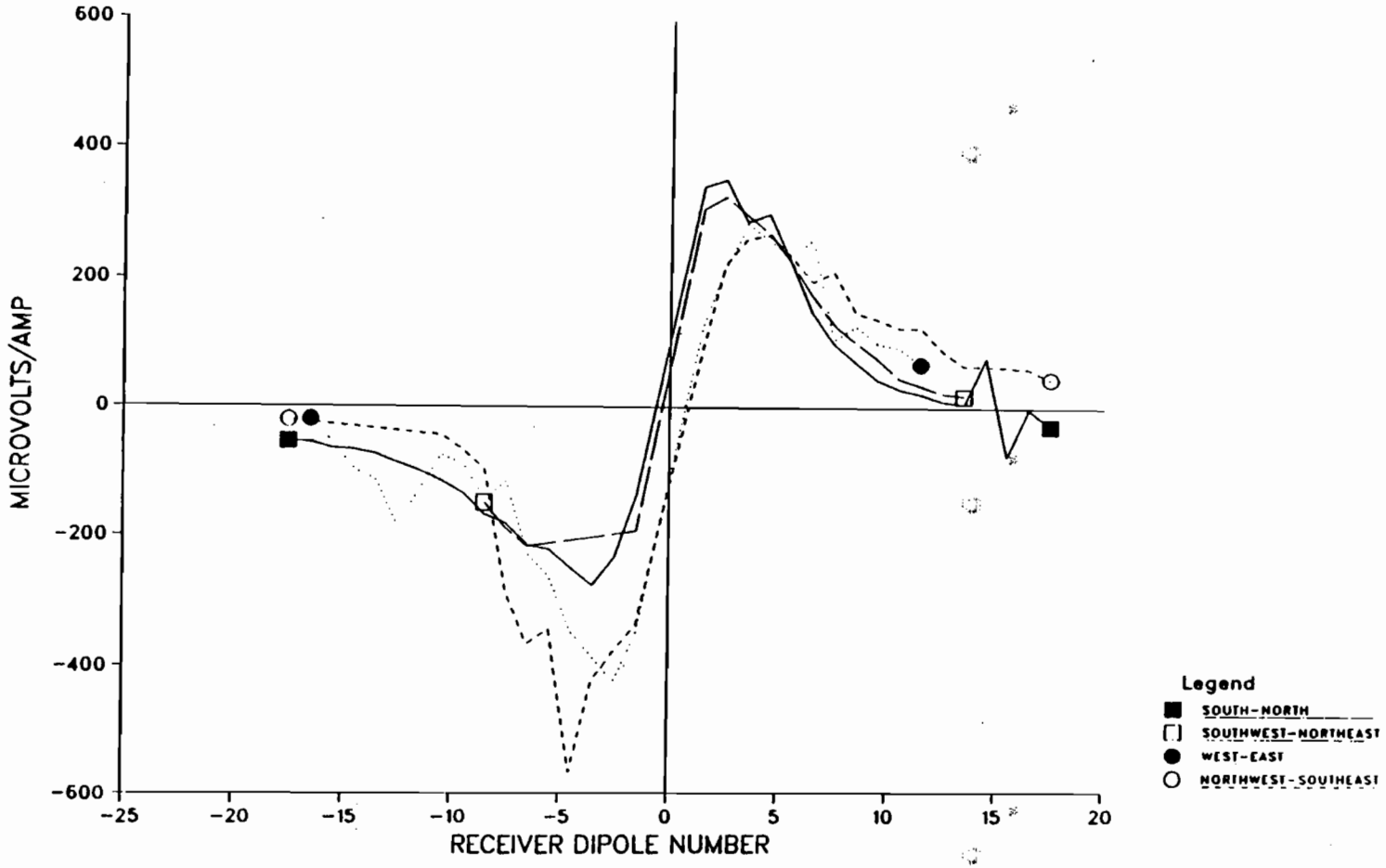

Figure 3.35. Curves of difference relative to baseline for dipole-dipole data along the four receiver lines. These curves were generated by subtracting the the data of Figure 3.33 from the data of Figure 3.34.

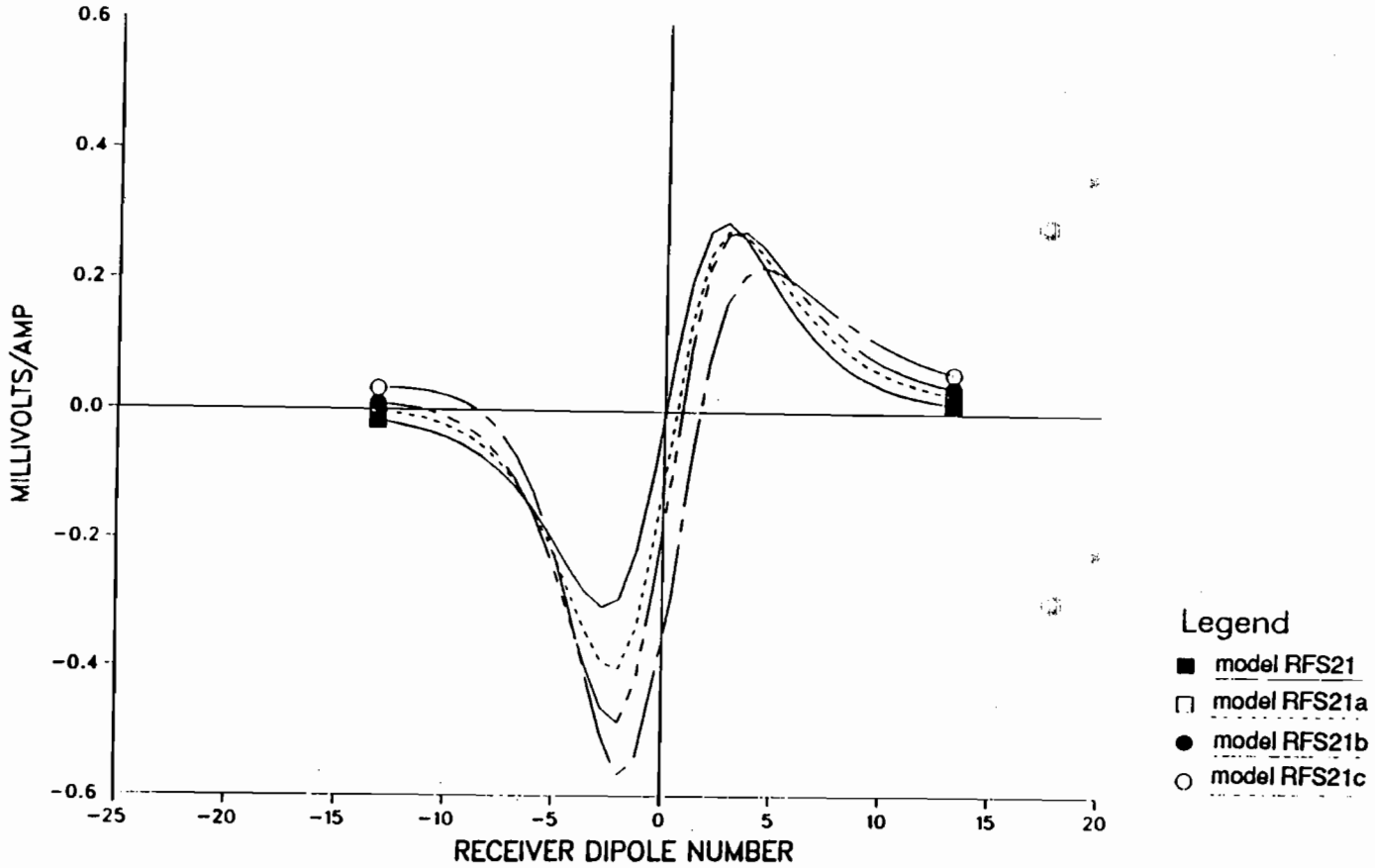

Figure 3.36. Three-dimensional model results for the borehole to surface dipole-dipole configuration. These curves of potential difference are for 3 m thick salt water block models corresponding to 20 percent formation porosity.

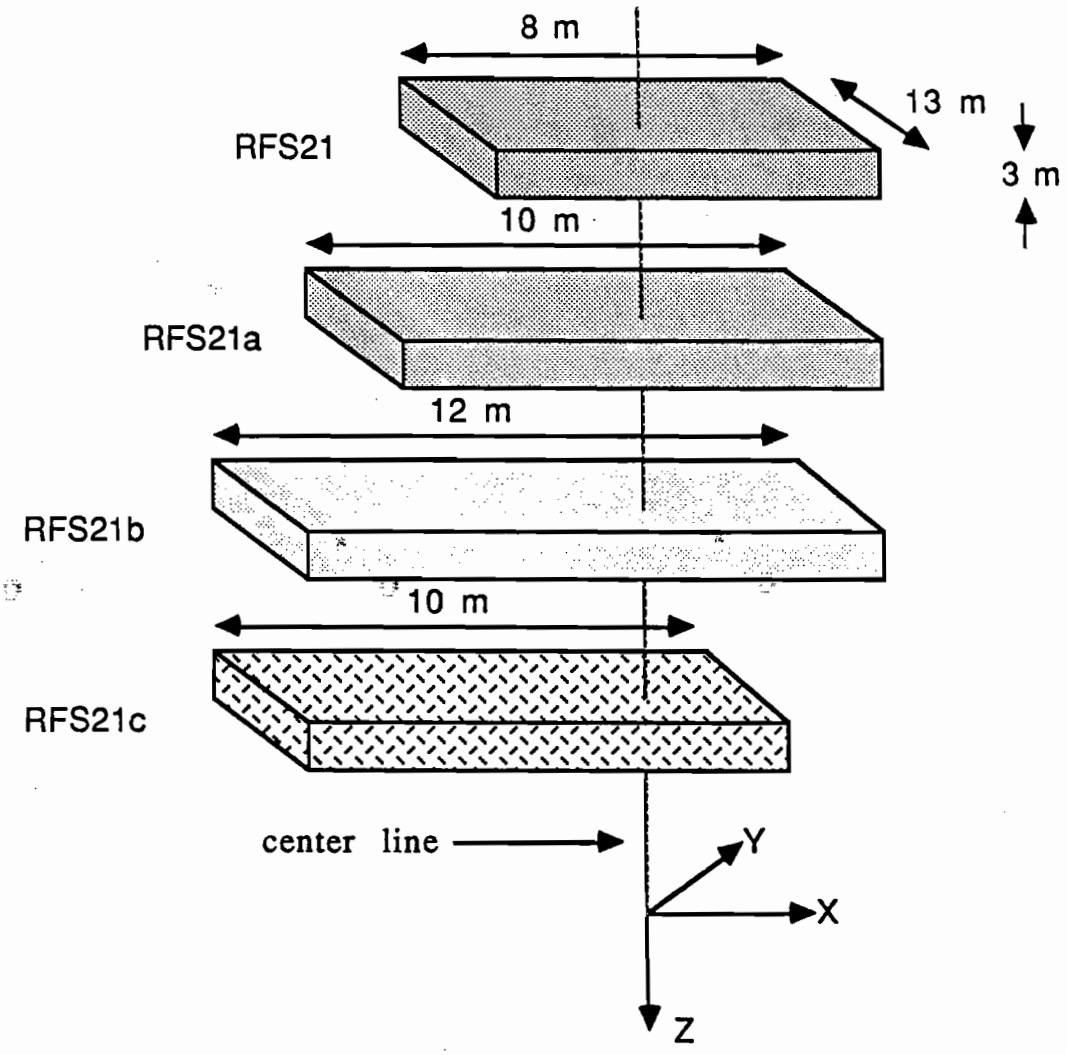

Figure 3.37. Relative positions and dimensions of the RFS21 salt water models. All models are 3 m in the z direction, 13 m in the y direction, and from 8 to 12 m in the x direction. The point were the center line intersects the blocks represents the location of the 30 m INJ electrode. The blocks are symetric about the center line in the y direction. Note that these models are offset to the left.